NUMERICAL MODELING OF CAPILLARY DRIVEN MICROFLUIDIC FLOW

by

MD ASHRAFUL ISLAM

Presented to the Faculty of the Graduate School of

The University of Texas at Arlington in Partial Fulfillment

of the Requirements

for the Degree of

DOCTOR OF PHILOSOPHY

THE UNIVERSITY OF TEXAS AT ARLINGTON

DECEMBER 2016

Acknowledgements

I am grateful to my PhD supervisor Dr. Albert Y. Tong for his sincere guidance towards the completion of my PhD. Dr. Tong introduced me to this exciting area of research, taught me the scientific approach of analyzing problems, helped me to develop effective research plan and gave suggestions to overcome the difficulties. Besides the regular weekly meetings, he made himself available whenever I needed help, even during the weekend and vacations. I am especially thankful for his enormous effort and time to correct and improve my technical writings. I am indebted to him not only for the research guidance but also for the engineering philosophy he taught me.

I would also like to thank my committee members, Dr. Ankur Jain, Dr. Hyejin Moon, Dr. Chaoqun Liu and Dr. Ratan Kumar for their thoughtful comments and suggestions on this work. I would also like to thank my group members Dr. Vimal Ramanuj and Dr. Yin Guan for their assistance in my research.

I am also grateful to the state of the art high performance computing facilities at UTA and Texas Advanced Computing Center (TACC) where I have run most of my simulations. I am also thankful for the teaching assistantship provided by the Department of Aerospace and Mechanical Engineering at UTA which was essential to support my education and research.

Finally, I would like to thank my family for their understanding and patience. I am especially thankful to my wife, Mun Mun Nahar, who has been tremendously supporting during this whole time. She not only gave me mental support but also helped me technically in my research.

November 29, 2016

Abstract

NUMERICAL MODELING OF CAPILLARY DRIVEN

MICROFLUIDIC FLOW

Md Ashraful Islam, PhD

The University of Texas at Arlington, 2016

Supervising Professor: Albert Y. Tong

Capillary driven two dimensional axisymmetric and three dimensional asymmetric flow in various microfluidic applications have been modeled and analyzed numerically. The transient Navier-Stokes equations are solved using a finite-difference formulation with a two-step projection method on a fixed grid. The vapor-liquid interface of the micro-droplet is tracked by volume-of-fluid (VOF) and coupled level set and volume-of-fluid (CLSVOF) methods with the surface tension force determined by the continuum surface force (CSF) model. The static contact angle at the three phase contact line has been modeled using wall adhesion scheme within the CSF framework. The developed numerical method for capturing the microfluidic flow with free surface has been validated using well-established benchmark tests.

Dynamics of drop formation from a vertical capillary tube and subsequent generation of satellite drops in air have been studied numerically. The evolution of complete droplet separation process has been simulated. The numerical results have been compared with published experimental data. The various stages of pendant droplet formation have been examined. These include: necking, bifurcation, recoil, wave generation and secondary necking and bifurcation. The mechanism for the recoiling of the liquid filament after droplet detachment and the subsequent formation of a satellite droplet

has been investigated. Parametric studies on the effects of inlet velocity, surface tension and viscosity have been performed. Controlling factors conducive for satellite droplet formation have been identified.

Electrowetting induced micro-water droplet detachment from the hydrophobic surface has been studied numerically. The results of the numerical model have been validated with published experimental data and the physics of stretching, recoiling and detachment of the droplet have been examined. A parametric study has also been performed in which the effects of droplet volume, voltage amplitude and voltage pulse width have been studied.

Electrowetting induced micro-water droplet transports in parallel-plate and open-plate Electrowetting-on-Dielectrode (EWOD) have been studied numerically. The results of the numerical model have been validated with published experimental data and the physics of droplet transport have been investigated. Velocity and pressure profiles inside the deformed droplet have been analyzed using electrowetting theory. The change of apparent contact angle within the small channel gap has been captured as the droplet is transported in parallel-plate EWOD devices. A parametric study has been performed in which the effects of voltage amplitude, channel gap and electrode size have been examined. Furthermore, the average transport velocity in open-plate and parallel-pate EWOD has been compared.

Table of Contents

List of Illustrations

List of Tables

Chapter 1

Introduction

There is an abundance of surface tension driven flows in daily life, science and technology. These phenomena can be seen from the leaky faucet in kitchen counter to the rain drenched waxed car. The capability of manipulation of droplet using surface tension, empowered an increasing number of engineering applications such as enhancement of phase change heat transfer, cooling of electronic devices, fuel cells, ink-jet printing, electronic displays, fiber optics, nanolithography, adjustable lenses and many biotechnological applications. Analysis of capillary driven flow in microfluidic devices has several challenges associated with it. First, often these processes take place within a length scale of a few millimeters and the actuation is extremely fast. So, the dynamics of such a flow is very hard and sometimes impossible to understand using experimental methods. Second, capillary driven flow involves liquid-solid and/or liquid-liquid interfaces. As the fluid properties such as density and viscosity change sharply across the interface, analytical modeling is also challenging. Third, the capillary dominant flow often involves separation of the continuous fluid body. Non-linear behavior near the vicinity of separation also poses challenges in theoretical analysis.

With the tremendous advancement in computing power over the past few decades, multiphase numerical method is a suitable remedy for the challenges in capillary driven flow. However, even using numerical methods, one still face difficulties. Probably the most imposing of them is to track the interface of a micro-droplet that deforms, moves, merges and separates in response to the surface tension. To capture accurately the surface topology is very important, as it determines the surface tension force acting on the fluid body. Again, the surface tension dominates the pressure and flow field inside the droplet

in a capillary dominant flow which in turn affect the shape of the interface. Such an inter-related dependency among surface tension force, interface topology, capillary pressure and flow field makes the numerical formulation a challenging task.

In numerical modeling of interfacial flow of two immiscible fluids in a fixed grid, a marker function is used that takes different values in different fluids. At every time step, the marker function needs to be updated as the location of the interface changes. In general, there could be two ways to update the marker function. One of them is to advect the marker function itself with the flow field. The interface location is then updated implicitly from the advected marker function. Such an approach of modeling the multiphase flow are called Eulerian and examples include volume-of-fluid (VOF) method [1], level-set (LS) method [2] and phase field method [3]. In general, Eulerian methods are good at capturing phenomena like interface merging and breaking where the interface goes through large topological deformations. However, Eulerian methods suffer from the implicit interface reconstruction. For example, in volume-of-fluid method, this causes the loss of sharpness and accurate orientation of the interface [4]. Even the level set method, which maintains better orientation of the interface shows the tendency of smearing the sharp edges of the interface [5]. In the phase field method, the interface is kept relatively sharp at the expense that the interface is assumed to have a finite thickness [3].

The second broad category of the multiphase flow modeling is Lagrangian method where instead of advecting the marker function, the marker points located on the interface is advected. Thus the interface is tracked explicitly and the marker function is redefined implicitly from the new location of the interface. One of the examples of Lagrangian methods is the front tracking method [6]. Lagrangian methods can preserve the sharpness

of the interface and can track the exact location of the interface. The main objection in Lagrangian methods is when the interface undergoes severe change in topology such as merging and breaking up. In order to overcome this problem, changing the connections among the marker points is required which accounts for increased code complexity [7].

The objective of this study is implementation of suitable multiphase numerical methods to capture the capillary driven flow and understand the physics of it in various micro-fluidic applications. A coupled level set and volume-of-fluid (CLSVOF) method has been developed following the algorithm presented by Gueyffier *et al.* [8] and Wang *et al.* [9]. The developed numerical scheme has been verified using well-established benchmark tests. Both two-dimensional axisymmetric problem such as formation of a pendant drop from a capillary tube and electrowetting induced droplet detachment from the hydrophobic surface and three dimensional asymmetric problem such as electrowetting induced droplet transports in parallel-plate and open-plate EWOD have been studied using developed free surface tracking algorithm.

Chapter 2

Numerical Formulation

Discretization of Momentum Equation

For incompressible fluids, the continuity and momentum equations are given by:

$$\nabla.\vec{\boldsymbol{V}} = 0 \tag{2-1}$$

and

$$\frac{\partial \vec{\boldsymbol{V}}}{\partial t} + \nabla \cdot \left(\vec{\boldsymbol{V}}\vec{\boldsymbol{V}}\right) = -\frac{1}{\rho}\nabla p + \frac{1}{\rho}\nabla \cdot \tau + \vec{\boldsymbol{g}} + \frac{1}{\rho}\overrightarrow{\boldsymbol{F_b}} \tag{2-2}$$

respectively. For Newtonian fluids, we have

$$\tau = 2\mu S \quad and \quad S = \frac{1}{2}\left[\left(\nabla\vec{\boldsymbol{V}}\right) + \left(\nabla\vec{\boldsymbol{V}}\right)^T\right] \tag{2-3}$$

where *S* is the rate-of-strain tensor. Combining Eqs. (2-2) and (2-3) gives the Navier-Stokes equations. Eq. (2-2) is approximated with a finite-difference in time as

$$\frac{\vec{\boldsymbol{V}}^{n+1} - \vec{\boldsymbol{V}}^n}{\delta t} = -\nabla \cdot \left(\vec{\boldsymbol{V}}\vec{\boldsymbol{V}}\right)^n - \frac{1}{\rho^n}\nabla p^{n+1} + \frac{1}{\rho^n}\nabla \cdot \tau^n + \vec{\boldsymbol{g}}^n + \frac{1}{\rho^n}\overrightarrow{\boldsymbol{F_b^n}} \tag{2-4}$$

where the superscripts *n* and *n+1* represent the value of the variable at consecutive time steps. It is decomposed into the following two equations:

$$\frac{\vec{\tilde{\boldsymbol{V}}} - \vec{\boldsymbol{V}}^n}{\delta t} = -\nabla \cdot \left(\vec{\boldsymbol{V}}\vec{\boldsymbol{V}}\right)^n + \frac{1}{\rho^n}\nabla \cdot \tau^n + \vec{\boldsymbol{g}}^n + \frac{1}{\rho^n}\overrightarrow{\boldsymbol{F_b^n}} \tag{2-5}$$

and

$$\frac{\vec{\boldsymbol{V}}^{n+1} - \vec{\tilde{\boldsymbol{V}}}}{\delta t} = -\frac{1}{\rho^n}\nabla p^{n+1} \tag{2-6}$$

where $\vec{\tilde{\boldsymbol{V}}}$ represents an intermediate value of the velocity. The basic algorithm is the two-

step projection method in which a time discretization of the momentum equation, Eq. (2-4), is broken up into two equations, Eqs. (2-5) and (2-6). In the first step, an intermediate velocity field, $\vec{\boldsymbol{V}}$, is computed from Eq. (2-5) which accounts for incremental changes resulting from viscosity, advection, gravity, and body forces. In the second step, the velocity field, $\vec{\boldsymbol{V}}^{n+1}$, is projected onto a zero-divergence vector field resulting in a single Poisson equation for the pressure field given by:

$$\nabla \cdot \left[\frac{1}{\rho^n} \nabla p^{n+1}\right] = \frac{\nabla \cdot \vec{\boldsymbol{V}}}{\delta t} \tag{2-7}$$

which is solved by using an incomplete Cholesky conjugate gradient technique [10].

Free Surface Tracking Algorithm

The main complexity of the numerical simulation is the dynamics of a rapidly moving free surface, the location of which is unknown and is needed as part of the solution. Accurate modeling of the surface tension force involving a high degree of surface curvature is critical. In recent years, a number of methods have been developed for modeling free surface flows [11-13], among which the volume-of-fluid (VOF) and the level set (LS) method are two Eulerian-based methods that have been widely used. One of the advantages offered by these methods is the ease in which flow problems with large topological changes and interface deformations can be handled. These include liquid ligament breakup, droplet elongation and breakup and droplet transport in electrowetting. The VOF method has the desirable property of mass conservation. However, it lacks accuracy on the normal and curvature calculations due to the discontinuous spatial derivatives of the VOF function near the interface. This may lead to convergence problems [14-16] especially in the surface tension force dominant problems. As for the LS method, the normal and curvature can be calculated accurately from the continuous and smooth

distance functions. However, one serious drawback of this method is the frequent violation of the mass conservation. To overcome such weaknesses of the LS and VOF methods, a coupled level set and volume-of-fluid (CLSVOF) method has recently been reported [17-20]. The coupled method offers improved accuracy on the surface curvature and normal calculations while maintaining mass conservation. A CLSVOF method is used in the present study with the interface reconstructed via a piecewise linear interface construction (PLIC) scheme from the VOF function and the interface normal computed from the LS function.

The LS function, ϕ, is defined as a distance function given by:

$$\phi(\vec{\boldsymbol{x}},t)=\begin{cases}>0, & \text{outside of the interface}\\ =0, & \text{at the interface}\\ <0, & \text{inside the interface}\end{cases} \tag{2-8}$$

i.e., negative in the liquid, positive in the air, and zero at the interface. The VOF function, F, is defined as the liquid volume fraction in a cell with its value in between zero and one in a surface cell and zero and one in air and liquid, respectively, i.e.,

$$F(\vec{\boldsymbol{x}},t)=\begin{cases}1, & \text{in the fluid}\\ 0<F<1, & \text{at free surface}\\ 0, & \text{external to fluid}\end{cases} \tag{2-9}$$

A flow chart of the CLSVOF scheme is presented in Figure 2-1. After initialization of the LS and VOF function, they are advanced by the following equations, respectively:

$$\frac{D\phi}{Dt}=\frac{\partial\phi}{\partial t}+(\vec{\boldsymbol{u}}\cdot\nabla)\phi=0 \tag{2-10}$$

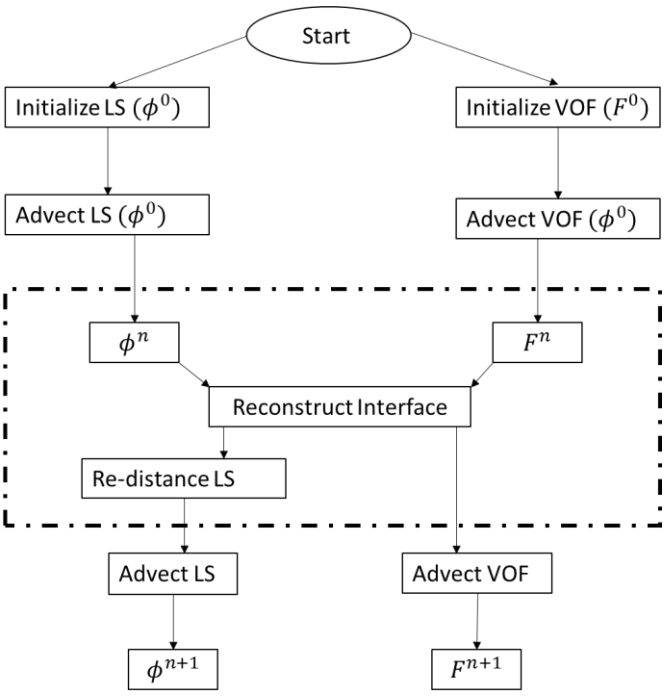

Figure 2-1 Flow chart of the CLSVOF scheme: VOF and LS coupling process in the dashed box

$$\frac{DF}{Dt} = \frac{\partial F}{\partial t} + (\vec{\boldsymbol{u}} \cdot \nabla)F = 0 \tag{2-11}$$

It should be noted that since the VOF function is not smoothly distributed at the interface, an interface reconstruction procedure is required to evaluate the VOF flux across a surface cell. The reconstruction of the interface is an important step for the CLSVOF method where the coupling of VOF and LS functions is accomplished. As the interface is reconstructed, the LS function is required to be redistanced from the new interface. Redistancing serves two purposes. First, the LS function fails to be a distance function after advection and redistancing is needed for its return to a distance function. Second, redistancing from the new interface enables the LS function to achieve mass conservation.

After redistancing, the LS function is advected again according to Eq. (2-10) which is solved using a second order central difference scheme for spatial discretization and a first order explicit scheme for time advancement. In order to avoid excessive numerical error, the VOF function at the interfacial cell is advected using a geometric procedure. In the present study, interface reconstruction and VOF advection have been carried out following the VOF-PLIC and Lagrangian interface propagation scheme presented by Gueyffier *et al.* [8].

A few methods have been reported over the last three decades to reconstruct the interface from the VOF function. Among them, Simple Line Interface Calculation (SLIC) by Noh and Woodward [21], the center of mass algorithm by Sultzmann [22], VOF-PLIC method by Parker and Youngs [23], Least Squares Volume-of-fluid Interface Reconstruction Algorithm (LVIRA) by Puckett [24] and VOF-PLIC method by Gueyffier *et al.* [8] are noteworthy. One of the remarkable features of the interface reconstruction scheme prescribed by Gueyffier *et al.* [8] is that it considerably reduces the complexity of interface reconstruction algorithm in 3D. To reconstruct the interface using this method, one needs to know the VOF function and the interface normal at the computational cell of interest. In the original methodology prescribed by Gueyffier *et al.* [8], the interface normal is also calculated from the VOF information of the neighbouring cells. In the present study the interface normal is calculated from the LS function instead and is given by:

$$\vec{\boldsymbol{n}} = \nabla\phi \tag{2-12}$$

The equation of a planar interface in 3D is given by:

$$n_1 x_1 + n_2 x_2 + n_3 x_3 = \alpha \tag{2-13}$$

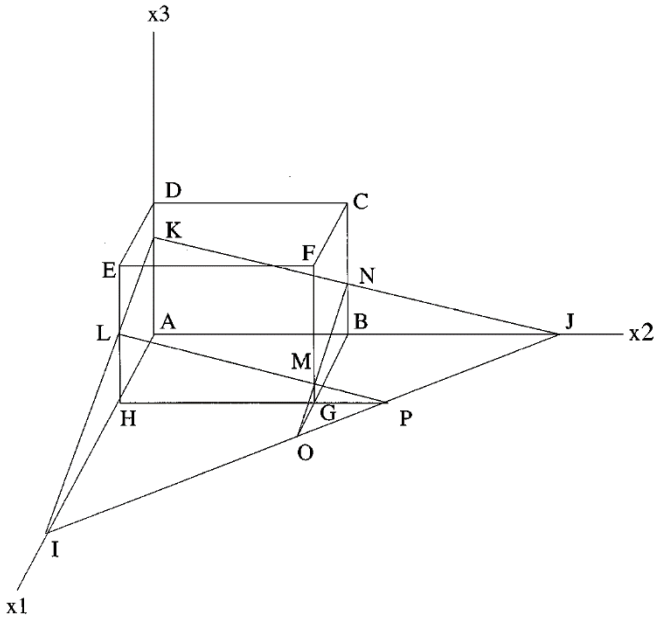

Figure 2-2 Ilustration of the *cut volume* in 3D [8].

where $n_1, n_2 \; and \; n_3$ are the components of unit vector normal to the interface in $x_1, x_2 \; and \; x_3$ directions, respectively and α the shortest distance to the interface from the origin. The parameter α is calculated from *cut volume* [8] which is the volume enclosed by the planar interface within the computational cell. The concept of *cut volume* is illustrated in Figure 2-2 where KNBALMGH, ABCDHGFE and KJI are the *cut volume,* computational cell and planar interface, respectively. The *cut volume* is given by:

$$Volume = \frac{1}{6n_1n_2n_3}\left[\alpha^3 - \sum_{j=1}^{3} H\left(\alpha - n_j c_j\right)\left(\alpha - n_j c_j\right)^3 + \sum_{j=1}^{3} H\left(\alpha - \alpha_{max} + n_j c_j\right)\left(\alpha - \alpha_{max} + n_j c_j\right)^3\right] \quad (2\text{-}14)$$

where c_j is the dimension of the computational cell in x_j direction, α_{max} $(= n_1c_1 + n_2c_2 + n_3c_3)$ the distance from the origin to the furthest corner of the computational cell and H the Heaviside step function defined as:

$$H(x) = \begin{cases} 0 & \text{for } x < 0. \\ 1 & \text{for } x > 0. \end{cases} \tag{2-15}$$

Note that in Eq. (2-14), *cut volume* is a function of the unknown parameter α and its derivative with respect to α can readily be calculated. It should also be noted that there is an alternative way to calculate the *cut volume* by multiplying the VOF function with corresponding cell volume. Considering these facts, finding α becomes a simple root finding problem which is solved in the present study using Newton's method.

Once the interface has been reconstructed, the VOF fluxes across the cell are calculated using the Lagrangian interface propagation scheme in which the interface segment is assumed to be propagated in each spatial direction with an operator splitting strategy. The equation of the interface at any given time step n is given by:

$$n_1^{(n)}x_1^{(n)} + n_2^{(n)}x_2^{(n)} + n_3^{(n)}x_3^{(n)} = \alpha^{(n)}. \tag{2-16}$$

At first, the interface is propagated in x_1 spatial direction as shown in Figure 2-3 at a linearly interpolated velocity given by:

$$u_1(x_1) = U_0\left(1 - \frac{x_1}{h}\right) + \frac{U_h x_1}{h} \tag{2-17}$$

where U_0 and U_h are the x_1 direction velocity component at the left and right face of the computational cell, respectively and *h* the dimension of the cell along the x_1 direction. Since this interpolated velocity is assumed to be constant over the advection time step δt, the x_1 coordinate of each point at the interface segment is updated as:

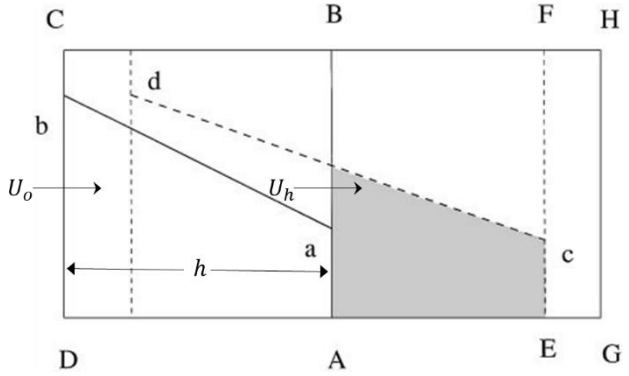

Figure 2-3 Lagrangian interface propagation scheme [8].

$$x_1^{(*)} = x_1^{(n)} + u_1\left(x_1^{(n)}\right)\delta t = \left[1 + \frac{U_h - U_0}{h}\delta t\right] x_1^{(n)} + U_0 \delta t \tag{2-18}$$

where the superscript (*) is used to denote fractional step. Eq. (2-18) can be rearranged as:

$$x_1^{(n)} = \frac{x_1^{(*)} - U_0 \delta t}{1 + \left(\frac{U_h - U_0}{h}\right)\delta t}. \tag{2-19}$$

During the operator split advection in x_1 direction, $x_2^{(n)}$and $x_3^{(n)}$ remain constant. The equation of the advected interface can be obtained by plugging the expression for $x_1^{(n)}$ into Eq. (2-16) which is given by:

$$n_1^{(*)} x_1^{(*)} + n_2^{(*)} x_2^{(*)} + n_3^{(*)} x_3^{(*)} = \alpha^{(*)} \tag{2-20}$$

where

$$n_1^{(*)} = \frac{n_1^{(n)}}{1 + \left(\frac{U_h - U_0}{h}\right)\delta t} \tag{2-21}$$

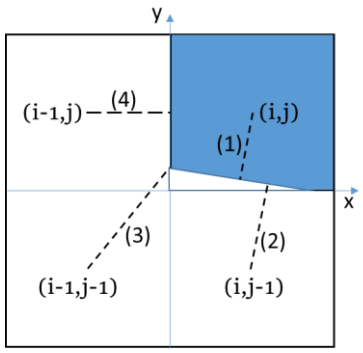

Figure 2-4 Redistancing of the LS function. Dashed lines are the shortest distances from the cell center to the interface.

and

$$\alpha^{(*)} = \alpha^{(n)} + \frac{n_1^{(n)} U_0 \delta t}{1 + \left(\frac{U_h - U_0}{h}\right)\delta t} \tag{2-22}$$

while all other variables remain same as in Eq. (2-16). The advected interface given by Eq. (2-20) is checked to see if it has been reached to the left or right cell. The protruded volumes will then be calculated using a modified version of Eq. (2-14). Thus the VOF fluxes during x_1 advection are calculated which is followed by similar flux calculation in x_2 and x_3 direction. The VOF function for the whole computational domain is updated after each directional sweep and its value at n+1 time step is obtained once all three sweeps are done.

Several researchers have prescribed the LS redistancing algorithm for 2D axisymmetric and 3D formulation [9,17-20]. In the present study, the redistancing has been carried out by following a geometric approach outlined by Wang *et al.* [9] in which the shortest distance from the cell center to the reconstructed interface is calculated. As

demonstrated in the 2D illustration shown in Figure 2-4, the closest point could be one of the vertices of the interface (case 3), or the projection point of the neighbouring cell center to the interface (case 1 and 2), or the cell face center (case 4). The details of the redistancing algorithm can be found in [9].

Surface Tension Force Modeling

Continuum surface force (CSF) method has been used to model surface tension [25]. The CSF method interprets surface tension as a continuous, three-dimensional effect across an interface rather than as a boundary value condition at the interface. Interfaces between fluids of different properties are represented as transition regions of finite thickness. Across this region there is a continuous variation of the property value of one fluid to the property value of the other fluid. The surface tension volume force that is only active inside the transition region is given by:

$$\boldsymbol{F}_b = \sigma\delta(x)\kappa(\vec{\boldsymbol{x}})\hat{\boldsymbol{n}} \tag{2-23}$$

where σ is the surface tension coefficient, $\delta(x)$ a delta function concentrated on the interface, $\hat{\boldsymbol{n}}$ the unit vector normal to the free surface. The free surface curvature $\kappa(\vec{\boldsymbol{x}})$ is given by:

$$\kappa(\vec{\boldsymbol{x}}) = -(\nabla\cdot\hat{\boldsymbol{n}}) = \frac{1}{|\vec{\boldsymbol{n}}|}\left[\left(\frac{\vec{\boldsymbol{n}}}{|\vec{\boldsymbol{n}}|}\cdot\nabla\right)|\vec{\boldsymbol{n}}| - (\nabla\cdot\vec{\boldsymbol{n}})\right] \tag{2-24}$$

where

$$\hat{\boldsymbol{n}} = \frac{\vec{\boldsymbol{n}}}{|\vec{\boldsymbol{n}}|} \quad and \;\; \vec{\boldsymbol{n}} = \nabla\phi \tag{2-25}$$

When a droplet is placed on a solid surface, it reaches a state of equilibrium by balancing the intermolecular cohesive and adhesive force within the liquid and liquid-solid boundary respectively. At equilibrium, the liquid-gas interface makes a static contact angle with the solid surface given by the Young's equation:

$$\sigma_{SG} - \sigma_{SL} - \sigma_{LG}\cos\theta_0 = 0 \tag{2-26}$$

where σ_{SG}, σ_{SL} and σ_{LG} are the solid-gas, solid-liquid and liquid-gas surface tension, respectively and θ_0 is the static equilibrium contact angle. In the present study, a wall adhesion scheme in the CSF framework [26] is used in which the unit vector normal to the liquid-solid interface is given by:

$$\hat{\boldsymbol{n}} = \hat{\boldsymbol{n}}_w \cos\theta_0 + \hat{\boldsymbol{t}}_w \sin\theta_0 \tag{2-27}$$

where $\hat{\boldsymbol{n}}_w$ and $\hat{\boldsymbol{t}}_w$ are the unit vectors normal and tangential to the wall, respectively. It is used to calculate the interface normal at the wall rather than Eq. (2-25), prior to calculating the curvature from Eq. (2-24). The curvature is then used in Eq. (2-23) to calculate the wall adhesion force that drives the fluid to comply with the static contact angle. This method does not strictly impose the contact angle at the solid-liquid boundary, rather its influence on the momentum equation [27].

Verification Study

Advection Tests

Three different advection tests have been carried to verify the accuracy of CLSVOF method used in present study. In the first advection test, shown in Figure 2-5, a slotted disk of radius 15.0 with slot width 5.0 is placed at (50.0,75.0) in a

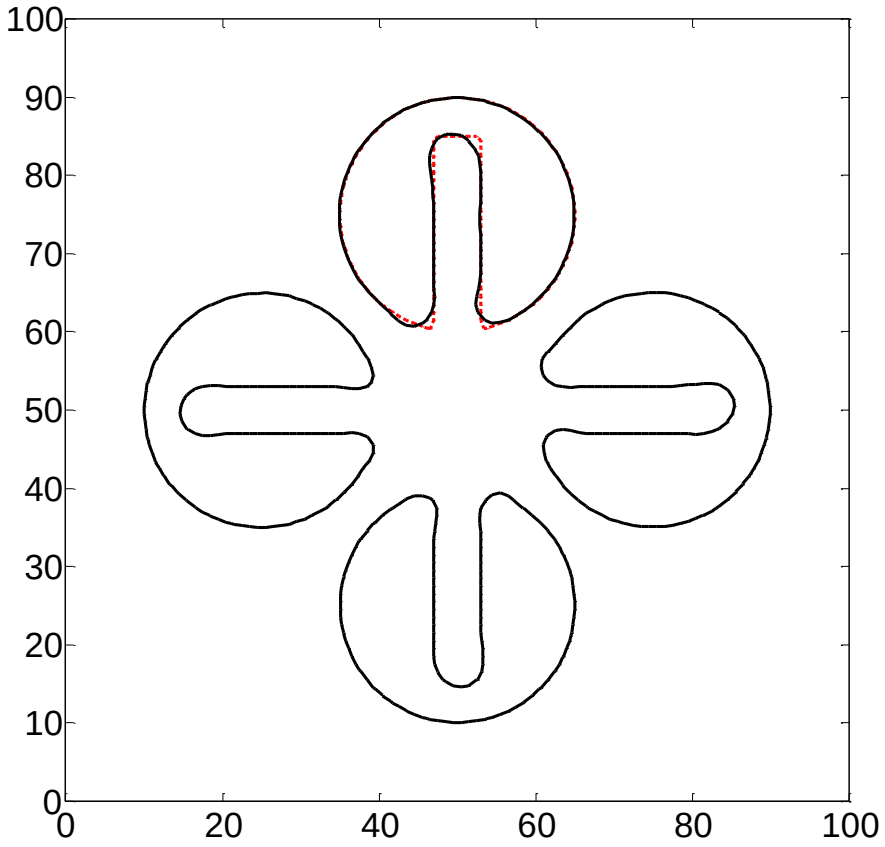

Figure 2-5 Solid body rotation of a slotted disc.

100X100 computational domain. The disc is rotated in a prescribed flow field given by:

$u = (\pi/314)(50 - y)$

$v = (\pi/314)(x - 50)$

In Figure 2-5, the initial shape of the disc is shown in red dashed line and as the disc is rotated counter clockwise, the 90˚, 180˚, 270˚ and 360˚ rotations have been shown in black solid lines. It is found that the shape of the fluid body remains nearly same after one full rotation although the slot edges get smeared. The relative mass error is found to be 0.00016%.

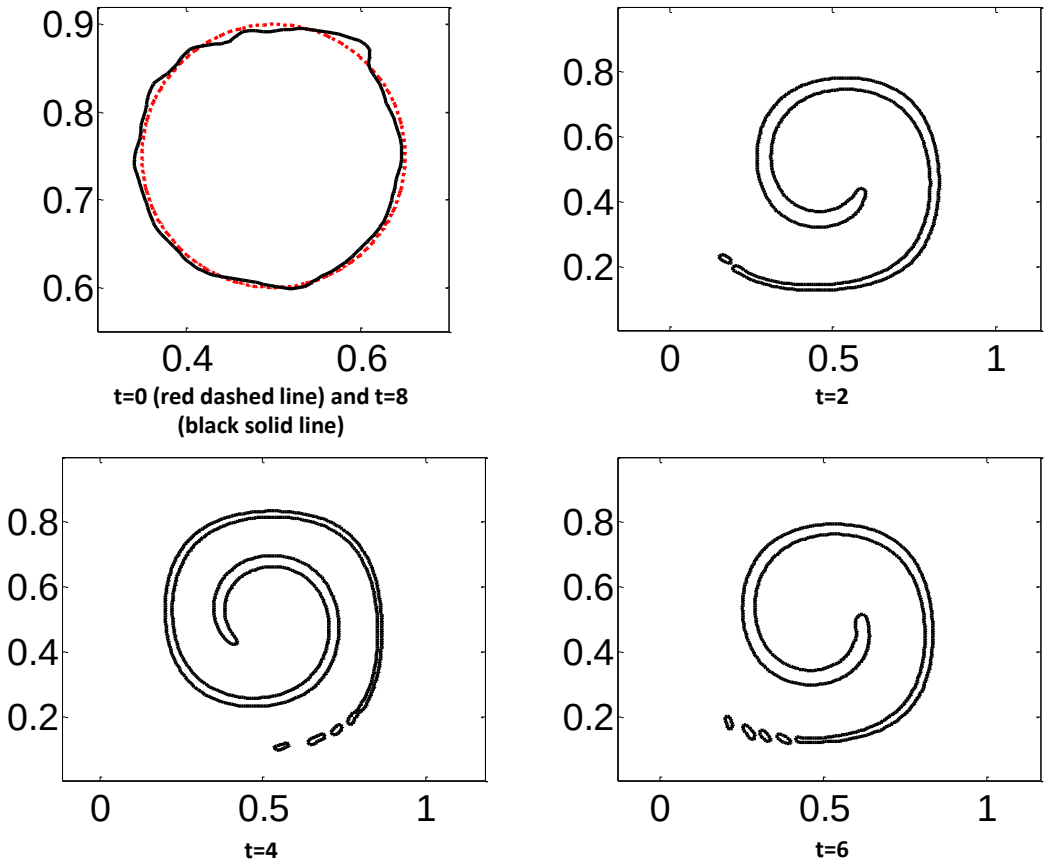

Figure 2-6 Vortex flow advection test

The second advection test is aimed at assessing the interface construction accuracy where the fluid body goes through severe topological changes. Once again, a circle of radius 0.15 is placed at (0.5, 0.75) in a computational domain of 1.0X1.0. The domain contains 128 computational cells in each direction. Here, the circle is subjected to a vortex flow which is given by:

$$u = (\sin(\pi x))^2 \sin(2\pi y) \cos\left(\frac{\pi t}{T}\right)$$

$$v = -(\sin(\pi y))^2 \sin(2\pi x) \cos\left(\frac{\pi t}{T}\right)$$

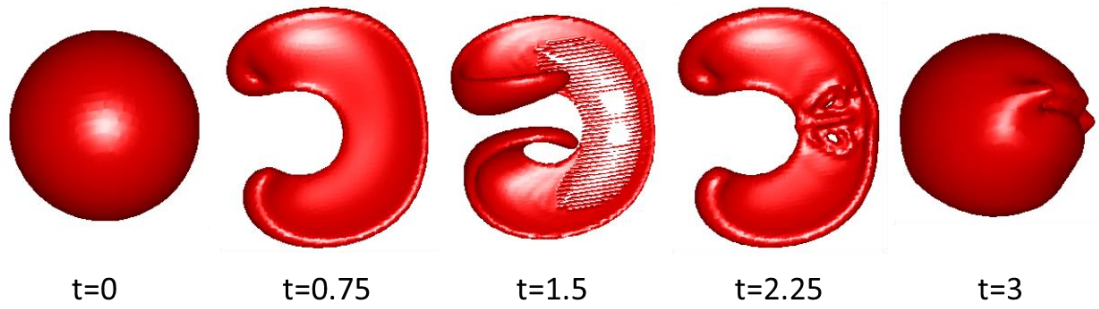

Figure 2-7 Advection of a sphere in a 3D vortex flow.

where the parameter T is set to 8.0. Unlike the first test, the vortex flow produces a thin filament as shown in Figure 2-6 and the deformation reaches its maximum at t=4.0. After that the filament is rotated back to create the initial circular shape at t=8.0. The CLSVOF method is able to capture the filament even at its maximum deformation, although the tail of the filament gets fragmented. The recovered shape at t=8.0 matches well with the initial circular shape. The relative mass error of the reconstructed circle is found to be 0.17%.

The third advection test is carried out to analyze the deformation of a sphere in 3D. A sphere of radius 0.15 is placed at (0.35,0.35,0.35) in a 100X100X100 computational domain which is subjected to a 3D vortex flow given by:

$$u = 2\sin^2(\pi x)\sin(2\pi y)\sin(2\pi z)\cos\left(\frac{\pi t}{T}\right)$$

$$v = -\sin(2\pi x)\sin^2(\pi y)\sin(2\pi z)\cos\left(\frac{\pi t}{T}\right)$$

$$w = -\sin(2\pi x)\sin(2\pi y)\sin^2(\pi z)\cos\left(\frac{\pi t}{T}\right)$$

where the parameter T is set to 3.0. The above flow field stretches the sphere creating two rotating vortices and the maximum deformation is attained at t=1.5. As can be seen from Figure 2-7, the mid-section of the filament breaks up due to the excessive stretching at

t=1.5. The flow field is then reversed and the fluid body is restored to almost its initial spherical shape at t=3.0. The maximum relative mass error is 0.74% for this test.

Implementation of Static Contact Angle

As the modelling of contact angle carries great importance in this numerical study, successful implementation of static contact angle using 3D CLSVOF scheme is demonstrated in Figure 2-8. In this validation test, a hemispherical droplet of 0.5 mm radius with 90˚ contact angle was initialized in a 2.0X2.0X2.0 mm^3 computational domain with a 0.05mm uniform grid spacing. The final steady shapes of the droplet for the various prescribed contact angles are shown in the figure. The red line represents the angle that was prescribed in the wall boundary condition of the code and the blue line represents the equilibrium shape of the droplet. The red line can be seen to be tangential to the interface at the three phase contact line, thus demonstrates the accuracy of the method employed.

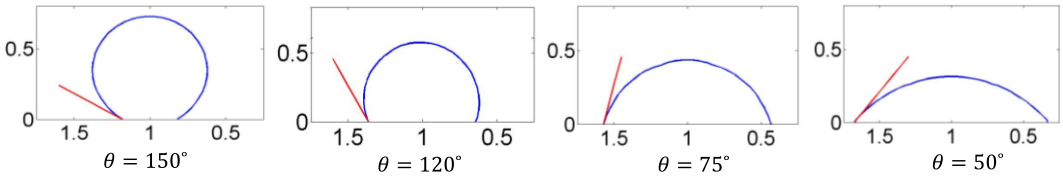

Figure 2-8 Implementation of various static contact angles.

Comparison between 2D Axisymmetric and 3D Free Surface Flows

Pendant drop formation from a vertical capillary tube has been simulated using both 2D axisymmetric and 3D model in which a nozzle of 0.9mm length with 0.8mm inner radius is used. The computational domain and the nozzle used in 3D simulation are shown

in Figure 2-9. Note that in order to conserve computational resources, only a quarter of actual domain has been simulated and a rigid free slip boundary condition (no fluid motion across the boundary with zero shear stress) has been applied along the plane of symmetry. Uniform grid size of 0.05mm has been used which is based on the results of a grid refinement study presented in the Appendix. As water is supplied through the nozzle inlet at 0.08m/s uniform velocity, a pendant droplet slowly grows at the nozzle tip and eventually detaches as shown in Figure 2-10.

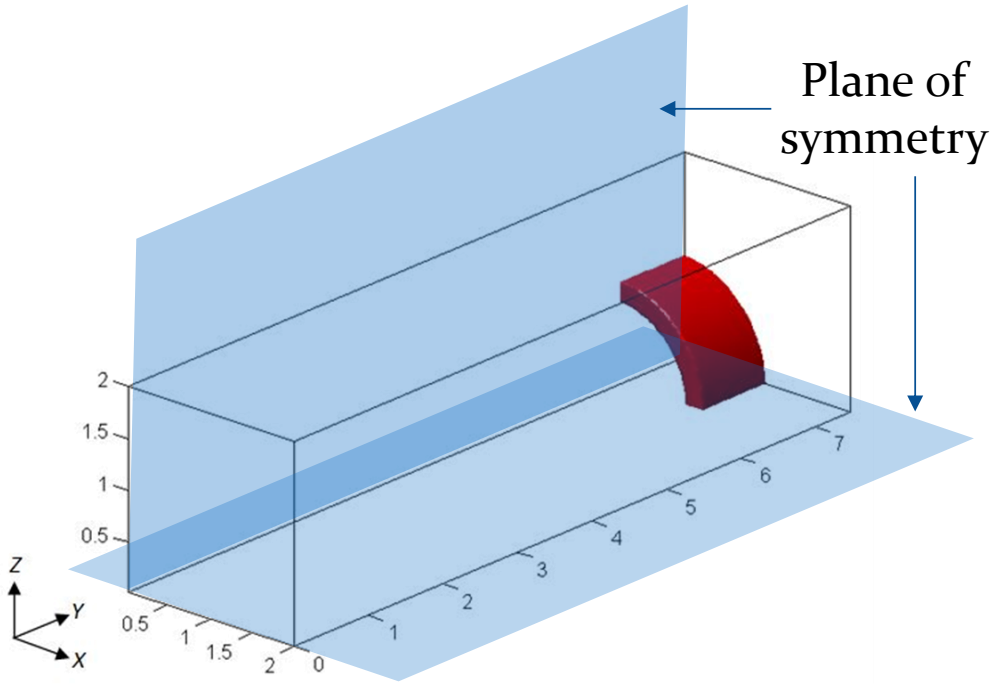

Figure 2-9 Computational domain and nozzle for pendant droplet simulation

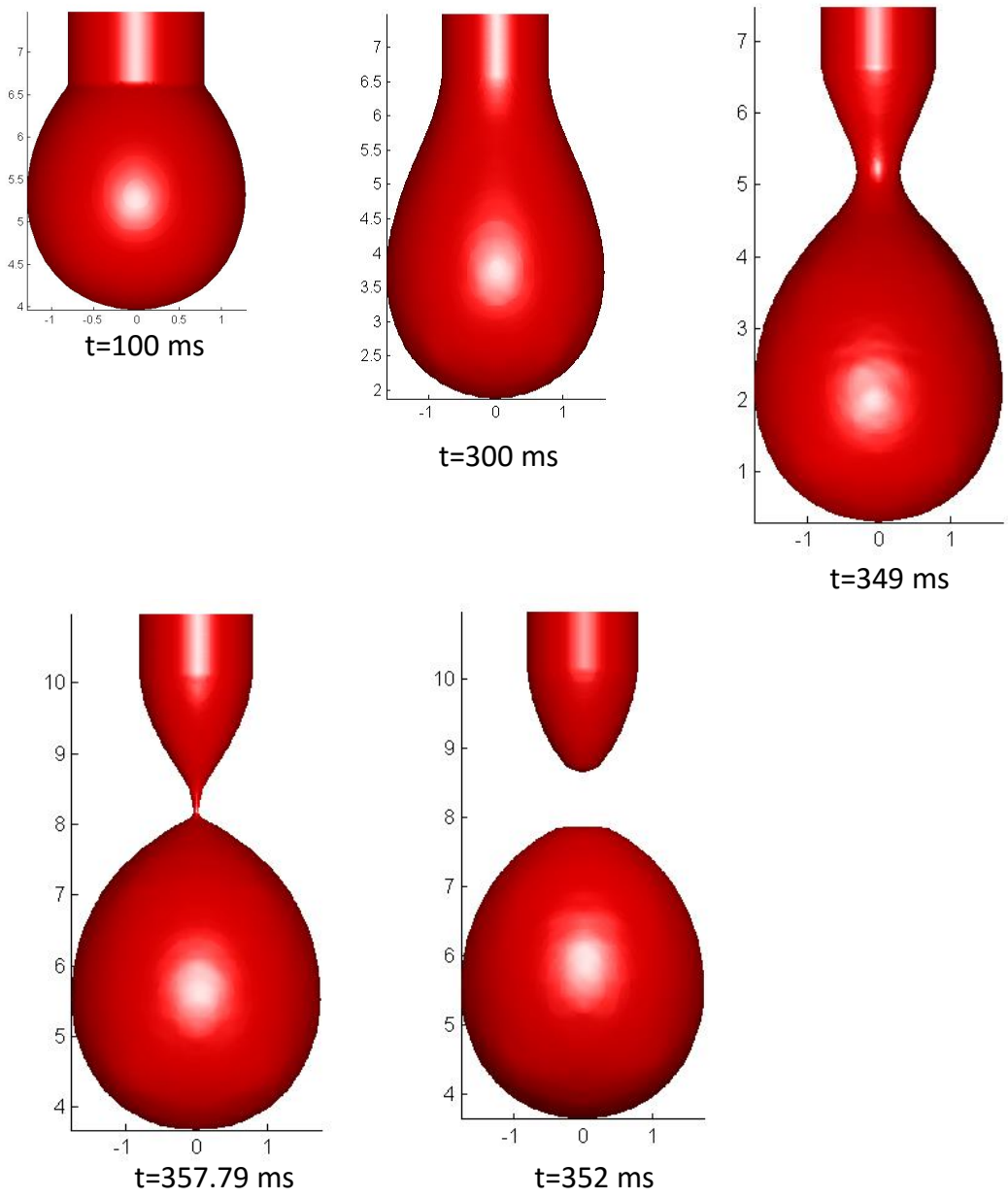

Figure 2-10 Evolution and detachment of a pendant droplet in 3D.

In Figure 2-11 pendant droplet at the instant of detachment has been compared between 2D axisymmetric and 3D model. Detachment takes place almost at the same time in both numerical models. Length of the total liquid column and size of the spherical droplet

are nearly same. An opposite downward and upward flow can be seen just below and above the neck, respectively in both cases.

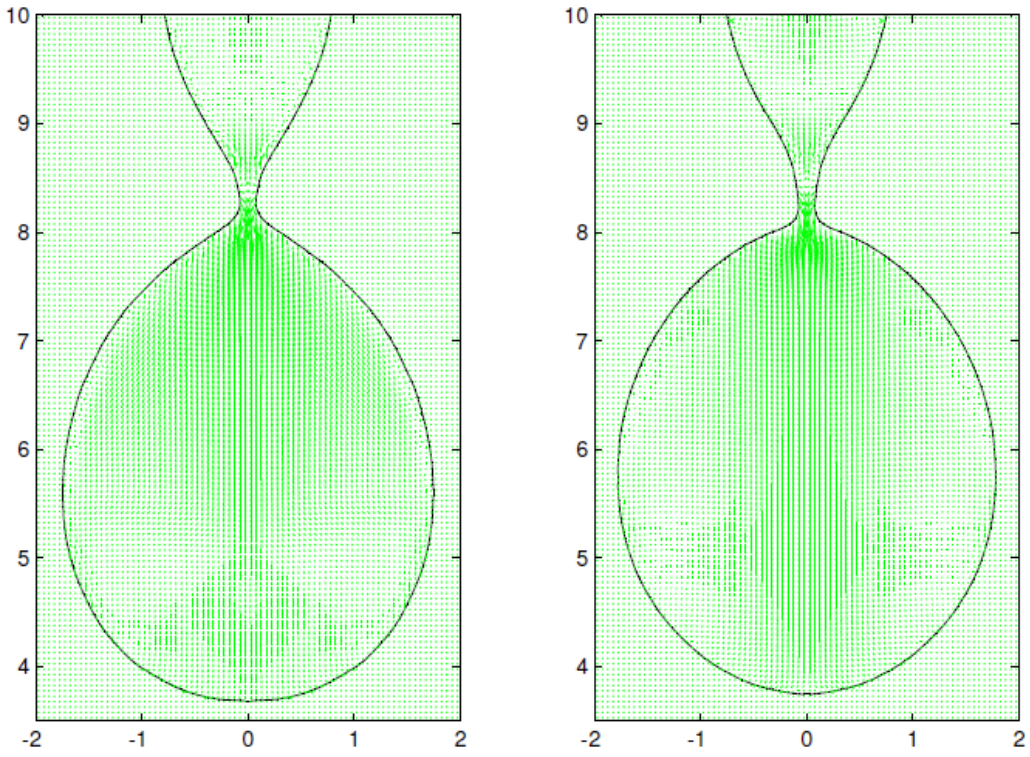

Figure 2-11 Comparison between 2D axisymmetric and 3D pendent droplet simulation.

Chapter 3

Dynamics of Satellite Droplet Formation

Introduction

The evolution and breakup of a drop falling from an orifice under the action of gravity has been of considerable interest in fluid dynamics due to its wide engineering application such as inkjet printing, DNA microarraying, cell and organ printing and blood oxygenation. Due to the diversity of its application, the problem has been studied by a number of researchers [28-41]. According to the published literature, at low flow rates when a droplet forms from the orifice, it suffers instability as it grows in size. The instability is caused by the fact that the gravitational force becomes sufficiently large that the surface tension is unable to hold the liquid onto the orifice. Subsequently a neck begins to develop

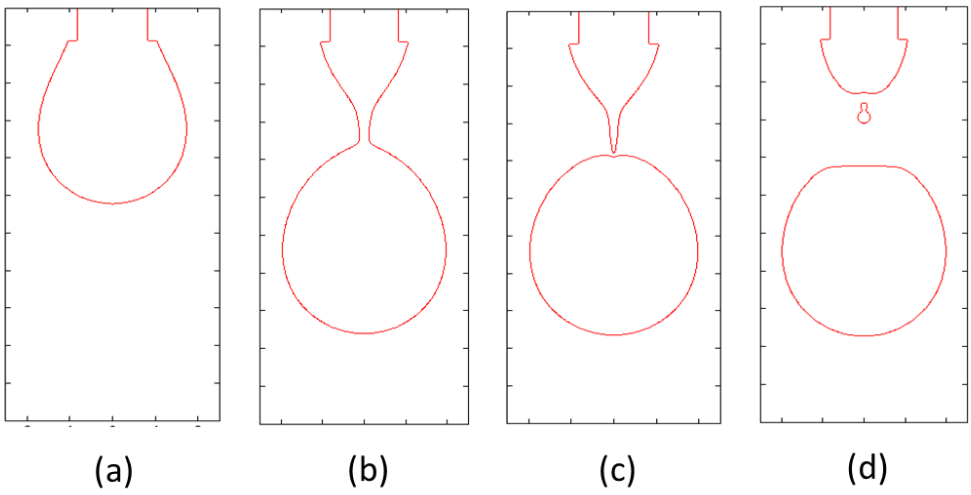

Figure 3-1 Schematic of pendant droplet and subsequent satellite droplet generation; a) spherical droplet hanging from the nozzle b) liquid cone, filament and spherical droplet, c) instant of primary bifurcation and d) satellite droplet.

along with the formation of a cylindrical liquid filament that connects the spherical droplet at the bottom to the liquid cone at the top as outlined in Figure 3-1(b). The first pinch off occurs at the bottom end of the filament that produces a primary droplet and sometimes, immediately after the first pinch off, it is followed by a secondary bifurcation at the top end of the filament where it is attached to the liquid cone creating a satellite droplet of much smaller volume as shown in Figures 3-1(c) and 3-1(d). It has been reported that in between the primary and secondary bifurcation the liquid filament recoils upward due to the unbalanced surface tension force with the development of a capillary wave along the interface [28].

It has been observed that the mechanism of secondary bifurcation is almost identical in nature to that of primary bifurcation [28-30]. The leaky faucet problem was investigated by Schulkes [29] using boundary integral method for inviscid fluid. It was reported that the pressure gradient is steepest at the point where curvature of the capillary surface changes most rapidly. As a result, volume flux out of the liquid filament is also largest at this point. Curvature change of the surface is largest where the liquid filament is connected to the spherical droplet. Therefore pinch off occurs first at this point rather than the cone-filament junction. After the primary bifurcation, the cone-filament junction becomes the point where the pressure gradient is steepest and a second neck begins to develop there and in a similar fashion, the liquid filament is bifurcated from the liquid cone forming satellite droplet. However, in many occasions, the liquid filament may successfully recoil upward without producing any satellite droplet, the phenomenon that cannot be properly explained with this analysis.

Droplet formation in a two-fluid system has been studied numerically by Zhang and Stone [30] using the boundary integral method for Stokes flow. It was reported that the satellite droplet formation depends primarily on the shape of the filament at the

instant of primary bifurcation. The effects of viscosity ratio and the Bond number on the satellite droplet formation have also been studied.

An experimental study on pendant droplet has been carried out by Zhang and Basaran [31] where the possibility of satellite droplet formation was studied by examining two dimensionless parameters: relative elongation ratio and relative interaction time. The relative elongation of the thread is defined as the ratio of the thread length l_d to its average radius a_0 at the instant when the thread is about to break for the first time and the dimensionless interaction time is the time interval that elapses between primary and secondary bifurcation, scaled by a capillary time $\sqrt{\rho l_d a_0^2/\sigma}$, where ρ and σ are the density and surface tension coefficient of the fluid, respectively. It has been reported that both of these ratios increase with the decrease of tube radius. Thus, when the tube radius is sufficiently small, the relative elongation of the filament is so large and the time for the filament to roll up is so short compared to its interaction time that the secondary breakup of the thread is entirely suppressed. However, the dynamics for which the interaction time increases with the decrease of nozzle radius was not addressed. Again, it is not clearly understood why the time to roll up the filament should be small if the relative elongation ratio increases.

Dynamics of a viscous pendant drop at low flow rate have been studied numerically using the volume-of-fluid method by Zhang [32]. According to that study, generation of a satellite droplet depends primarily on two factors: the deformation of the liquid cone that joins to the upper end of the filament and the time interval that elapses between the breakup of the two ends of the filament. It has been reported that as the flow rate increases, the relative elongation of the liquid cone increases and thus it becomes more difficult for the surface tension to restore the apex of the cone-shaped liquid mass to near-spherical form when competing with increasing inertial force. Therefore, more time is required for the

secondary rupture of the filament at its joining point with the liquid cone. When the flow rate is sufficiently high, the secondary breakup can no longer occur before the filament rolls up and coalesces with the liquid cone. In the present study it has also been found that surface tension force weakens when flow rate is increased although it does not weaken when competing with increasing inertial force but it weakens due to a relatively smooth cone-filament junction. However, the physics for which this weaker surface tension force becomes inadequate to compete with increased inertial force and thereby fails to restore the spherical apex was not analyzed. In other words, how these two opposing force affect the flow field at the cone-filament junction and thereby determines the fate of generation of satellite drop is not clear from this theory.

Parametric study on the satellite drop formation has also been carried out by some researchers [32-35]. Based on experimental and numerical results, Zhang [32] has proposed an empirical relation:

$$We.G^{0.3921} = K$$

where *We* the Weber number, *G* the Bond number and *K* a constant. If the value of *K* is less than 0.0125 then it leads to satellite drop formation. Another parametric study on the generation of satellite drops has been conducted by Ambravaneswaran *et al.* [33]. It has been reported that if the Ohnesorge Number (*Oh*) is fixed, there exists a critical *We*, above which no satellite drops are produced and below which satellite drops are always produced. The locus of the critical values of *We* varies nonmonotonically with *Oh*. The effect of nozzle shape and radius on the satellite drop formation has been examined experimentally by D'Innocenzo *et al.* [34]. It has been reported that if the orifice is beveled, the presence of satellite drops is greatly reduced and if the diameter of the nozzle is less than 0.36mm, satellite drop formation is not observed. The evolution of the detached liquid filament created by the secondary bifurcation into a spherical drop has been experimentally

captured by Notz *et al.* [41] using high speed digital camera. In that study, a 2D finite element method has also been used to analyze the evolution of detached filament numerically.

Based on the above discussion and literature review, it is concluded that although there are a lot of studies on the dynamics of dripping faucet, proper understanding of the mechanism of satellite droplet formation is still lacking which is the objective of this study. It has been accomplished numerically by solving the unsteady Navier-Stokes equations for Newtonian fluid along with a robust free-surface tracking scheme. Also, the dynamics of the recoiling of liquid filament after primary bifurcation has been investigated and the physics of capillary wave development have been analyzed.

Results and Discussion

Dynamics of Pendant Drop Formation

In Figure 3-2, pendant drop formation from a vertical capillary tube has been compared between experimental [28] and numerical study. Water at a very low flow rate has been supplied through the nozzle of 5.2mm outer diameter in both cases. For the numerical simulation, dimensionless Weber $(\rho V^2 l/\sigma)$ and capillary $(\nu V\rho/\sigma)$ numbers are $1.78X10^{-3}$ and $6.91X10^{-5}$, respectively. As shown in Figure 3-2, a good agreement in size and shape of the liquid cone, filament, primary and satellite droplets between simulation and experiment has been achieved. In each image, nozzle size and position have been matched between numerical simulation and experiment to compare rest of the liquid column. Note that the locations of the filament and satellite droplet in the experiment are eccentric whereas they are at the center in numerical simulation.

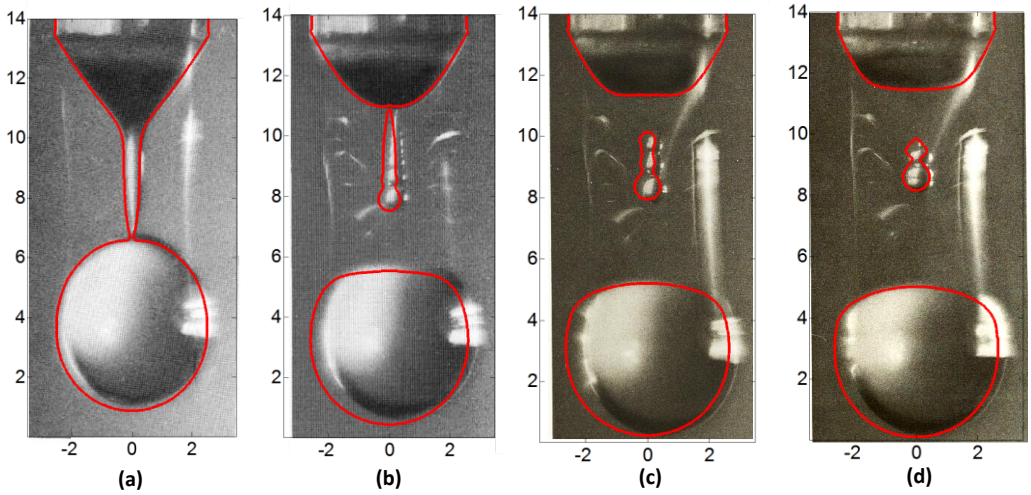

Figure 3-2 Comparison between numerical (red line) and experimental study [28] at the instant of a) primary and b) secondary bifurcation. c) and d) evolution of satellite droplet.

According to Peregrine *et al.* [28], growth and breakup of viscous pendant drops can be described in six stages. These are: necking, bifurcation of the main drop, recoiling, wave generation, secondary necking and bifurcation and final phase of motion. In this numerical study, the evolution of the pendant drop up to the secondary bifurcation has been examined by analyzing the pressure and velocity profiles. In general, the pressure change in the radial direction is small compared to that in the axial direction and the flow field is primarily dominated by the axial velocity which can be seen from Figure 3. Although, unidirectional downward flow exists in most of the region of liquid column, some circulations are also present in the region close to the free surface which is more prominent during the pre-necking stage of pendant drop (t=198ms, Figure 3-3). As these circulations are localized near the surface of spherical drop and not present in the vicinity of necking and detachment region as can be seen at t=433.9ms in Figure 3-3, the necking and bifurcation of the pendant drop is dominated by the axial flow. It has been

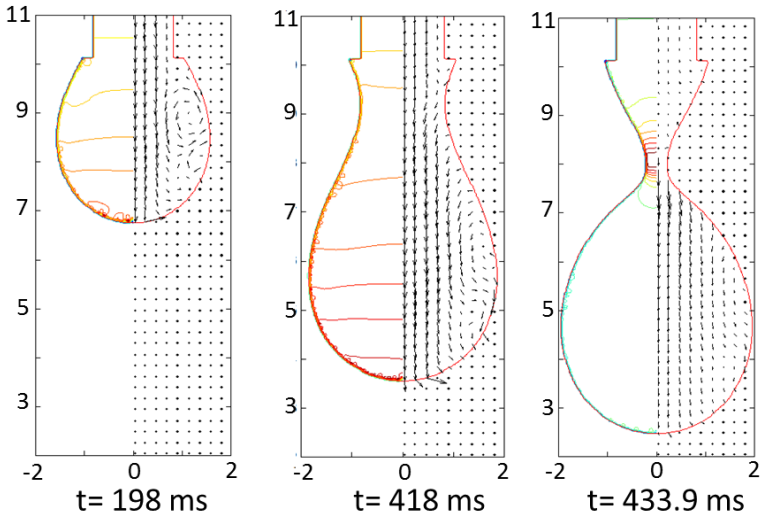

Figure 3-3 Velocity vectors and pressure contours at various stages of the pendant drop formation.

also reported by Zhang [32] that the flow pattern is dominated essentially by the unidirectional downward flow during the drop necking and detaching period. So, the analysis presented in this study is carried out by analyzing the pressure and axial velocity along the center axis. However, 2-D velocity field has also been presented, where radial velocity also plays an important role. To understand the dynamics of the various stages of the growth and breakup of pendant drops, a water like fluid with kinematic viscosity of $1.005\times10^{-6}m^2/s$, surface tension coefficient of $7.27\times10^{-2}\,N/m$ and density of 1000 kg/m^3, has been simulated at $0.05\ m/s$ inlet velocity. Nozzle length is set to be 1.9mm with 0.8mm inner and 1.05mm outer radius for all of the cases. In order to conserve computational resources, computations are performed in an axisymmetric domain of dimensions $12.0mm\times2.6mm$. A time and grid convergence study has also been performed and the results are given in the Appendix.

i. Necking

At the initial stage of necking, surface tension maintains an almost spherical shape of the pendant drop as it grows slowly at the tip of the nozzle. However, as the pendant drop gains volume, it suffers from gravity induced straining. As shown in Figure 3-4, at t=418ms, the pressure profile along the axis of the liquid column is almost linear, which indicates that gravity plays an important role at this stage of the drop formation. As the drop grows a neck gradually develops in the liquid column as can be seen in Figure 3-4, t=433.44ms. During this stage, flow is downward and also there is a pressure rise in the neck region due to large radial curvature of free surface. Thus increase in pressure at the neck acts as a barrier for the downward fluid velocity. Pressure gradient opposes the downward flow upstream of the neck and it favors the same flow downstream of the neck.

In the final stage of necking, a thin filament is formed between the liquid cone and the spherical drop as shown in Figure 3-4 at t=434.96ms. The formation of the liquid filament takes only 1.5~2.0ms. It is a very small time scale when compared to the overall neck formation time of 435ms. At the cone-filament junction, the liquid cone transforms sharply into a thin liquid filament and the radius of the filament decreases continuously from the cone-filament junction to the filament-sphere junction. As a result, pressure rises sharply at the cone-filament junction and it continues to rise as long as the radius of the filament decreases.

From Figure 3-4 at t=434.96ms, it is shown that the steep pressure gradient at the cone-filament junction drives the fluid upward and the pressure gradient at the filament-sphere junction squeezes the fluid downward. Thus flow is separated around the midsection of liquid filament. For the sake of discussion, the upward flow at the cone-filament junction is referred to as the tertiary recoiling flow and the downward flow at the

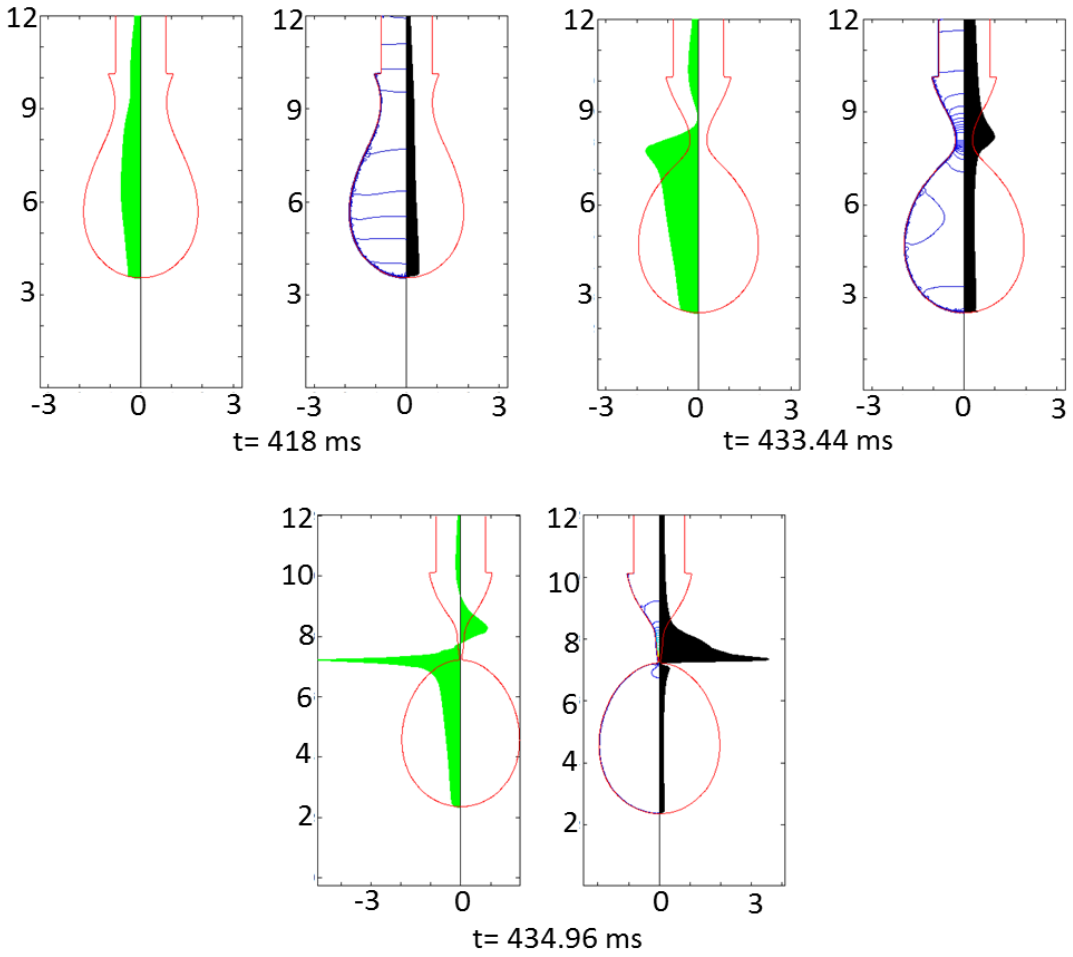

Figure 3-4 Necking: Left, axial velocity and RIGHT, pressure distribution along the center axis of the liquid column.

filament-sphere junction is referred to as the primary extending flow. From the consecutive axial velocity profiles shown in Figure 3-5, it can be seen that the acceleration of the primary extending flow is stronger than that of the tertiary recoiling flow. There are two reasons behind it, first, the geometry of the free surface changes from slightly convex to concave at the filament-sphere junction. Due to negative lateral curvature of the free

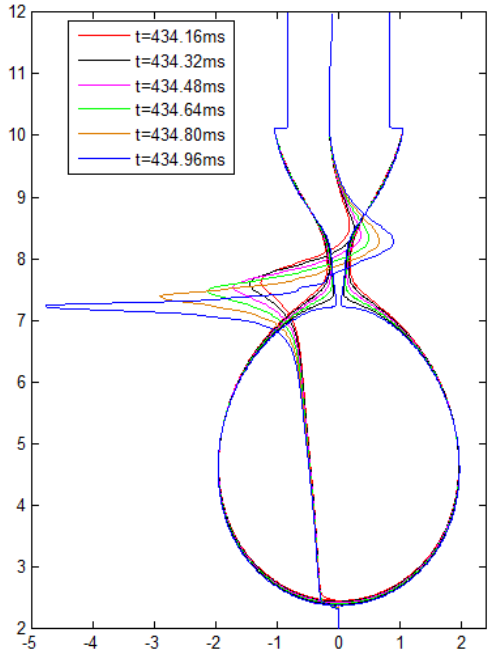

Figure 3-5 Consecutive axial velocity profiles along the center axis during primary bifurcation

surface, the capillary pressure plummets sharply at the filament-sphere junction. Thus pressure gradient in this location is steeper than that of the cone-filament junction, as shown in Figure 3-4, at t=434.96ms. Similar physics has been demonstrated by Tong and Wang [42] to explain the end-pinching mechanism of liquid ligament. And the second reason is that the pressure gradient acts against inertia and gravity to develop upward recoiling flow but the pressure gradient is aided by gravity while developing the downward extending flow.

Note that the separation point of primary extending and tertiary recoiling flow is located slightly above the maximum pressure point at t=434.96 ms. This is because the strength of these two opposite flow fields are not the same. The stronger downward primary extending flow originates from the center of the liquid filament although the pressure

gradient is pushing upward at that location. The extending and recoiling flows stretch the liquid filament at the bottom and top ends, respectively, and consequently produces an elongated tapered shape filament as shown in Figure 3-5.

ii. Bifurcation

From Figure 3-6 at t=435.04ms, the liquid column is bifurcated at the filament-sphere junction due to the primary extending flow. One can think that the cone-filament junction is another potential location for the bifurcation due to the tertiary recoiling flow. However, the first bifurcation always occur at the filament-sphere junction because of the stronger flow field. This phenomenon has also been noted by Schulkes [29] where it has been explained that the bifurcation occurs where pressure gradient is maximum. In this case, the filament-sphere junction has the maximum pressure gradient (Figure 3-4 , t=434. 96 ms).

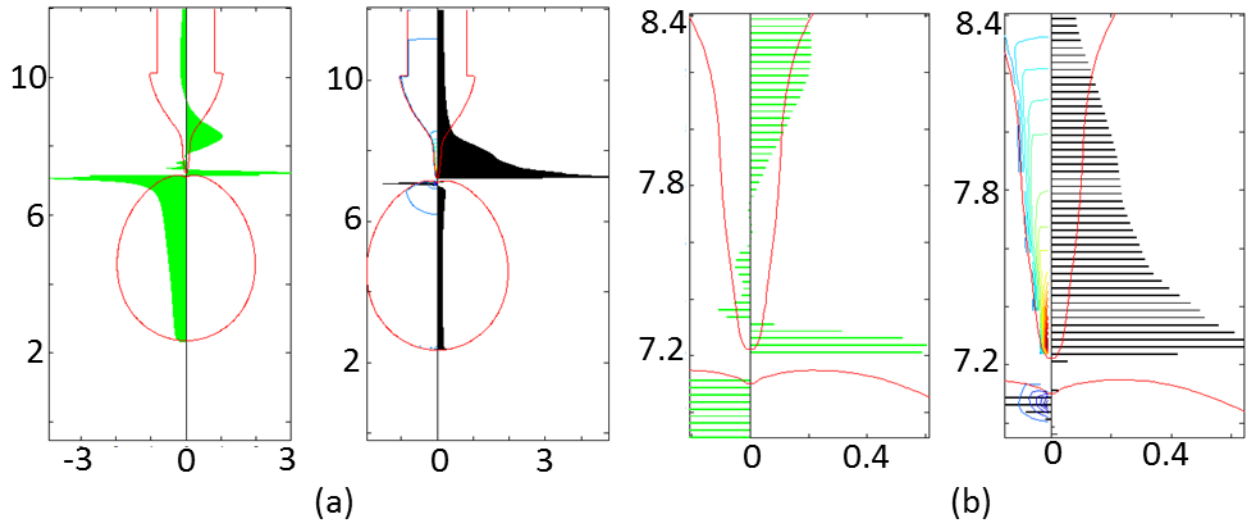

Figure 3-6 Primary bifurcation at t=435.04ms: LEFT, axial velocity and RIGHT, pressure distribution along the center axis of the liquid column. a) without magnification b) magnified view of the filament.

iii. Recoil

The pressure and velocity profiles immediately after the primary bifurcation are shown in Figure 3-6. The radius of the filament decreases monotonically from the cone-filament junction to the sharp edged tip. As a consequence, capillary pressure increases along the filament. At the tip of the filament the pressure gradient is very steep which generates a strong upward recoiling flow there. It has also been reported by Peregrine *et al.* [28] that the unbalanced surface tension force acts like an impact which causes a rapid acceleration of the liquid filament. The upward flow at the tip of the filament is referred to as the primary recoiling flow in this study.

As shown in Figure 3-6, there is a wavy shape axial velocity profile in-between primary and tertiary recoiling flow. This wavy shape also appears in the following time instants at t=435.12 and 435.2ms, but gradually vanishes.

Explanation of this phenomenon could be drawn from the history of the pendant drop formation. As explained earlier, the primary extending flow originated from the midsection of the filament instead of filament-sphere junction (Figure 3-4, t=434.96ms). After bifurcation of the liquid column at the filament-sphere junction, although there is no change in the shape of the liquid filament, the downward extending flow at the tip of the filament is replaced by the upward primary recoiling flow. The rest of the primary extending flow that is present in the filament between the midsection and the tip is subjected to a steep pressure gradient that pushes this downward flow in an upward direction. As a result the flow recoils upward creating small vortices. From 2-D velocity field in Figure 3-7 at t=435.04ms, it is found that the flow field is bending inward. At t=435.12ms, two small vortices are noticeable. However, these vortices are short lived and as the pressure gradient dominates, the vortices vanish and the flow field becomes upward at t=435.2ms. This flow field is referred to as the secondary recoiling flow in this study.

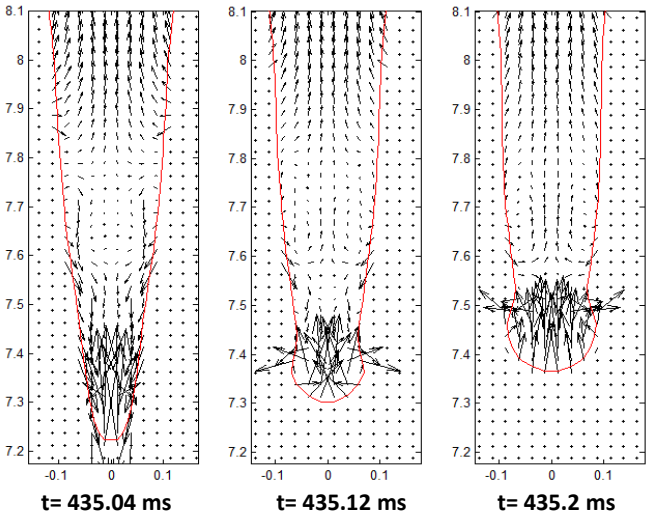

Figure 3-7 Velocity vectors along the filament right after the primary bifurcation.

As shown in Figure 3-8 at t=435.2 and 435.44ms, the primary recoiling flow at the tip of the liquid filament creates a bulb shaped tip which is referred to as the primary bulb. Since the fluid is accumulated at the bulbous tip of the filament, the neck of the primary bulb becomes concave and due to negative lateral curvature, pressure decreases. Thus a small pressure fluctuation is created in an otherwise monotonously upward decreasing pressure field. Although the magnitude of this fluctuation is small initially, it is amplified in the following time instants as the neck of primary bulb becomes more noticeable (at t=435.44 and 435.60ms). As the pressure gradient at the neck of the bulbous tip gets steeper, it squeezes the fluid downward from the neck region. This downward flow at the neck of the bulbous tip is referred to as the secondary extending flow in this study. The development of secondary extending flow can be realized comparing the axial velocity profiles at t=435.44, 435.60 and 435.68ms in Figure 3-8.

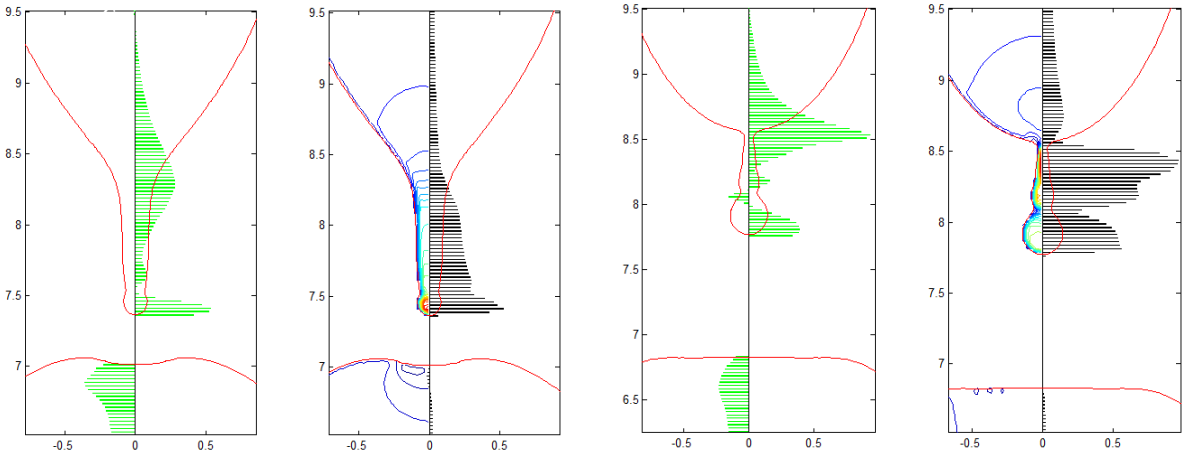

t=435.20ms t=435.68ms

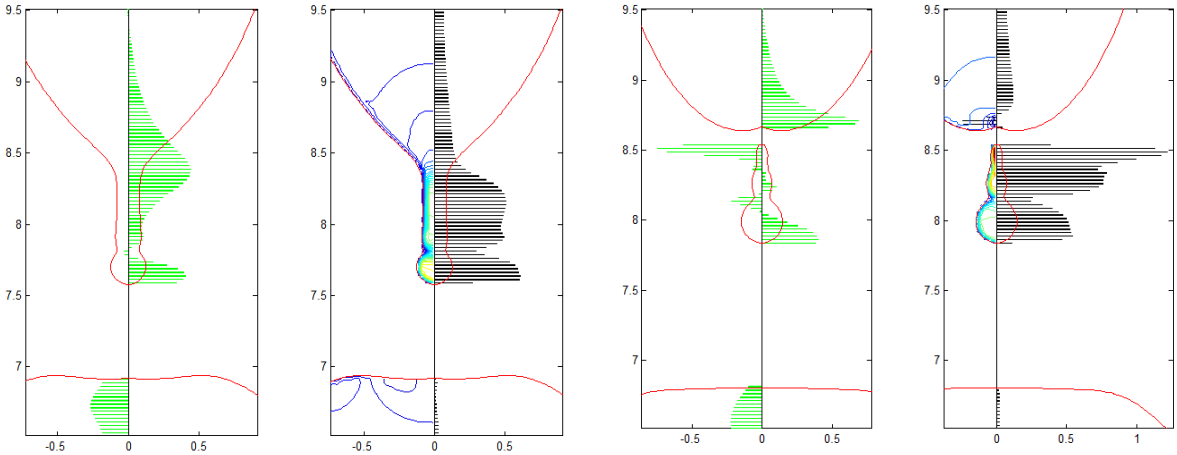

t=435.44ms t=435.76ms

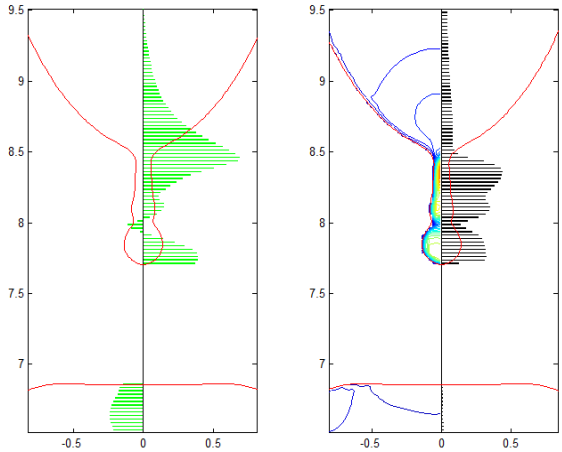

t=435.60ms

Figure 3-8 Filament recoiling and secondary bifurcation (magnified view): LEFT, the axial velocity, RIGHT, pressure distribution along the center axis of the liquid column

iv. Wave Generation

The secondary recoiling flow above the neck of the primary bulb is less perceptible at t=435.2ms in Figure 8. However, due to the favorable pressure gradient in this region, this flow field gets stronger and becomes more noticeable at t=435.60 and 435.68ms. As a consequence, fluid is accumulated immediately above the neck of the primary bulb and a second bulging shape is created. The formation of the secondary bulb becomes noticeable at t=435.68ms in Figure 3-8. Thus alternating extending and recoiling flows create small ripples on the liquid filament. Such ripples can also be found in the experiment conducted by Peregrine *et al* [28]. The shape of the free surface is also reflected on the pressure profile. The trough of the each ripple has local minimum pressure due to negative lateral curvature while the local maximum pressure can be seen at the crest of the respective ripple.

v. Secondary Necking and Bifurcation

In between t=435.04 and 435.68ms the shape of the filament changes from a sharp edged tapered one to a rounded edge bottom heavy one as can be seen from Figure 6 and 8. The corresponding pressure profile also changes accordingly. The sharp tip of the filament had the highest pressure at the beginning of this period, but at t=435.68ms the bulbous tip of the filament has the third highest pressure peak while the highest pressure can be found at the thin cone-filament junction from Figure 3-8.

As discussed earlier, tertiary recoiling flow is due to the pressure gradient at the cone-filament junction. During recoiling process, this flow field contributes to the thinning of filament at the cone-filament junction. As a result liquid column is bifurcated again and a satellite droplet is formed at t=435.76ms in Figure 3-8.

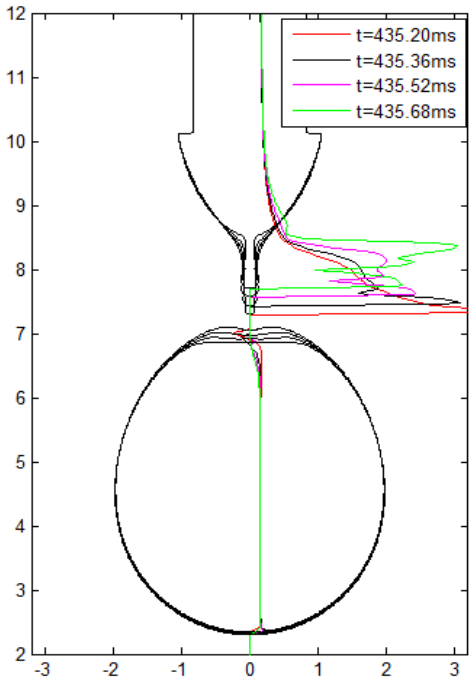

Figure 3-9 Consecutive pressure profiles along the center axis of the liquid column.

Two aspects of tertiary recoiling flow play an important role for successful secondary bifurcation. First, tertiary recoiling flow has a bell shaped profile with its peak at the cone-filament junction that gradually decreases on either sides. Such a profile is the consequence of an elongated filament and associated pressure distribution at the instant of primary bifurcation. Because of the bell shaped tertiary recoiling flow which is observed during the entire recoiling period, fluid is squeezed upward from the cone-filament junction without getting compensated enough by the trailing recoiling flow. Thus the junction gets thinner over time.

Second, tertiary recoiling flow demonstrates strong acceleration. Shown in Figure 3-9, as the cone-filament junction gets thinner with time, the capillary pressure increases. Eventually the junction becomes concave and associated negative lateral curvature of the interface results in a steep pressure gradient. As a result, tertiary recoiling flow has strong

acceleration as shown in Figure 3-10a that enables thinning of cone-filament junction at a faster rate. Thus the primary and secondary recoiling flow do not have enough time to recoil the filament and join the liquid cone, before the liquid column breaks at the cone-filament junction (Figure 3-8, t=435.76ms).

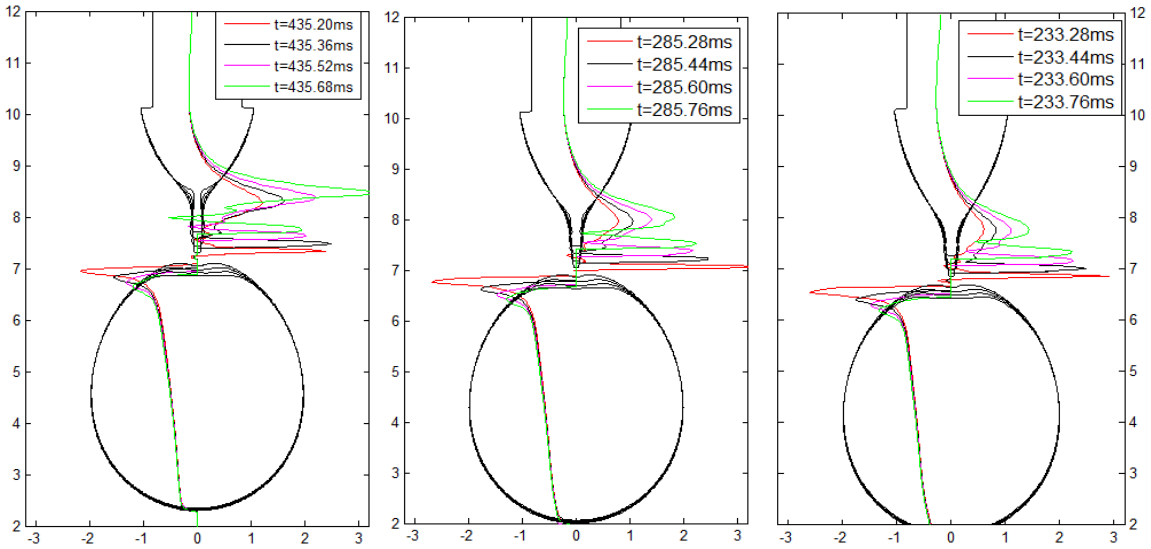

(a) (b) (c)

Figure 3-10 Consecutive axial velocity distributions during filament recoiling; a) 0.05m/s, b) 0.08m/s and c) 0.1m/s inlet velocity.

Effect of Flow Rate

In order to study the effect of flow rate on the formation of a satellite droplet, the inlet velocity has been increased from 0.05m/s to 0.08m/s and 0.1m/s, holding all other parameters the same. As the flow rate increases, the primary bifurcation takes place earlier and the length of the liquid column prior to the primary bifurcation is longer as shown in Figure 3-11. Although the dynamics of primary bifurcation is almost same as before, at increased flow rate the liquid cone contains more fluid. The elongated cone shrinks

gradually and smoothly transforms into a filament. However, the filament itself is thicker, less elongated and more tapered in shape than its low flow rate counterpart.

The shapes of cone-filament junction and filament at the instant of primary bifurcation affect the pressure and velocity fields. For 0.1m/s inlet velocity, first, distribution of axial velocity at the cone-filament junction is no longer bell shaped due to shorter filament (Figure 3-12, 233.60 ms). Instead, the magnitude of this flow decreases sharply at the neck of bulbous tip. Such a velocity field does not shrink the cone-filament junction instead, it retracts the junction upward.

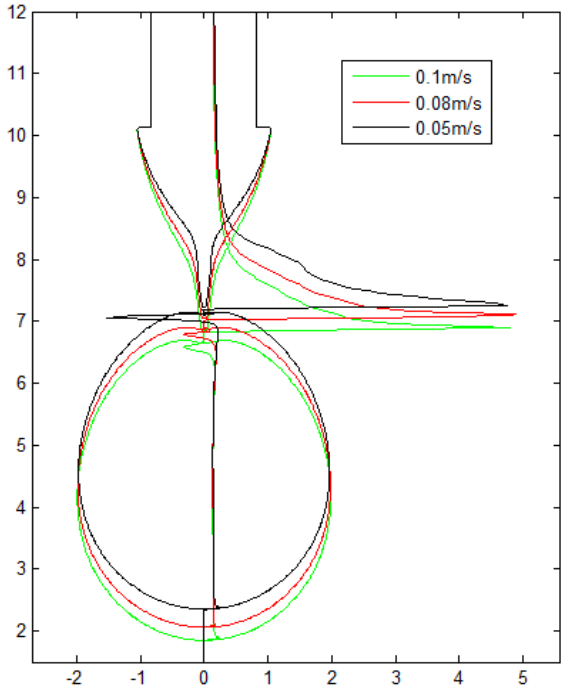

Figure 3-11 Pressure distribution at the instant of primary bifurcation for various inlet velocities.

Second, smoothly shaped cone-filament junction results in less steep pressure gradient (Figure 3-11) and a weaker acceleration of tertiary recoiling flow (Figure 3-10).

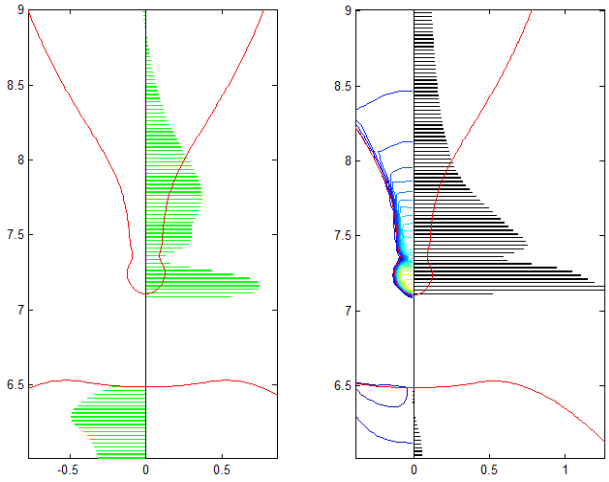

t=233.60 ms

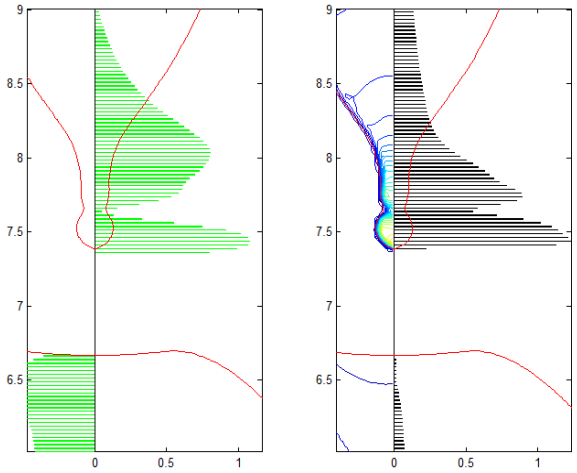

t=285.68 ms

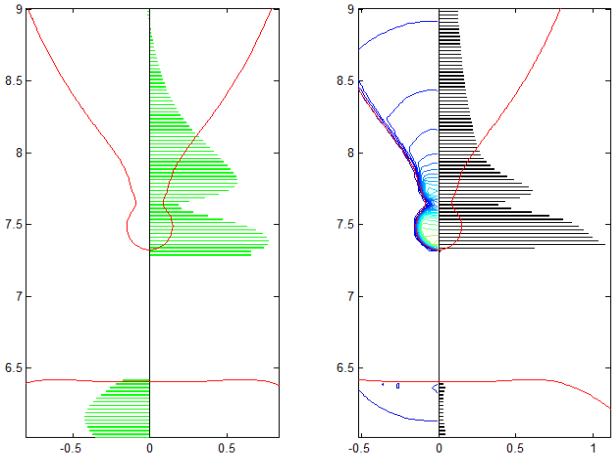

t=233.84 ms

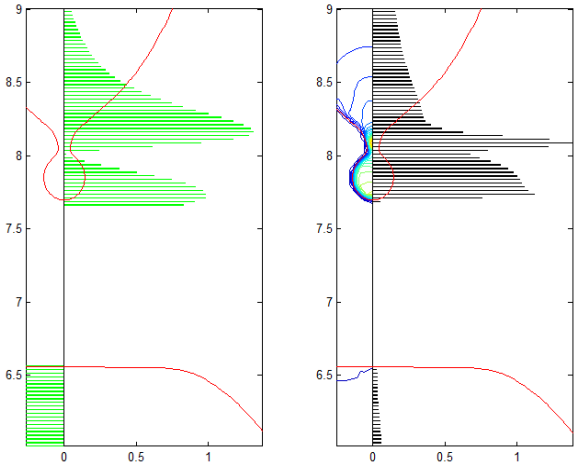

t=286.00 ms

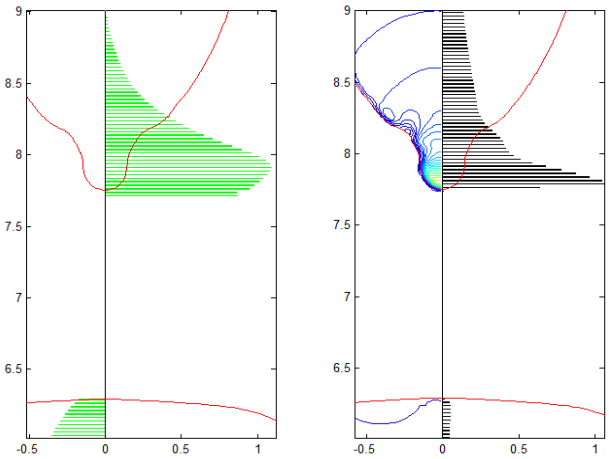

t=234.24 ms

Figure 3-12 Filament recoiling at 0.1m/s inlet velocity; LEFT: axial velocity, RIGHT: pressure distribution along the center axis of the liquid column.

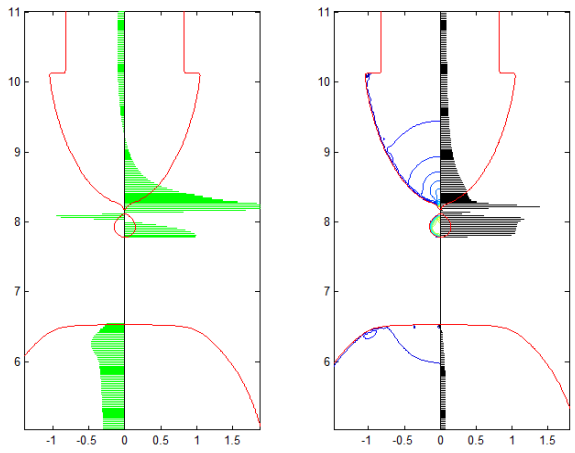

t=286.08 ms

Figure 3-13 Filament recoiling at 0.0.08m/s inlet velocity; LEFT: axial velocity, RIGHT: pressure distribution along the center axis of the liquid column.

Consequently, the cone-filament junction retracts at a rate slower than the primary bulb (Figure 3-12, 233.84ms). Thus, the primary bulb joins the liquid cone at 234.24ms producing no satellite droplet.

Recoiling of filament at 0.08m/s inlet velocity is similar to that at 0.1m/s inlet velocity, except retraction of cone-filament junction is faster (Figure 3-10 and 3-13) due to the slightly steeper pressure gradient at this location (Figure 3-11). As a result, the liquid column is bifurcated at the neck of bulbous tip as the primary bulb falls behind due to relatively slower recoiling speed (Figure 3-13, t=286 ms).

Effect of Surface Tension

In order to study the effect of surface tension on the dynamics of satellite droplet formation, surface tension coefficient has been increased by 50% for the 0.1m/s inlet velocity holding all other parameters the same. As the surface tension coefficient increases, the length of the liquid column increases and the primary droplet grows larger in size as shown in Figure 3-14. Although the mechanism of primary bifurcation is the same as before, the overall time required for primary bifurcation increases. This is because increased capillary force can sustain the gravity induced straining for a longer period of time and at the same time, it can maintain a larger pendant droplet.

Dynamics of filament recoiling before and after increasing surface tension co-efficient is similar except the cone-filament junction is slightly sharper as shown in Figure 3-14. Consequently, the pressure gradient at this location is steeper that develops a faster acceleration of tertiary recoiling flow (Figure 3-15). The recoiling of liquid filament and subsequent generation of the satellite droplet at increased surface tension coefficient is shown in Figure 16 where rapid acceleration of the tertiary recoiling flow enables swift

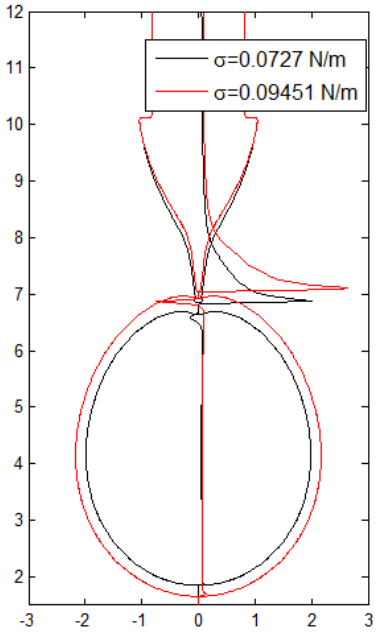

Figure 3-14 Pressure distribution at the instant of primary bifurcation for various different surface tension coefficients.

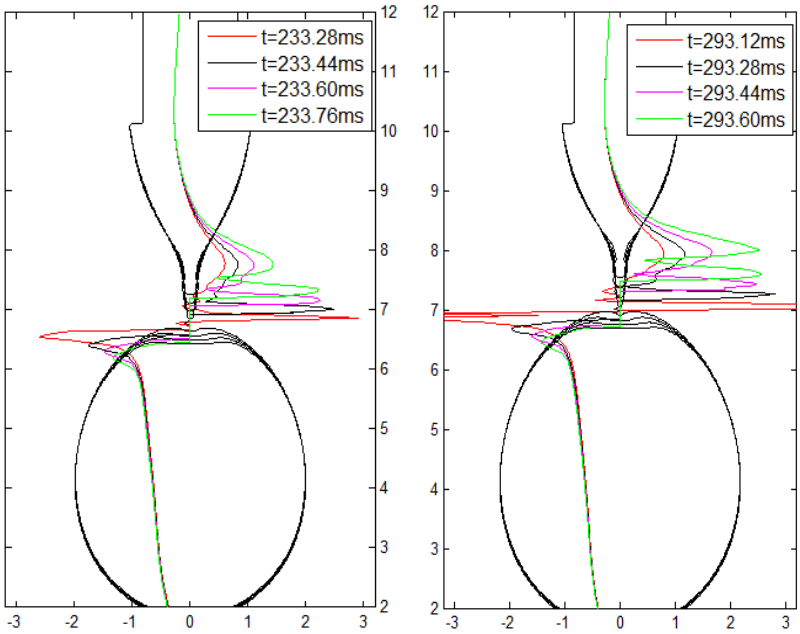

Figure 3-15 Consecutive axial velocity distributions during filament recoiling; a) σ=0.0727N/m, b) σ=0.09451N/m.

recoiling of the cone-filament junction. Consequently, the filament breaks before the bulbous tip could reach the liquid cone and thus a satellite droplet is formed (Figure 3-16, 293.92ms). Note that before increasing the surface tension coefficient, no satellite droplet was observed.

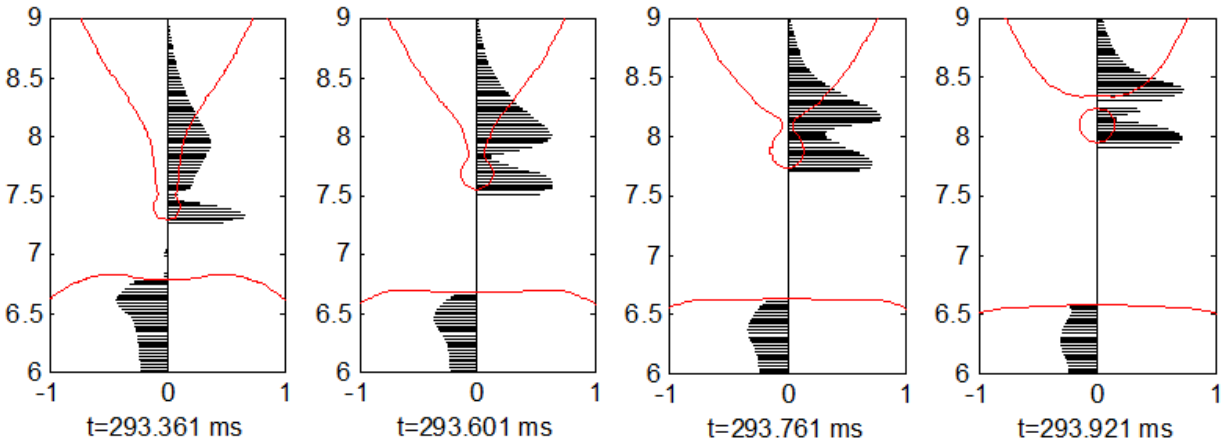

Figure 3-16 Axial velocity distributions during filament recoiling at u=0.1m/s, σ=0.09451N/m and μ=1.005e-3N.s/m2

Effect of Viscosity

In order to study the effect of viscosity on the formation of the satellite droplet, the dynamic viscosity has been increased about 28 times for the 0.05m/s inlet velocity holding all other parameters the same. The dynamics of primary bifurcation is almost same as before increasing viscosity. However, the cone-filament junction is sharper and filament is more elongated at the instant of primary bifurcation as shown in Figure 3-17.

Various stages of filament recoiling and subsequent satellite droplet formation have been shown in Figure 3-18. As the viscosity dampens the motion, no discernible ripples are formed on the elongated filament except for a bulbous tip. Consequently, pressure is almost uniform inside the liquid cone and along the liquid filament with a steep

rise at the cone-filament junction (t=462.64ms). Such a profile forms a bell shaped axial velocity distribution at the cone-filament junction that eventually shrinks the junction and a satellite droplet is formed as shown in Figure 3-18, 463.12ms.

The interesting feature for this case is that in spite of the steeper pressure gradient at the instant of primary bifurcation (Figure 3-17), comparing Figure 3-19a and 3-19b it is found that the acceleration of tertiary recoiling flow is weaker in case of increased viscosity. Although satellite droplet has been confirmed both before and after increasing viscosity, there are differences in the shape of satellite droplet. Capillary waves were more prominent on the satellite droplet before increasing viscosity, but after increasing viscosity fewer ripples were observed on the satellite droplet.

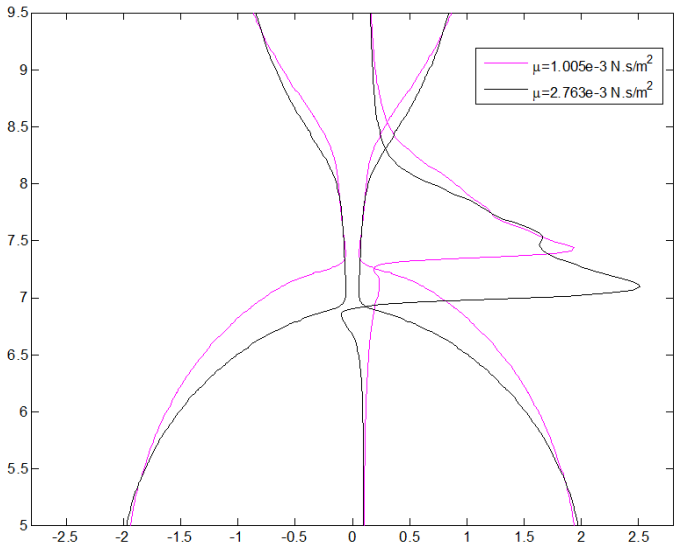

Figure 3-17 Axial pressure distributions at the instant of primary bifurcation for different viscosities.

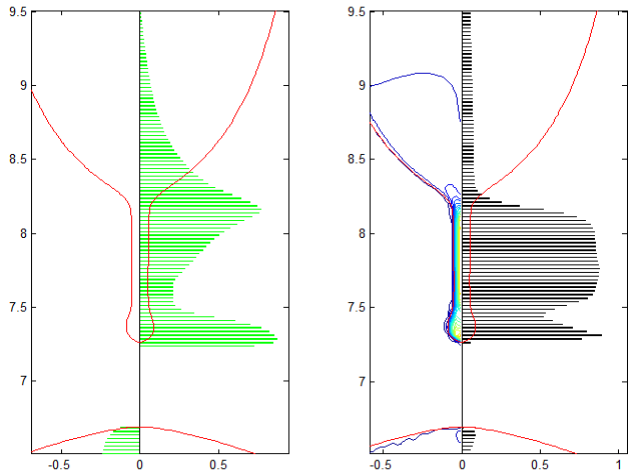

t=462.64ms

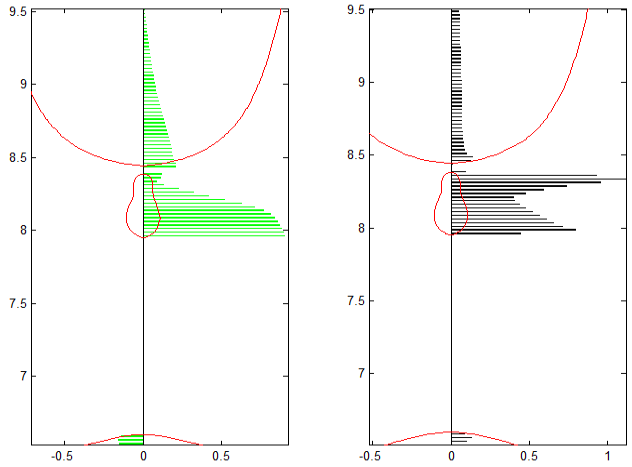

t=462.96ms

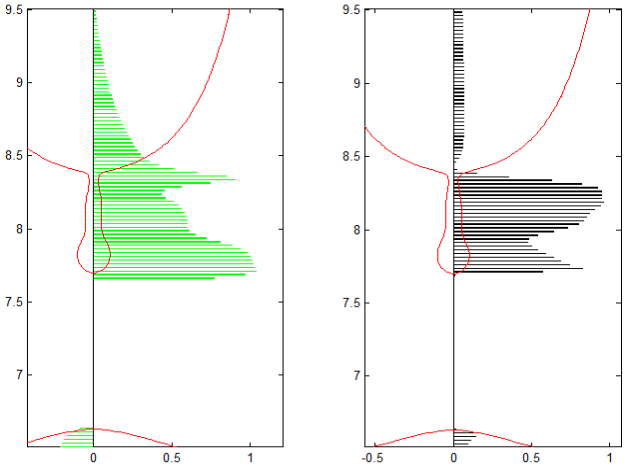

t=463.12ms

Figure 3-18 Filament recoiling at u=0.05m/s and μ=2.763e-3 N.s/m^2; LEFT, axial velocity, RIGHT, pressure distribution along the axis of the liquid column.

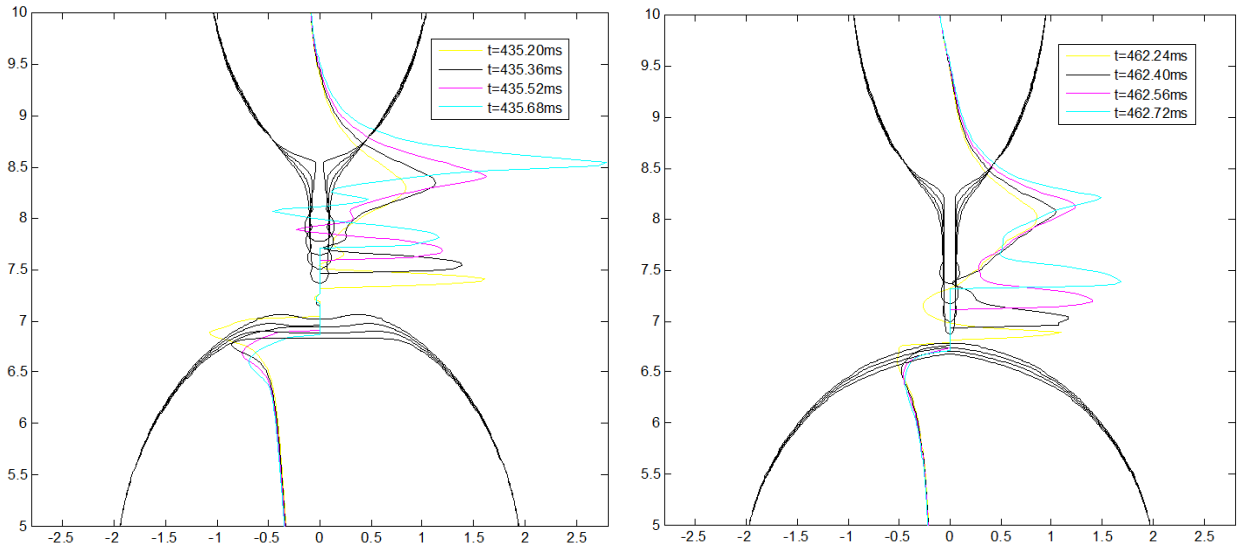

Figure 3-19 Consecutive axial velocity distributions at 0.05m/s inlet velocity;

a) μ=1.005e-3 N.s/m^2 , b) μ=2.763e-2 N.s/m^2.

Closure

Dynamics of droplet formation from a vertical tube under the action of gravity for a Newtonian incompressible fluid has been studied numerically using a CLSVOF method for tracking the free surface in conjunction with the CSF model for the surface tension calculation. The various stages of pendant droplet formation have been examined in detail and some interesting features of the filament recoiling process have been studied. The controlling factors of subsequent satellite droplet formation have also been identified. The probability of satellite droplet generation depends on the fast acceleration and the bell shaped distribution of the axial velocity at the cone-filament junction. The inlet velocity and surface tension play a dominant role in satellite droplet formation. Satellite droplet is less likely to be formed at high inlet velocity and low surface tension coefficient. Viscosity, on the other hand, has been found to play an important role on the shape of liquid filament and satellite droplet.

Chapter 4

Electrowetting Induced Droplet Detachment from Hydrophobic Surface

Introduction

Recoiling and stretching of a sessile droplet involve the transformation of surface energy into kinetic energy and vice versa. Using external force such as electric field or mechanical vibration the droplet can be stretched where it can store large amount of surface energy. As the droplet recoils, the stored surface energy transforms into kinetic energy that enables the droplet to restore its shape at a lower surface energy level. The difference of these two surface energy levels that at first transforms into kinetic energy, develops droplet oscillation and if the difference is large enough it can detach the droplet from the solid substrate. Researchers have utilized similar phenomenon in various microfluidics applications [43-45]. By converting the surface energy into kinetic energy as the micro droplets coalesce spontaneously, they can be detached from the hydrophobic condensing solid surface that eventually enhances the phase-change heat transfer process [43]. Electrowetting-induced droplet oscillations have also been used for efficient micro-fluidic mixing [44]. During this process, the droplet is repeatedly stretched and recoiled by applying an AC voltage. Vertical transportation of a droplet from the bottom to the upper surface is another example in three dimensional digital microfluidics that uses the conversion of surface energy to kinetic energy of a sessile droplet through electrowetting-on-dielelectrode [45].

In the process of electrowetting induced droplet detachment, an electric potential is applied between the solid substrate and the droplet as it rests on top of a hydrophobic

surface. This leads to reduction of effective solid-liquid surface tension and decreases the apparent contact angle at the three phase contact line. Consequently, the droplet spreads on the substrate and the electrical energy is converted into the surface energy. When the voltage is turned off, the stored surface energy is converted into kinetic energy as the droplet recoils. Depending on the extent of droplet stretching, it may just oscillate and eventually come to rest after dissipation of the kinetic energy or may induce sufficient vertical elongation for droplet detachment.

During the recoiling of a stretched droplet, a fraction of stored surface energy is lost through excitation of surface waves and flow induced dissipation according to the study by Cavalli *et al.*[46] in which the efficiency of surface to kinetic energy conversion in the droplet detachment process have been investigated both numerically and experimentally. The effect of applied voltage on the energy balance of the jump as well as the role of finite wettability on the threshold radius for detachment have also been quantified.

Detachment of droplets from a hydrophobic surface by applying a square voltage pulse has been analyzed by Lee *et al.* [47]. Threshold voltage for droplet detachment for volumes ranging from 0.4 to 10 μL has been investigated both experimentally and theoretically. The possibility of droplet detachment for different voltage pulse widths has also been analyzed.

In the present numerical study, emphasis has been given to the dynamics of stretching and recoiling of the droplet. As discussed earlier, not the entire amount of available surface energy is transformed into the kinetic energy that detaches the droplet. A fraction of the surface energy is consumed to overcome adhesion between the solid substrate and the droplet, another fraction of the surface energy is spent to recoil the

droplet towards its center with the formation of capillary waves. The remaining surface energy that transforms into kinetic energy will elongate the droplet and increase the gravitational potential energy by elevating the center of mass of the droplet. In order to obtain a comprehensive picture of the entire process, it is necessary to understand the underlying dynamics of stretching and recoiling that accompany the formation of surface waves. This is done by analyzing the pressure and velocity field inside the droplet. The numerical results have been compared with experimental data [47] available in the literature for validation. A parametric study has been performed which includes volume of the droplet, voltage amplitude and voltage pulse width.

Computational Setup

An experimental study of detachment of a sessile droplet from a hydrophobic surface subjected to a square pulse voltage was conducted by Lee *et al.* [47]. In their study, an aqueous 1mM NaCl droplet was placed on top of a spin-coated Teflon surface as shown in Figure 4-1. A dielectric layer of 5.0μm thickness was placed in between the hydrophobic Teflon layer and the bottom electrodes. The bottom electrodes were connected to a needle electrode at the top, which is partially immersed into the droplet. A square voltage pulse was applied between the needle and the bottom electrode which changes the apparent wettability of the hydrophobic Teflon surface. The static contact angle of the droplet was reported to be 116˚±3˚ and the advancing and receding contact angles were 119˚±3˚ and 110±3˚, respectively.

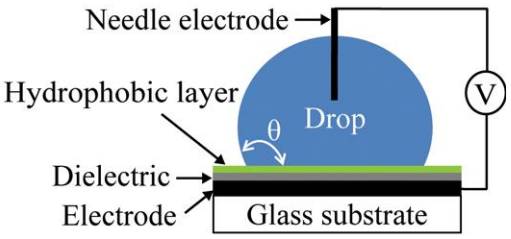

Figure 4-1 Schematic of experimental setup for electrowetting induced droplet detachment [47].

In the present numerical simulation using VOF-CSF scheme, a droplet of a specified volume is initialized as a hemisphere on top of a solid substrate which is the bottom boundary of the two-dimensional rectangular axisymmetric computational domain. A rigid no-slip wall boundary condition with 116° static contact angle (same as water/Teflon system) is imposed at this boundary. The computational domain is large enough to ensure that the droplet is contained throughout the detachment process. The droplet is given sufficient time to reach an equilibrium shape conforming to the specified contact angle. A square voltage pulse is then applied between the substrate and droplet which is implemented numerically by reducing the static contact angle at the bottom surface for a time duration equal to the voltage pulse width. The reduced contact angle is obtained from the Young-Lippmann's equation given by:

$$cos\theta = cos\theta_0 + \frac{\epsilon_0 \epsilon}{2\sigma_{lg} t} V^2 \tag{4-1}$$

where θ_0 is the equilibrium contact angle with zero electric potential, ϵ the dielectric constant, ϵ_0 the permittivity of the vacuum, t the thickness of the dielectric layer, σ_{lg} the liquid-vapor surface tension, V the electric potential and θ the reduced contact angle. The Young-Lippmann equation is reasonably accurate in predicting the contact

angle at low voltage. However, it has been discovered that the contact angle θ remains constant beyond a threshold voltage. This effect is referred to as contact angle saturation and has been addressed in the literature [48-49].

As the droplet spreads and recoils during this process, contact angle hysteresis has an overall effect of reducing the stretching and recoiling speed and its physics is still not completely understood. The fact that dynamic contact angles are influenced not only by the plate material [50] but also by other factors such as temperature, ambient pressure, droplet properties, surface irregularity and smoothness makes prediction of dynamic contact angles very challenging. The following scheme is used to determine whether the interface is advancing or receding at each time step before the dynamic contact angles are applied

$$\vec{\boldsymbol{n}}.\vec{\boldsymbol{u}}\begin{cases} < 0 & advancing\ interface \\ > 0 & receding\ interface \end{cases} \tag{4-2}$$

Once the direction is determined, the dynamic contact angles are computed by the following equations:

$$\theta_R = \theta - \Delta_R \tag{4-3}$$

$$\theta_A = \theta + \Delta_A \tag{4-4}$$

where Δ_R and Δ_A are the deflections of the receding and advancing contact angles from the static contact angle, respectively. In the present study, Δ_R and Δ_A have been assumed to be 6˚ and 3˚, respectively, following the experiment by Lee *et al.* [47].

Results and Discussion

As the modeling of contact angle carries great importance for this numerical study, successful implementation of static contact angle is demonstrated in Figure 4-2. In this validation test, a 5μL hemispherical droplet is initially placed on a substrate of various wettability. The final steady shapes of the droplet for the various contact angles prescribed at the substrate are shown. The blue line represents the angle that was prescribed in the wall boundary condition of the code and the red line represents the equilibrium shape of the droplet. The blue line can be seen to be tangential to the interface at the three phase contact line, thus demonstrates the accuracy of the method employed.

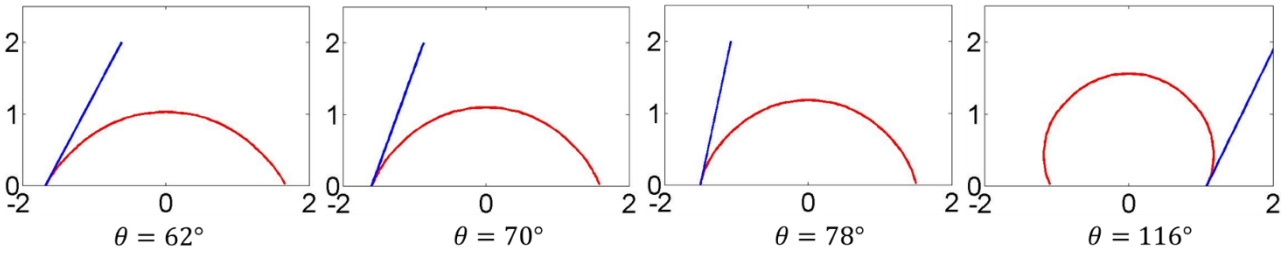

Figure 4-2 Numerical modeling of various static contact angles.

The numerical results of the present study have been compared with experimental results reported in [47]. In order to compare various stages of droplet detachment, 116˚/73˚ change in contact angle which corresponds to 135V square pulse in the experiment, is applied to a 5μL droplet for 7ms. All other parameters such as fluid and dielectric properties are as in the experiment. A uniform square mesh with grid spacing of 0.05mm is used which is based on the result of a grid refinement study presented in the Appendix. The time step for the numerical calculations is automatically adjusted during the course of calculation, which is taken as the minimal of the time step constraints for the numerical stability of capillarity, viscosity and the Courant condition [26].

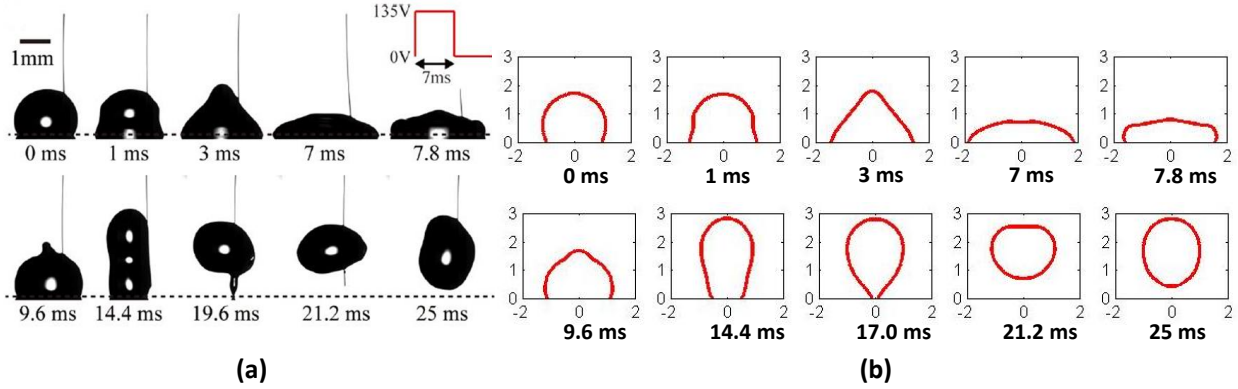

Figure 4-3 Various stages of droplet detachment (a) experimental [47] (b) present numerical study.

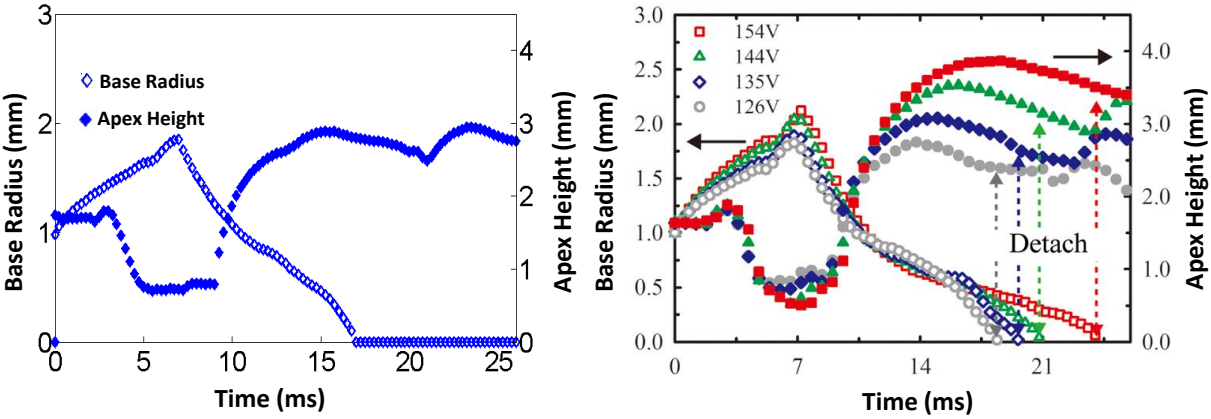

Figure 4-4 Base radius and apex height versus time during a 5μL droplet detachment; Numerical simulation at 135V (left); experimental results [5] (right).

The various stages of the droplet detachment process are shown in Figure 4-3. The time variation of base radius and apex height are shown in Figure 4-4. There is an excellent agreement in shape and size of the droplet between numerical and experimental studies up till 9.6ms. At 14.4ms, the droplet apex reaches the highest point in both studies. The maximum apex height in numerical simulation is 4.6% lower than the experimentally observed value. This discrepancy might due to uncertainty in hysteresis angle used in numerical study. Note that the hysteresis angle is obtained from the experiment in which

3˚ uncertainty has been reported [47]. Droplet detachment time is 19.6 ms for the experiment whereas it is found to be 17.0 ms in the numerical simulation. In the experiment a thin filament connecting the droplet to the solid substrate can be observed at the instant of detachment, whereas no such shape is found in the numerical results. Such a liquid filament is also absent in similar numerical and experimental studies conducted by Cavalli *et al.* [46]. Perhaps formation of the filament delayed the detachment in the experiment. It should be noted that in the experimental study, droplet has an asymmetric shape as it lifts off from the substrate which was not addressed by the authors [47]. This could be due to the presence of the needle electrode in the experimental setup. In spite of these discrepancies, the overall agreement in droplet deformation between numerical and experimental studies is good. For a more thorough analysis on the evolution of droplet detachment, it is divided into three stages: stretching, recoiling and detachment which are discussed in detail below.

Droplet Stretching

It has been reported that electrowetting induced contact angle reduction causes a droplet to spread with the formation of capillary waves along its surface [47]. In the present study two stages of capillary wave have been observed during stretching. In the first stage, the capillary wave is generated from the droplet base which propagates upward and eventually converges at the top edge of the droplet. In the second stage, a surface wave is generated at the top-mid section that induces droplet oscillation. A reduced contact angle remains active during this process until the droplet reaches its maximum diameter.

The dynamics of droplet stretching are presented in Figure 4-5. After the hemispherical droplet is stabilized, it makes an obtuse contact angle (~116˚) with the

hydrophobic substrate as shown in Figure 4-5 at t=0ms. Due to the decrease in apparent contact angle, the droplet base begins to spread as shown at t=1ms. Sudden expansion of the base creates a disturbance that propagates upward in the form of a capillary wave along the droplet surface. In this capillary driven flow, the static pressure inside the droplet is a function of the droplet topology i.e. the radial and lateral curvatures. As the droplet base expands, the radial curvature around the base decreases resulting in a pressure difference between the upper and lower part of the droplet. Again due to the capillary wave,

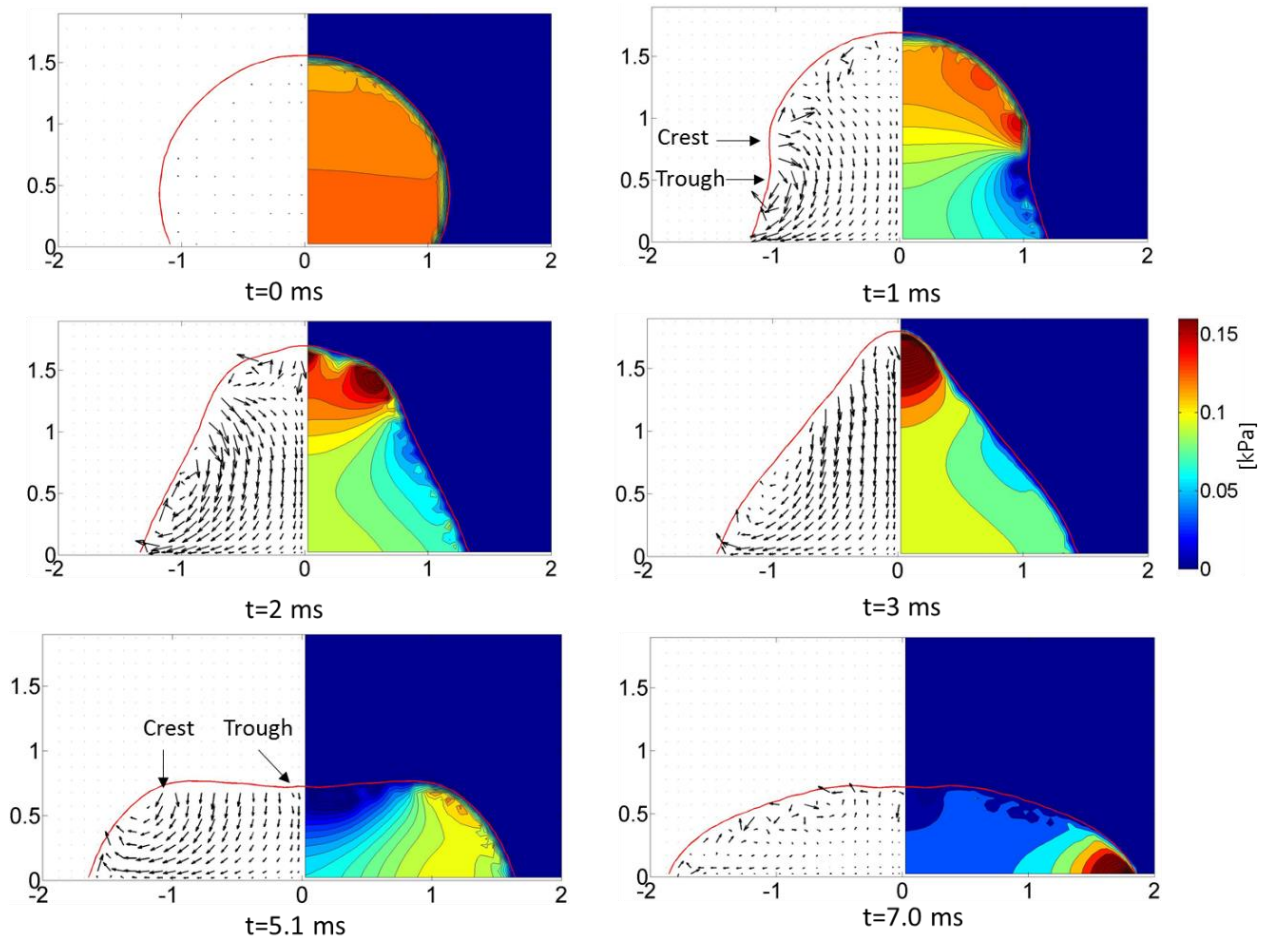

Figure 4-5 Pressure and velocity fields during droplet stretching.

there is a low pressure zone at the trough and a high pressure zone around the crest of the wave. Thus the lateral curvature also contributes to the pressure field which directly affects the flow field inside the droplet. As can be seen at t=1ms, the overall fluid motion is downward and it spreads outward at the bottom. Again there is a circular fluid motion that originates from around the crest of the capillary wave and drives the fluid inward and downward.

In between 1.0 and 3.0ms, the capillary wave propagates upward while the droplet base spreads further. At t=3.0ms, the wave converges at the top edge forming a triangular droplet which has also been recorded in the experiment [47] (Figure 4-3). It should be noted from Figure 4-4 that the droplet apex does not drop during the first stage of wave propagation (until 3ms), although its base is stretched continuously. In fact, the apex is higher than that of the initial droplet at t=3.0ms. This is due to the fact that while the capillary waves are propagating upward, the peripheral circular motion drives the fluid towards the center of the droplet while its base expands.

There is a large curvature at the tip of the triangular shaped droplet. Consequently, the static pressure near the triangular peak is also high which results in a strong downward current from the tip of the triangle and the height of the droplet reduces sharply in between 3.0 and 5.0ms as shown in Figure 4-4. Eventually as this process continues, the top-mid section becomes a low pressure concave trough, surrounded by an outer high pressure crest (t=5.1ms, Figure 4-5). Due to the inertia of the downward-spreading flow, the pressure gradient at the crest cannot oppose but only hinders the spreading and only for a very short period of time. Indeed, it can be seen in Figure 4-4 that the slope of radius versus time is almost flat at t=5.1ms for both numerical and experimental results [47]. As the droplet continues to spread outward its center oscillates until ultimately reaching its maximum

diameter at t=7.0ms. The voltage is then turned off and the apparent contact angle changes from wetting to non-wetting. At that moment, the droplet has attained its maximum surface energy and is on the verge of recoiling inward, converting the surface energy back to kinetic energy.

Droplet Recoiling

Droplet recoiling is shown in Figure 4-6. At t=7.2ms, due to the sudden increase in apparent contact angle, the sharp edges become rounded and convex. The large curvature at the edge of the droplet creates a high pressure which leads to a strong recoiling flow accompanied by a capillary wave. As the capillary wave propagates inward, the base radius decreases as shown at t=7.85ms. Note that at this time instant the top-mid portion of the droplet has a slight positive lateral curvature but it is much less than the curvature at the crest of the capillary wave. Consequently, the resulting pressure gradient recoils the droplet.

At t=8.55ms, the existence of a strong recoiling flow can be seen clearly. The capillary wave has propagated further inward and creates an apparently flat interface at the top-mid section of the droplet. The static pressure around this flat surface is lower than the pressure at the crest of the capillary wave. Consequently, the pressure difference that drives the recoiling flow intensifies. At t=9.05ms, just before the wave converges, a low pressure trough surrounded by the high pressure crest is created. This concave trough has a large negative lateral curvature, resulting in a pressure gradient which initiates a strong upward flow at the top-mid section of the droplet. The strong upward flow along the center axis of the droplet is more pronounced at t=9.6ms. Eventually, the trough disappears and a small bulb shaped tip can be seen instead.

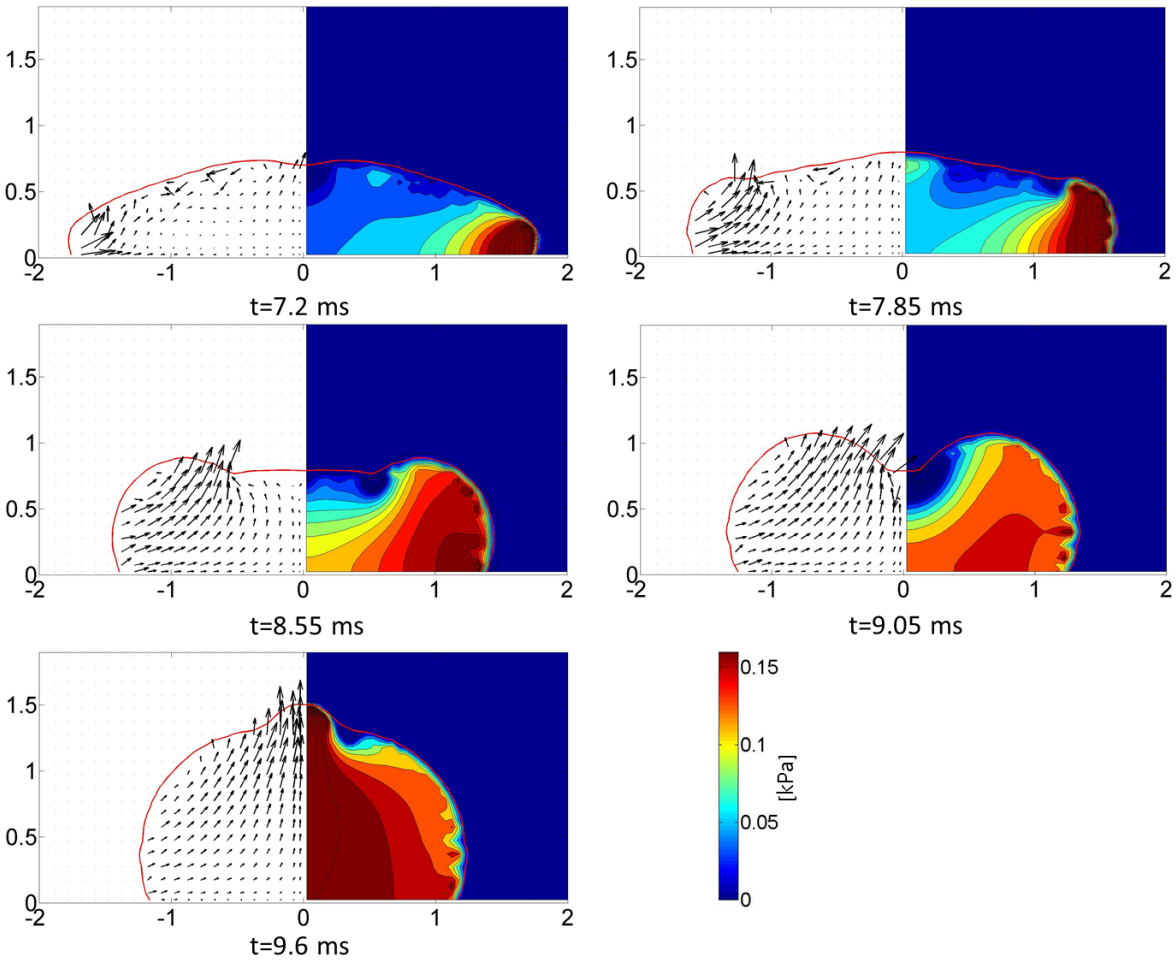

Figure 4-6 Pressure and velocity fields during droplet recoiling.

Droplet Detachment

In between t=7.0 and 9.6ms, the droplet transforms from a maximum wetted shape into a shape that matches closely with the initial droplet shape at t=0ms. As the total surface area is reduced during this transformation, the excess surface energy is transformed into kinetic energy which elongates the droplet vertically and eventually leads to the detachment of the droplet from the substrate, as shown in Fig. 4-7.

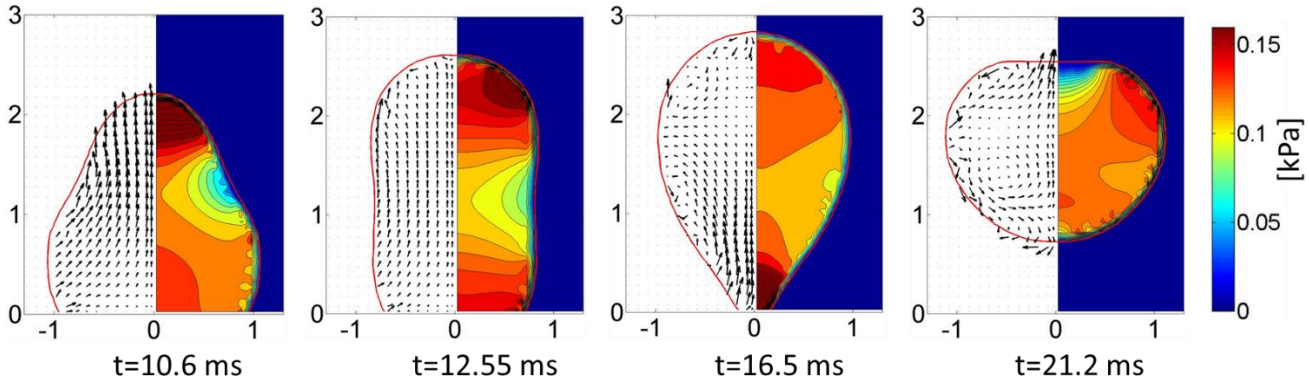

Figure 4-7 Pressure and velocity fields during droplet detachment.

At t=10.6ms, the droplet elongates due to the upward flow that starts at t=9.6ms. As the radial curvature at the upper part of the droplet is higher than that at the center, there is a pressure difference between the top and mid-section of the elongated droplet. Thus a restoring force is created that tries to hold the droplet in spherical shape. But this pressure gradient is not sufficient to suppress the strong upward elongating flow field. As the droplet elongation continues, the base radius decreases continuously. At t=12.55ms, the shape of the droplet becomes cylindrical with almost uniform radial curvature. At t=16.5ms, the base radius is less than the radius at the center of the droplet. As a result, the radial curvature at the base becomes higher than the radial curvature at the center of the droplet and the corresponding pressure gradient pushes the droplet away from the substrate. Eventually the capillary force overcomes the gravitational force and lifts the droplet from the substrate.

Droplet Spreading Spectrum

In order to ensure droplet detachment, it is necessary to have adequate droplet stretching that generates sufficient kinetic energy. For a given fluid and surface properties, the spreading diameter of a sessile droplet depends on various factors, such as voltage

pulse width, amplitude of the pulse and droplet volume. After the droplet is stabilized on the hydrophobic (~116˚) substrate, the contact angle is reduced permanently to a wetting angle (<90˚) at t=0ms which simulates the activation of the electrode. The droplet then goes through a sequential spreading and recoiling process without detachment. However, as the droplet is allowed to oscillate freely, the magnitude of this oscillation dampens with time and finally the droplet is stabilized again at the wetting contact angle with the substrate. For the sake of discussion, from here onward, the base radius versus time plot for such an oscillating droplet will be referred to as the droplet spreading spectrum.

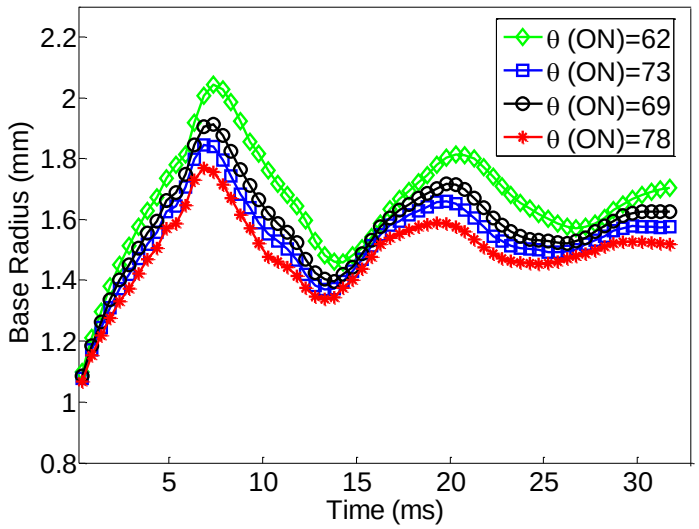

Figure 4-8 Droplet spreading spectrums for a 5μL droplet for various actuating contact angles.

Spreading spectrums for a 5μL droplet on top of a hydrophobic surface (~116˚) for various actuating contact angles are shown in Figure 4-8. Note that the actuating contact angles are tied to the rms voltages in the experiment via the Young-Lippmann's equation. Higher voltage yields lower actuating contact angle and larger stretching diameter hence it should take longer stretching time. But the driving force that stretches the droplet is also

stronger for higher voltage resulting only slight increase in maximum stretching time. As shown in Figure 4-8, the differences among maximum stretching times at various actuating contact angles are small and the maximum stretching time has been assumed to be 7ms for a 5µL droplet throughout this study.

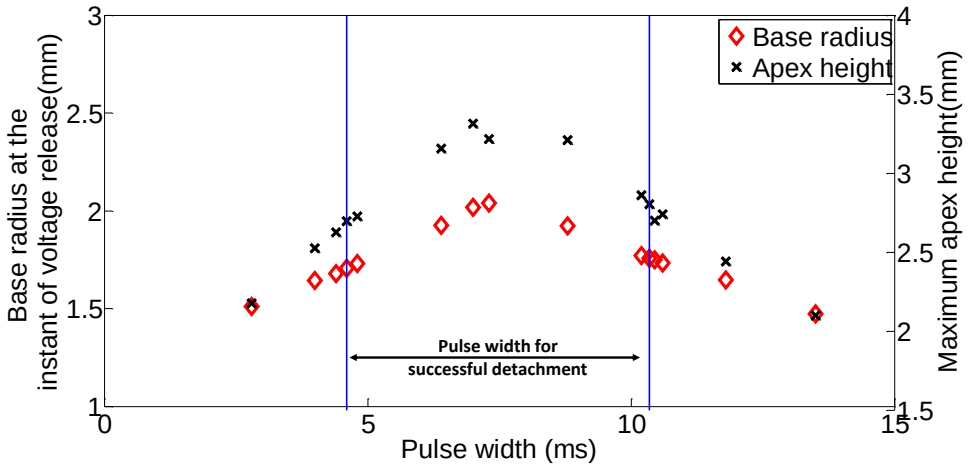

Figure 4-9 Base radius at the instant of voltage release and maximum apex height versuspulse width (5µL droplet with 116˚/62˚ change in contact angle).

By adjusting the voltage pulse width one can control the spreading of the droplet at the instant of voltage release which in turn determines the probability of detachment and maximum jumping height. Base radius at the instant of voltage release and maximum apex height for various pulse widths are shown in Figure 4-9. Note that by connecting the base radii in this figure, one can obtain the droplet spreading spectrum for given specifications. As shown in the figure, pulse width determines the stretching of the droplet at the instant of voltage release and consequently the fate of droplet detachment and maximum apex height. There is an upper and lower limits of the pulse width within which the droplet detaches. The base radii corresponding to these limits are almost identical which suggests that the droplet has harnessed equal amount of surface energy at the instant of voltage

release in both cases. The maximum apex height also varies with the pulse width. For the pulse width corresponding to larger spreading, the maximum apex height is also higher.

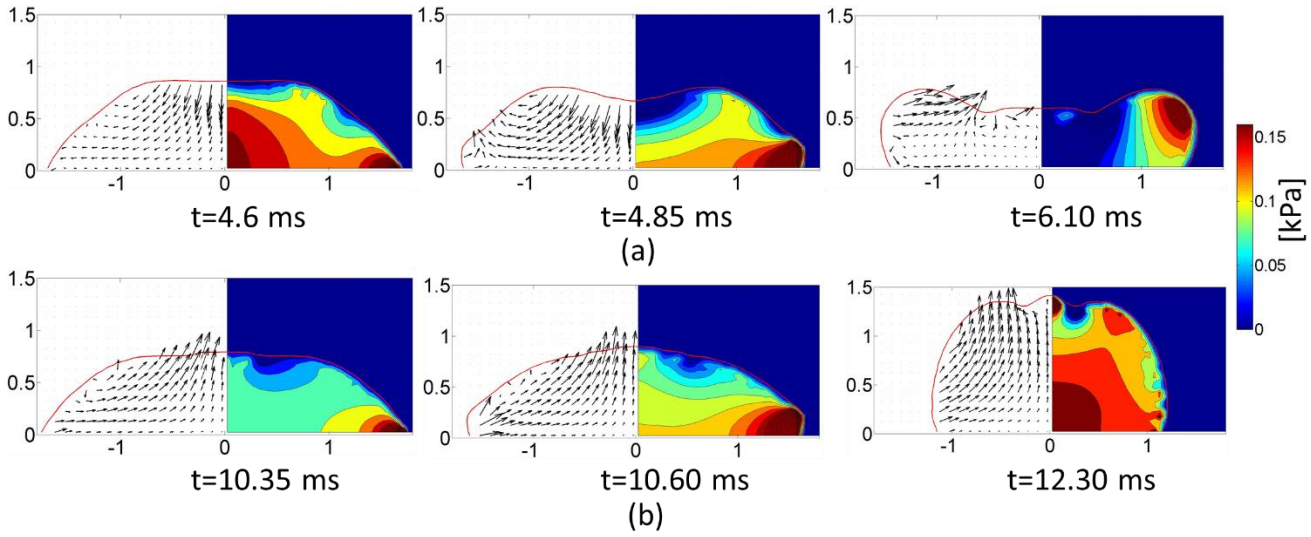

Figure 4-10 Pressure and velocity fields during droplet recoiling;
(a) 4.6ms pulse width (lower limit); (b) 10.35ms pulse width (upper limit).

The dynamics of droplet recoiling at the upper and lower pulse width limits are shown in Figure 4-10. Although the base diameters and the shapes of the stretched droplets at the upper and lower limits are similar right before the voltage release (compare t=4.6ms and t=10.35ms in Figure 4-10(a) and (b), respectively), the physics of recoiling differs. For the 4.6ms pulse width (lower limit), the droplet was still spreading when the voltage was turned off. As a result, a downward-spreading flow field can be observed inside the droplet. Due to the downward flow, the top-mid section of the droplet becomes concave (t=4.85ms in Figure 4-10(a)). The concave shape creates a lower pressure zone and together with the higher pressure zone at the edge of the droplet, develops a large pressure gradient. The pressure gradient hinders further spreading of the droplet and reduces the strength of the outward flow field. By t=6.10ms, the flow field becomes inward. Thus it took

almost 1.5ms for the pressure gradient to convert a downward-spreading flow into an inward-recoiling flow field. As the recoiling continues, capillary wave converges and the droplet eventually detaches itself from the hydrophobic surface due to the high kinetic energy as previously described.

As for the 10.35ms pulse width (upper limit), the flow field inside the droplet is already recoiling (Figure 4-10(b)) which is a favorable condition for detachment. Due to the upward elongating flow field, the top mid-section of the droplet becomes convex at t=10.60ms. The lateral curvature of this convex shaped top-mid section is lower than the curvature at the edge of the droplet. So, there is a pressure gradient between the top-mid section and the edge of the droplet which assists the droplet to recoil. Even though this pressure gradient is less intense than the 4.6ms pulse width where the top-mid section of the droplet was concave, it still helps the fluid to recoil and ultimately detaches itself from the substrate.

As shown in Fig. 4-11, the 10.35ms pulse width has higher overall elevation while the 4.60ms pulse width has larger spreading. These results can be understood from the difference in initial flow fields. Furthermore, the recoiling and subsequent detachment of the droplet occur sooner for the 10.35ms pulse width. As mentioned previously, for the 4.6ms pulse width case, the pressure gradient has to convert a downward spreading flow into an upward recoiling flow in order to detach the droplet from the solid substrate. Whereas the pressure gradient just assists the already existing recoiling flow to detach the droplet in the case of the 10.35ms pulse width.

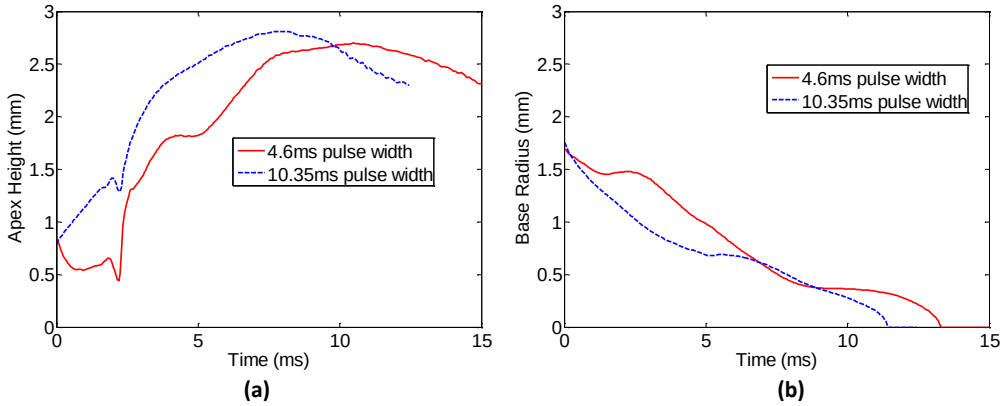

Figure 4-11 Apex height and base radius versus time for the 116˚/62˚ change in contact angle. (Starting time shifted to the instant of voltage release).

The spreading spectrums for various droplet volumes with 116˚/73˚ change in contact angle are plotted in Figure 4-12. The base radius, R, of the droplet has been nondimentionalized by R_c, the radius of a spherical droplet of the same volume and time, t has been nondimentionalized by T_s, the time required to stretch the droplet to its maximum diameter for the corresponding droplet volume. T_s at different droplet volumes are: 2.36ms (0.575 µL), 5.25ms (3.0 µL), 6.7ms (5.0 µL), 8.0ms (7.5 µL) and 17.5ms (39.41 µL). These values are comparable to experimental values reported in [47] at: 2ms (0.4 µL), 3ms (1 µL), 5.3ms (3 µL), 7ms (5µL), and 9ms (10µL). As can be seen from Fig. 12, the frequencies of the normalized spreading spectrum for different droplet volume are almost same. As for the 0.575, 5 and 7.5µL droplets, the normalized spreading diameters are almost same. But as the volume increases further, the spreading also increases. This phenomenon can be explained with the use of the Bond number ($Bo = \frac{\Delta\rho g R_c^2}{\sigma}$), which is the ratio of gravitational and capillary forces. As the Bond number is much less than unity, the gravitational force does not affect the spreading of the droplet as much but as the Bond number approaches

to unity, due to the increased effect of the gravitational force, spreading of the droplet increases.

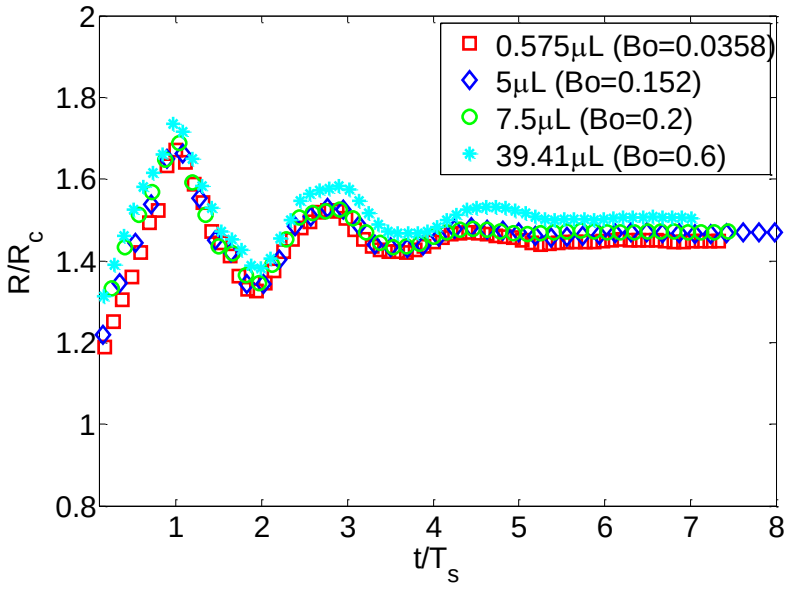

Figure 4-12 Normalized spreading spectrum for different droplet volume.

Effect of Actuating Contact Angle

The droplet detachment process at various actuating contact angles are shown in Figure 4-13. A 5μL droplet on top of an 116˚ hydrophobic surface is studied where the droplet is stretched to its maximum diameter when the voltage is released. As mentioned previously, the time required for the maximum stretching has been assumed to be 7ms based on the previous analysis of a 5μL droplet. Droplet detachment occurs for all of the actuating contact angles. As expected, higher voltage yields larger droplet stretching (Figure 4-13(b)) thereby enables it to store larger amount of surface energy which produces larger droplet elongation (Figure 4-13(a)).

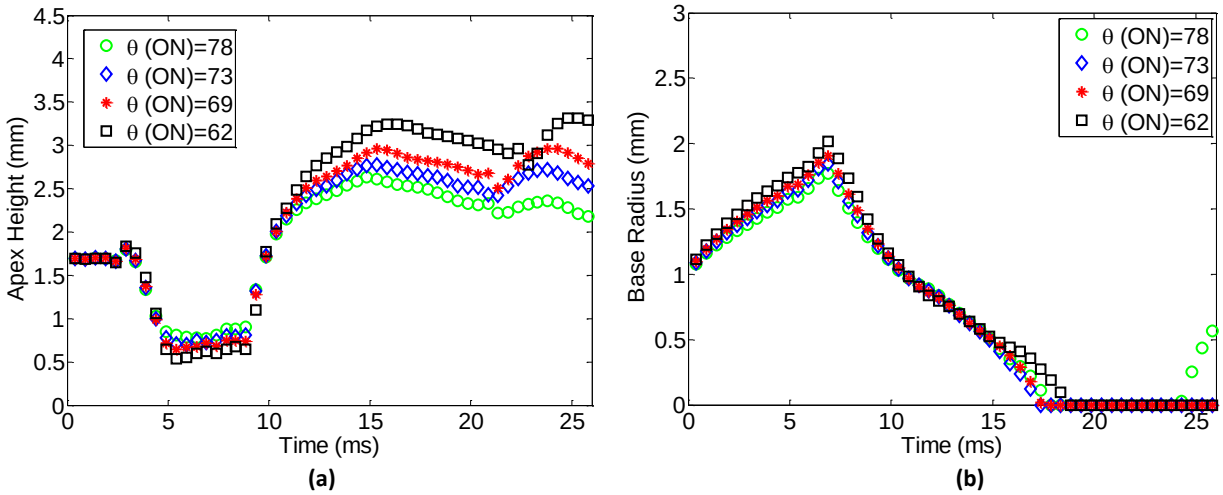

Figure 4-13 Effect of actuating contact angle on the droplet detachment process for a 5µL droplet.

Effect of Droplet Volume

The effect of droplet volume on droplet elongation is shown in Figure 4-14. Again, the droplet has been stretched to its maximum diameter when the voltage is released. It should be noted that droplet detachment from the substrate occurs in all of the cases except for the 39.41µL case. The normalized elongation is higher for smaller droplet volume where the Bond number is also lower. As the Bond number increases, the effect of gravitational force on the droplet also increases and the elongation of the droplet decreases.

Considering the overall effect of droplet volume and voltage magnitude, it is possible to find the minimum voltage required for detachment for a given droplet volume. The threshold voltages versus droplet volumes are plotted in Figure 4-15. In order to compare the numerical results with the available experimental data [47] the threshold

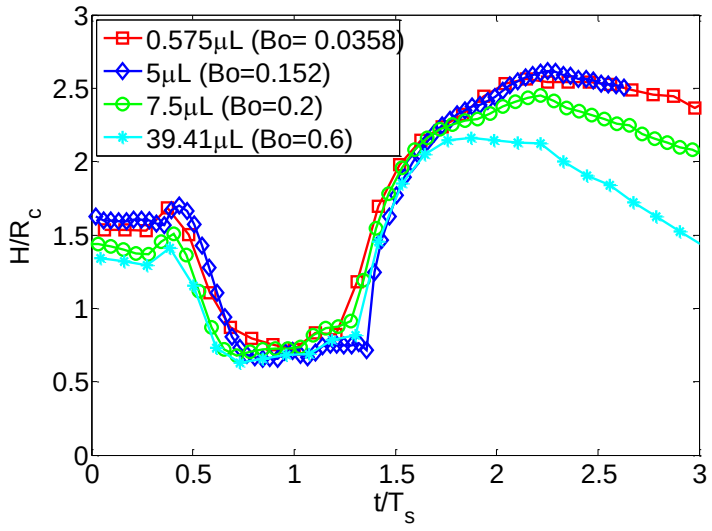

Figure 4-14 Apex height versus time for various droplet volumes

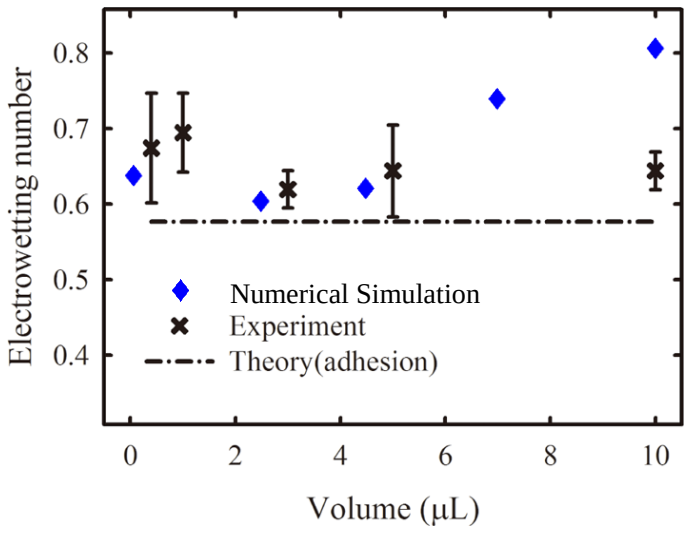

Figure 4-15 Threshold voltage for droplet detachment for various droplet volumes.

voltage is expressed in terms of the Electrowetting number, η, given by $\epsilon\epsilon_0 V^2/2t\sigma_{lg}$ (see Eq. 4-1). As shown in Figure 4-15, the numerically obtained threshold Electrowetting numbers for all of the cases, are higher than the theoretical minimum Electrowetting

number for detachment of 0.57 [47] which was obtained by balancing the electrical energy imparted by the applied voltage and the adhesion work. The threshold voltage for droplet detachment is not entirely independent of the volume. For very small droplet volume, the threshold Electrowetting number is around the theoretical minimum value of 0.57. For the larger volumes, threshold voltage for the detachment increases which indicates that gravity and viscous effects are important which were neglected in theoretical prediction.

Closure

Dynamics of electrowetting induced droplet detachment from a hydrophobic surface has been analyzed numerically using the VOF-PLIC method for tracking the free surface in conjunction with the CSF model for the surface tension. The various stages of droplet detachment which include stretching, recoiling and detachment have been examined in detail. The effect of voltage pulse width, amplitude of voltage pulse and droplet volume on the detachment process have also been investigated. It has been found that an optimization of voltage pulse width is required to ensure sufficient stretching and subsequent detachment of the droplet. Higher voltage leads to lower actuating contact angle which enhances the possibility of droplet detachment and increases the vertical elongation of the droplet. The Bond number has been found to play an important role when the effect of droplet volume is considered. For Bond numbers much less than unity, droplet detachment does not depend on the voltage amplitude. Otherwise, higher voltage is required for detachment.

Chapter 5

Electrowetting Induced Droplet Transport in Parallel-plate and Open-plate Configuration

Introduction

Electrowetting induced droplet actuation has wide engineering applications [51] such as digital microfluidics [49,52], fibre optics [53], electronic cooling [54-55], enhancement of phase change heat transfer [56], adjustable lenses [57], fuel cells [58] and electronic displays[59]. When a conductive liquid droplet placed on a conductive solid is subjected to an electric potential, a thin layer of counter-ions called electric double layer is accumulated at the solid-liquid interface. The electrostatic force associated with the double layer pulls the droplet radially outward resulting a decrease in the apparent contact angle at the three-phase contact line [51]. The associated change in the curvature of the liquid-gas interface reduces the capillary pressure near the three-phase contact line; a phenomena that causes the droplet to spread out. In order to prevent electrolysis in the liquid at high actuation voltage, a dielectric layer of very small thickness is added in between the conductive solid and liquid. In addition, to minimize the static friction that resists the movement of contact line, a thin hydrophobic layer such as Teflon or Cytop is spin-coated on top of the dielectric layer. Such a combination of conductive solid (electrodes) and dielectric layer including hydrophobic coating to manipulate the droplet is referenced to as the electrowetting-on-dielectrode (EWOD) in the literature.

The remarkable advantage of EWOD is that it can control the fluid flow and even the shape of the droplet by changing the applied voltage alone [51]. Another salient feature is re-configurability; the droplet can be manipulated in different paths merely by controlling

the sequence of electrode actuation. The various droplet manipulation operations include horizontal and vertical transport, splitting, merging, dispensing and spreading. In general, EWOD devices can be categorized depending on the placement of the reference and activated electrode. In early days, the droplet was actuated using a ground electrode at the bottom and a needle electrode that is partly submerged into the droplet from the top. Using such an arrangement it was only possible to spread out the droplet. In recent times such an arrangement has been used even in vertical droplet transport [45,47]. The most popular EWOD devices use parallel-plate configurations where the bottom plate contains individually addressable control electrodes and the top plate contains the ground electrode. Parallel-plate EWOD devices allow droplet transportation, merging and splitting. However, it reduces the transport velocity as both top and bottom plates exert viscous drag on the droplet. There is another configuration of EWOD devices known as co-planar design where both actuating and ground electrodes are arranged at the bottom plate with no top plate. Such an arrangement considerably reduces the viscous drag force on the droplet which results in faster transportation.

As droplet manipulation in EWOD devices often takes place within the lengthscale of a few millimeters on an extremely fast timescale, it is very difficult to analyse the dynamics inside the droplet experimentally whereas the numerical methods offer a good alternative. Various researchers have analysed the dynamics of electrowetting in parallel-plate configuration numerically. Transportation, division and creation of droplets in parallel-plate EWOD have been studied numerically using commercial software CFD-ACE+ employing volume-of-fluid method by Jang *et al.* [60]. A good agreement between numerical and experimental results has been reported in that study. Two dimensional planar flow in parallel-plate EWOD using Hele-Shaw type equations has been modeled by Walker and Shapiro [61] where the interface was tracked using the level set method.

Contact angle hysteresis was modelled to match the shape and time-scale of the simulation with the experiment. That study was later extended by Walker *et al.* [62] where the contact line pinning effect was introduced. Three dimensional droplet transport in parallel-plate configuration using volume-of-fluid method has been studied by Dolatabadi *et al.* [63] where contact angle hysteresis was modelled at a voltage threshold below which the contact angle imbalance does not move the contact line. This study was also extended by Arzpeyma *et al.* [64] where the electric potential was derived by solving the Laplace Equation for the entire domain. The derived potential was used to calculate the contact angle in individual grid cells by employing the Young-Lippmann's equation. Recently, a coupled level set and volume-of-fluid method (CLSVOF) was used by Guan and Tong [65-66] to study two dimensional planar droplet manipulation in parallel-plate EWOD, where a simplified model for the viscous stresses exerted by the two plates at the solid-liquid interface was used.

Although a number of studies have been conducted to investigate the electrowetting induced droplet manipulation, a study that analyses the pressure and velocity profiles with three dimensional topological deformation of the droplet in parallel-plate and open-plate EWOD configuration is still lacking. These are accomplished numerically in the present study using a Coupled Level Set and Volume-of-Fluid (CLSVOF) method. The numerical results have been compared with the published experimental data. A parametric study for parallel-plate EWOD has been performed which includes voltage amplitude, channel gap and electrode length. Open-plate droplet transport has also been analysed by varying the voltage amplitude. Finally the average transport velocities for the two types of EWOD configurations have been compared.

Computational Setup

In the present numerical analysis of the droplet transport in parallel-plate configuration, a circular droplet is initially sandwiched between the hydrophobic top and bottom plates (Figure 5-1). The top electrode is one whole piece which remains grounded at all time while the two disjointed square-shaped electrodes at the bottom can be switched ON and OFF individually as needed. The top and bottom plates act like a rigid no-slip wall with an 117˚ static contact angle (same as Teflon) imposed as part of the wall boundary condition corresponding to zero electric potential. Initially the circular droplet is placed at the center of the deactivated electrode. The effect of applying an electric potential was incorporated by reducing the static contact angle on the activated electrode according to the Young-Lippmann's equation given by:

$$cos\theta = cos\theta_0 + \frac{\epsilon_0 \epsilon}{2\sigma_{lg} t} V^2 \tag{5-1}$$

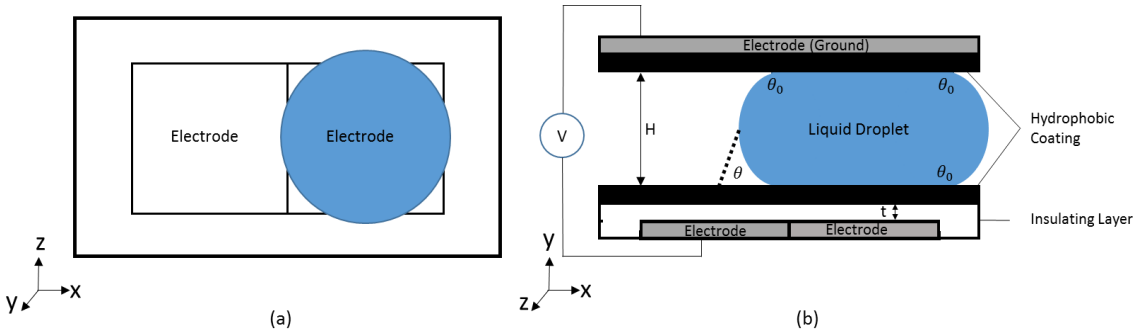

Figure 5-1 Schematic of droplet transport setup in parallel-plate configuration, (a) Top view; (b) Cross-sectional view. The reduced contact angle has been shown in broken line.

where θ_0 is the equilibrium contact angle with zero electric potential, ϵ the dielectric constant, ϵ_0 the permittivity of the vacuum, t the thickness of the dielectric layer, σ_{lg} the

liquid-vapor surface tension, V the electric potential and θ the reduced contact angle. The Young-Lippmann equation is reasonably accurate in predicting the contact angle at low voltage. However, it has been discovered that the contact angle θ remains constant beyond a threshold voltage. This effect is referred to as contact angle saturation and has been addressed in the literature [48-49].

As the droplet is deformed and pulled from the deactivated to the activated electrode, contact angle hysteresis occurs which has an overall effect of reducing the transport rate and its physics is still not completely understood. The fact that dynamic contact angles are influenced not only by the plate material [50] but also by other factors such as temperature, ambient pressure, droplet properties, surface irregularity and smoothness make prediction of dynamic contact angles very challenging. The following scheme is used to determine whether the interface is advancing or receding at each time step:

$$\vec{\boldsymbol{n}}.\vec{\boldsymbol{u}}\begin{cases} < 0 & advancing\ interface \\ > 0 & receding\ interface \end{cases} \tag{5-2}$$

Once the direction is determined, the dynamic contact angles are applied by the following equations:

$$\theta_R = \theta - \Delta_R \tag{5-3}$$

$$\theta_A = \theta + \Delta_A \tag{5-4}$$

where Δ_R and Δ_A are the deflections of the receding and advancing contact angles from the static contact angle. In the present study Δ_R and Δ_A have been assumed to be 4˚ following the observations by Lee *et al.* [47] and Nelson *et al.* [67].

Droplet transport in an open-plate configuration has been studied experimentally by Yi and Kim [68]. Here, the solid substrate contains both the driving and reference electrodes. In such a coplanar electrode configuration, the substrate is divided into multiple driving electrode units where each unit contains several sub-electrodes as shown in Figure 5-2. The solid substrate is spin-coated with hydrophobic layer of Cytop (~2000 A˚). By applying potentials among the sub-electrodes within a driving unit, the droplet is transported on top of it. In such a coplanar electrode arrangement a modified Young-Lippmann equation can be employed [68] where contact angle changes are related to the area ratio among driving electrodes, reference electrodes and the gaps in between.

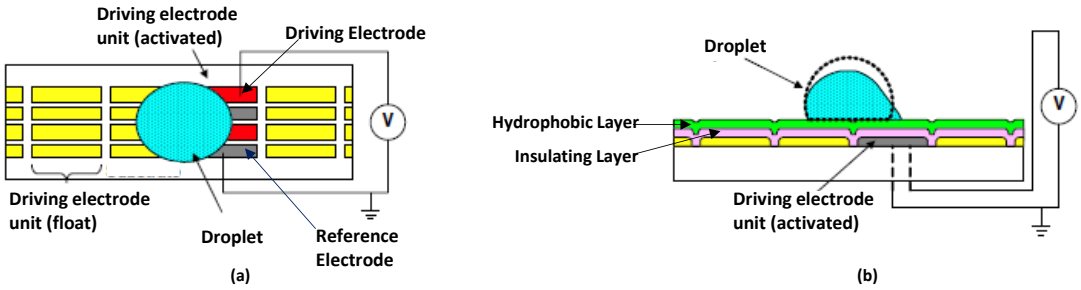

Figure 5-2 Schematic of droplet transport in open-plate configuration; (a) Top and (b) cross-sectional view of the experimental setups [68]

In the numerical modelling of open-plate transport, a droplet is placed on the hydrophobic solid substrate that contains two sets of driving electrode units. Initially the droplet is placed at the center of the deactivated electrode unit. The change in apparent contact angle on the driving electrode unit is obtained from the experimental data reported in [68] and implemented as part of the wall boundary condition.

Results and Discussion

Droplet Transport in Parallel-plate Configuration

In order to compare droplet transport in parallel plate configuration between numerical and experimental work [69], a 0.4μL water droplet was placed at the center of the OFF electrode while the other electrode was activated at 165V electric potential. The fluid and dielectric properties were as in the experiment. The length of the square electrode and the channel gap were 2.0mm and 0.1mm respectively in both studies. Application of the electric potential reduces the effective solid-liquid surface tension on the activated electrode. In response, the apparent static contact angle at the three phase contact line also decreases according to the Young-Lippmann's equation. A reduced apparent contact angle of 54˚ is implemented on the activated electrode. Everywhere else on the bottom plate and the entire top plate has a non-wetting angle of 117˚ which is the static contact angle of water on Teflon surface at zero electric potential. The mesh size is 0.025mm and 0.017mm in the parallel and normal directions to the plates, respectively based on a grid refinement study. The time step for the numerical computations is taken as the minimum of the time step constraints for numerical stability of capillarity, viscosity and the Courant condition [25-26]. As shown in Figure 5-3, the overall agreement between the experimental and numerical results is good. The observed difference could be due to the lack of exact reproducibility in the experimental procedure.

Pressure and velocity profiles inside the droplet during transport in a parallel-plate configuration are presented in Figure 5-4. The top and cross-sectional views with magnification of the leading and trailing edges of the droplet are presented. The droplet goes through both radial and lateral deformations during the transport process. The lateral

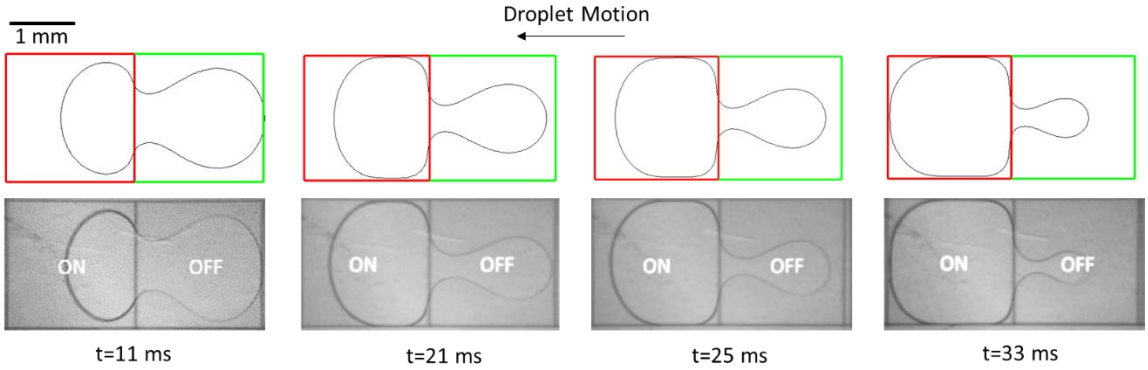

Figure 5-3 Comparison of droplet transport between numerical (top row) and experimental study [69] (bottom row).

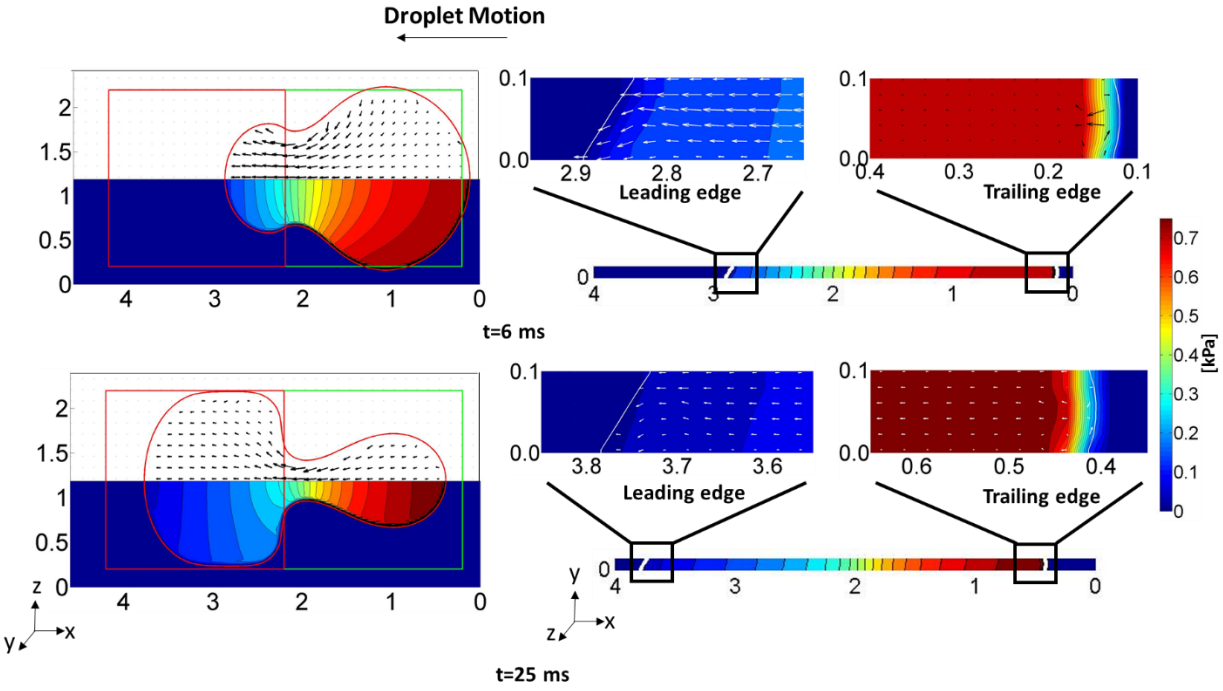

Figure 5-4 Droplet transport in parallel-plate electrowetting at 117˚/54˚ change in contact angle. Pressure and velocity fields are indicated by colormap and arrows, respectively. LEFT: Top view at y=50μm, RIGHT: Cross-sectional view at z=1mm.

deformation (observable in cross-sectional views) is caused by the difference in contact angle and the overall dynamics affect the radial deformation (observable in top view).

As the electric potential is applied, the part of the droplet on the actuated electrode quickly assumes a reduced contact angle as can be seen at t=6ms in Figure 5-4. From the cross-sectional view, the right end of the droplet makes an obtuse angle with both top and bottom plates whereas the left end of the droplet makes an acute contact angle with the bottom and an obtuse angle with the top plate. It should be noted that the free surface throughout the activated and deactivated electrodes has a topology similar to the magnified leading and trailing edges, respectively, shown in Figure 5-4. The lateral curvature on the activated electrode is lower than that at the deactivated electrode and this difference in curvature changes the pressure distribution inside the droplet creating a low pressure zone on the activated electrode and a high pressure zone on the deactivated electrode. The steep pressure gradient at the ON/OFF electrode junction pulls the droplet towards the activated electrode. On the other hand, the pressure gradient is lower in the large fluid body on the deactivated electrode thus producing only slight motion there. Consequently, a bulging shape develops at the leading edge of the droplet whereas the rest of it still remains circular.

According to Guan and Tong [65], the pressure difference between the activated and deactivated electrodes can be approximated by:

$$p_{OFF} - p_{ON} \cong \sigma_{LG} \left(\frac{\cos\theta - \cos\theta_0}{H} + k_{xz,OFF} - k_{xz,ON} \right) \tag{5-5}$$

where the first term within the parenthesis represents the difference in lateral curvature and the remaining terms represent the difference in radial curvature. At t=6ms, the radial

curvature on the activated electrode is larger than that on the deactivated electrode, resulting in a negative contribution in Eq. (5-5). However, the overall pressure difference remains positive because of the more substantial contribution of the lateral curvature due to the small channel gap (H). Thus the resulting pressure difference favors droplet transport in small channel gap.

It should be noted that the lateral deformations at the leading and trailing edges of the droplet remain almost identical throughout the transport process as can be seen from the cross-sectional views at various times. Thus the difference in lateral curvature continuously pushes the droplet from right to left. As this process continues, more and more fluid is transported to the actuated electrode and the bulging shape at the leading edge of the droplet expands as can be seen at t=25ms. At that point, the radial curvature at the trailing edge of the droplet is higher than that at the leading edge. As a result, the difference in radial curvature also assists the transportation as well as the lateral curvature. As shown in Figure 5-4, the overall pressure difference between t=6ms and 25ms increases with time. The droplet is fully transported to the actuated electrode by t=40ms.

It can be seen in Figure 5-4 that the pressure is uniform in the y-direction and the y-direction velocity component is negligible. Representative x-direction velocity profiles across the channel gap at various locations of the droplet are shown in Figure 5-5. It should be noted that although the flow is transient and not fully developed, the flow profiles appear parabolic in nature. Based on these observations the problem can be treated in 2D with a plane Couette flow model as was implemented by Guan and Tong [66]. For fully developed Couette flows between two stationary plates, the velocity profile is parabolic for both u and w, with the shear stresses at both planes equal to $6\mu(u/H)$ and $6\mu(w/H)$ in the x- and z-

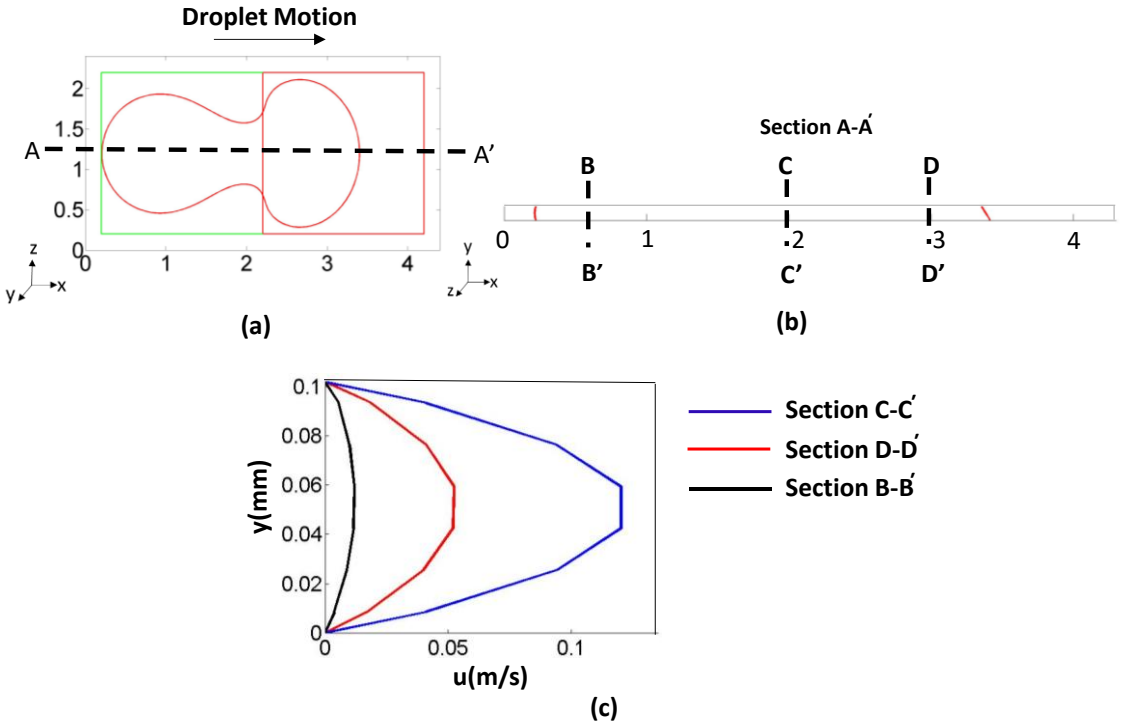

Figure 5-5 Droplet transport at t=15 ms, (a) Top view, (b) cross-sectional view and (c) velocity profiles across the channel gap at various locations.

directions, respectively. Since the flow is by no means steady and fully developed, the viscous stress from the Couette flow model is modified by a multiplication factor.

The effect of change in contact angle on the droplet transport is shown in Figure 5-6. Note that the change in contact angle are tied to the applied voltage in the experiment via the Young-Lippmann's equation. As expected, high electric potential reduces droplet transport time. Additionally, deformation of the droplet also depends on the applied voltage. Higher electric potential induces greater difference in lateral curvature between the activated and deactivated electrodes. The resulting steeper pressure gradient transports the droplet faster and creates more noticeable deformation. At the 117˚/54˚ change in

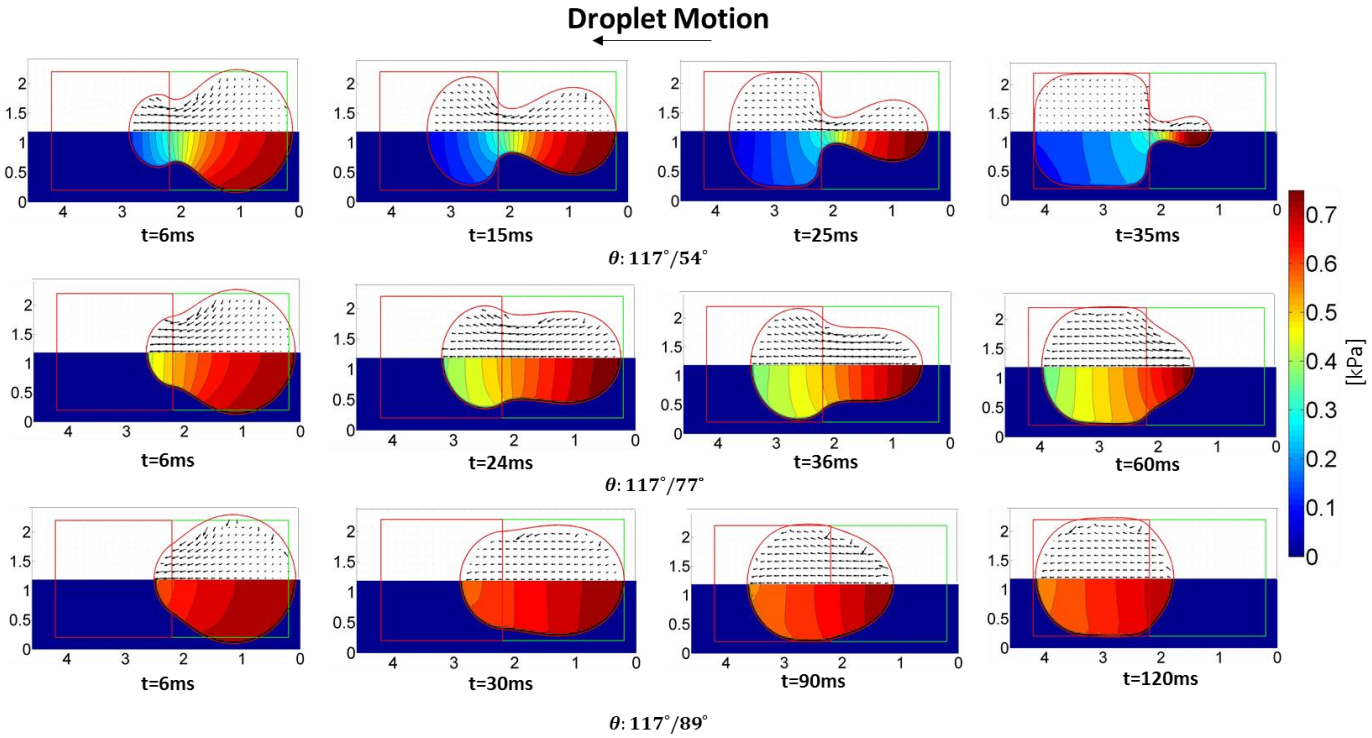

Figure 5-6 Droplet transport in parallel-plate configuration at various actuating contact angles for 2mm square electrode with 0.1mm channel gap (50μm offset from the ground).

contact angle, a neck is formed in the fluid body, since the leading edge moves so fast that the trailing edge falls behind. Due to the concave shape of the neck, capillary pressure plummets sharply and the fluid is squeezed out of the neck. Interestingly, in a deformed droplet that produces noticeable neck, the fastest motion in the fluid occurs at the neck instead of the leading or trailing edge. It has been observed in the numerical study by Guan and Tong [66] that with sufficient electric potential the droplet can even split in two. However, neck formation is less significant for smaller difference in contact angle. For the 117˚/89˚ change in contact angle, the droplet remains mostly elliptical throughout the process with no observable neck formation.

The effect of channel gap on parallel-plate droplet transport is displayed in Figure 5-7. Increased channel gap decreases the pressure difference between the ON/OFF electrodes according to Eq. (5-5) as shown in Figure 5-7(a). Decreased pressure gradient produces less deformed droplet as demonstrated in Figure 5-7(b). Another effect of increasing channel gap is shorter transport time. It has been discussed earlier that the lateral curvature term, $(cos\theta - cos\theta_0)/H$, is the major contributor to the pressure difference between ON/OFF electrodes that drives the fluid in parallel-plate droplet transport. Although this pressure difference decreases with increase in channel gap, the net driving force may not be affected significantly as the cross-sectional area also increases with channel gap. On the other hand, larger channel gap yields lower viscous resistance which can be approximated inversely proportional to channel gap based on a simplified Couette flow model. Subsequently, droplet transport time decreases with increase in channel gap as shown in Figure 5-7(b).

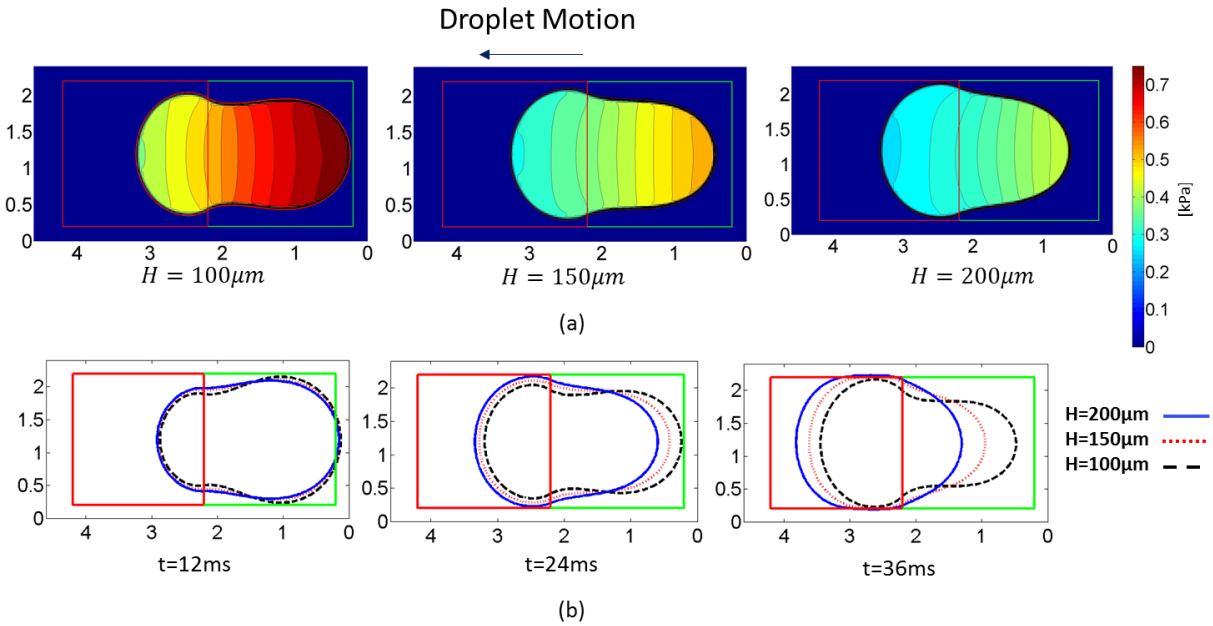

Figure 5-7 Parallel-plate droplet transport at various channel gaps (50μm offset from the ground), (a) pressure distribution at 24 ms and (b) droplet deformation at various time instants.

The effect of electrode size on droplet transport is presented in Figure 5-8 that shows smaller electrode yields faster transport for the same channel gap and actuation voltage. Average leading and trailing edge velocities (calculated by measuring the time required for the leading edge to reach the other end of activated electrode) for various electrode sizes are given in Table 5-I. Larger electrodes contain larger droplets and due to

Table 5-1 Comparison between leading and trailing edge average velocities.

Electrode Size (mm^2)	Average leading edge velocity, v_L (mm/s)	Average trailing edge velocity, v_T (mm/s)	$\frac{v_L - v_T}{v_L} X100$
1.4X1.4	67	34	49.25
2.0X2.0	57	23	59.64
3.0X3.0	33	3.77	88.57

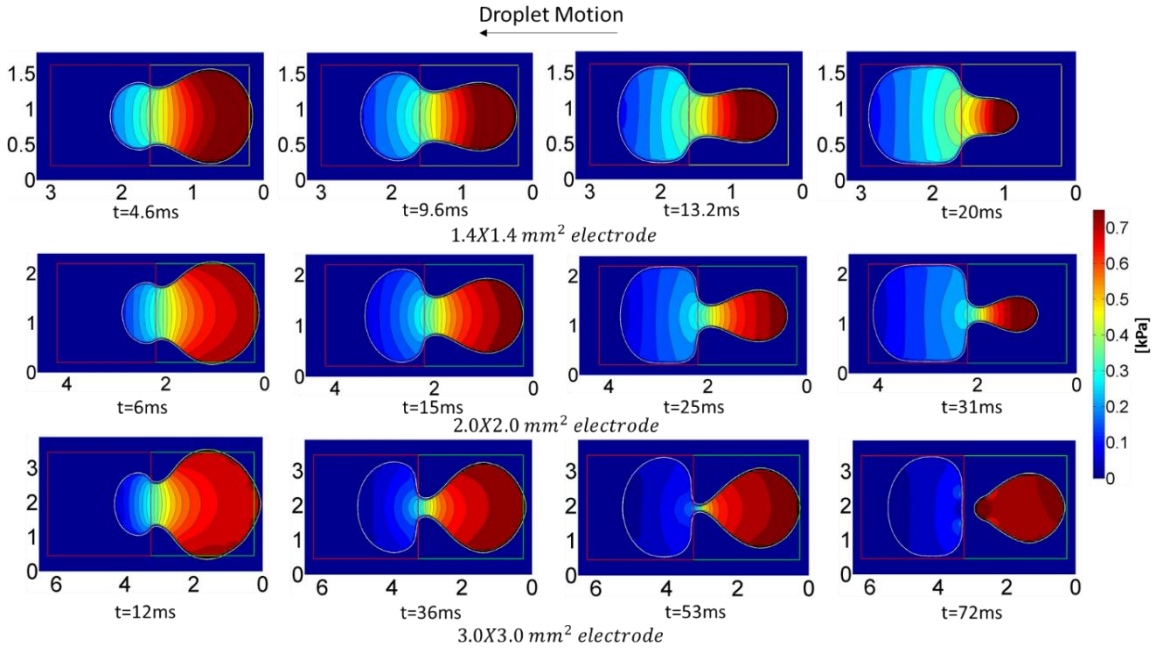

Figure 5-8 Parallel-plate droplet transport at various electrode sizes.

the inertia of larger fluid body, both leading and trailing edge velocities are less in larger electrode. In addition, the leading edge velocity is larger than the trailing edge in all of the cases since the pressure gradient is not uniformly distributed throughout the droplet, but is concentrated near the ON/OFF electrodes junction. It can also be seen that the difference between leading and trailing edge velocities increases with the size of electrode and consequently deformation of the droplet becomes more pronounced. This is due to the factthat the trailing edge falls further behind in the larger electrode with increased inertia. Note that necking is more pronounced in the 2.0 mm electrode than the 1.4 mm electrode and the droplet ultimately splits in the 3.0 mm electrode. Since for the same channel gap and contact angle, the lateral curvature differences between the leading and trailing edges remain unchanged (Eq. 5-5), the pressure profiles inside the droplet are almost same in the three cases at the beginning of the transport. However, as the droplet starts to deform, the negative radial curvature at the neck of droplet becomes prominent in larger electrode and consequently a larger pressure difference between ON-OFF electrodes can be observed.

Droplet Transport in Open-plate Configuration

To compare droplet transport in open-plate configuration with an experimental study [68], an 110˚/93˚ change in contact angle (corresponding to 65V electric potential) was applied to the driving electrode unit while a non-wetting 110˚ static contact angle (same as Cytop) was maintained everywhere else on the substrate. The volume of the water droplet and size of the square actuation pad are 2μL and 1.4mm, respectively as in the experiment. Uniform square mesh of 0.05mm is used based on the results of a grid refinement study. As can be seen from Figure 5-9, the droplet shape remains almost circular in low voltage actuation for both numerical and experimental studies. However, the

average droplet transport velocity has been reported to be 10mm/s in the experiment whereas it has been found to be 13mm/s in the present study.

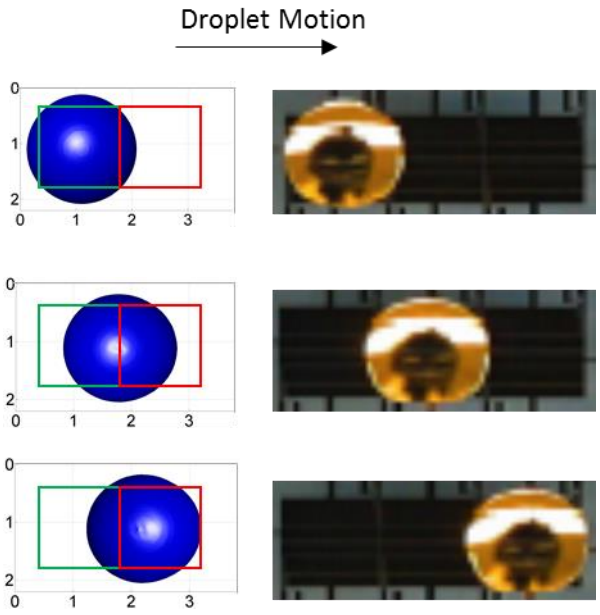

Figure 5-9 Comparison between numerical (left) and experimental (right) [68] droplet transport in open-plate EWOD.

Pressure distribution and velocity profiles inside the droplet during transport in an open plate configuration with 110˚/68˚ change in contact angle are shown in Figure 5-10. There are similarities in electrowetting induced transport mechanism between the parallel and open plate configurations. In both cases, the droplet starts moving towards the activated electrode due to the difference in lateral curvature between the leading and trailing edges. From Figure 5-10 at t=1.98ms, the leading edge of the droplet forms an acute angle while the trailing edge forms an obtuse angle with the substrate producing a difference in lateral curvature and pressure between the two edges and fluid is drawn

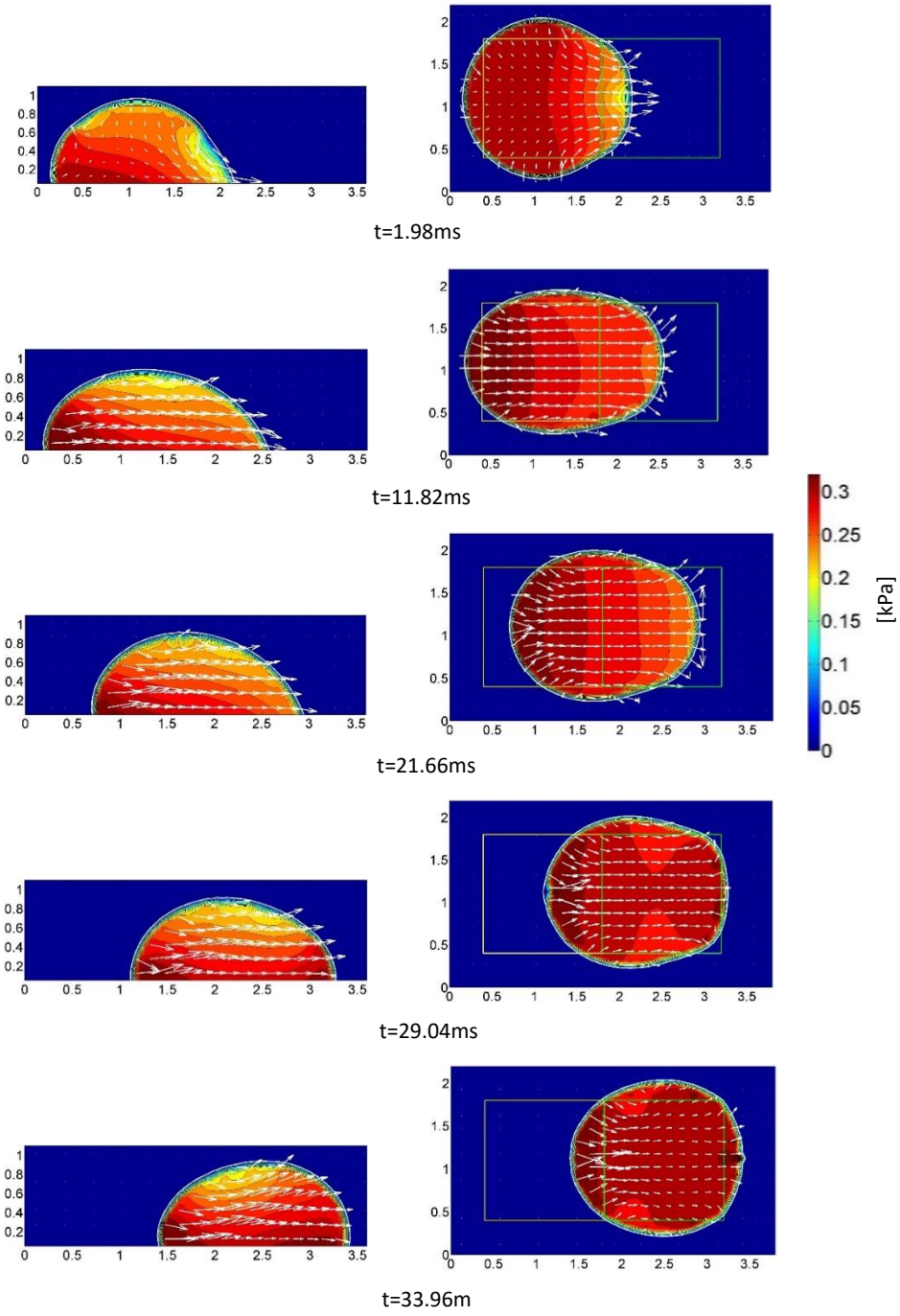

Figure 5-10 Droplet transport in open-plate configuration; LEFT: Cross sectional view (mid-plane), RIGHT: Top view (0.1mm offset from the ground).

towards the actuated electrode. It should be noted that the difference in radial curvature between the leading and trailing edge is not as prominent as in the case of parallel plate configuration (Figure 5-10, t=11.82ms). The shape of the droplet remains elongated until the leading edge reaches the opposite end of the activated electrode when the interface makes an obtuse angle again with the substrate resulting an increase in capillary pressure at the leading edge (t=29.04ms). At t=33.96ms, the lateral curvatures of both ends become comparable which decreases the overall pressure difference between the leading and trailing edge. As a result, the shape of the droplet resumes circular. It has been observed that the droplet keeps moving from left to right due to the kinetic energy and slows down to a complete stop eventually.

The effect of contact angle in droplet transport for open plate configuration is demonstrated in Figure 5-11. As expected, the overall transportation time decreases as the change in contact angle is increased. It can be seen from the figures that the deformation of the droplet also depends on the change in contact angle. Larger change in contact angle causes greater difference in lateral curvature between activated and deactivated electrodes that results in steeper pressure gradient inside the droplet. As a result the droplet is found to be more elongated.

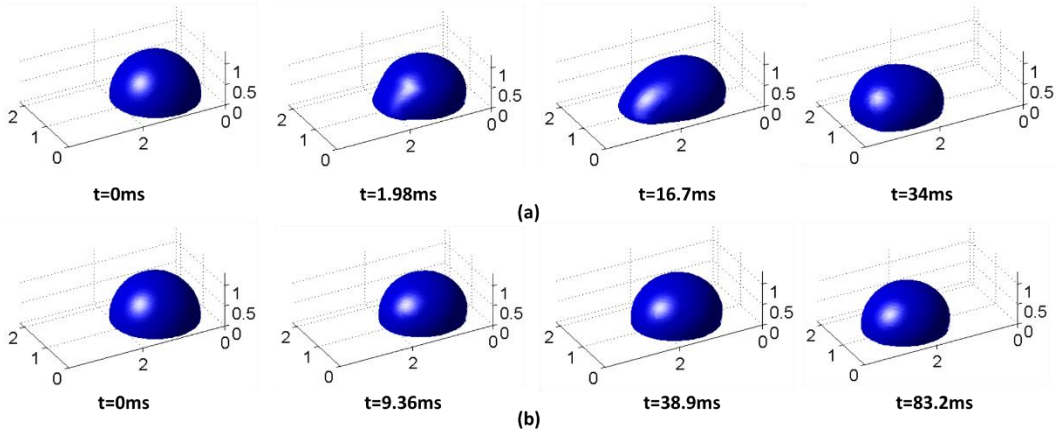

Figure 5-11 Droplet deformation in open-plate configuration at (a) 110˚/68˚ and (b) 110˚/93˚ change in contact angle

Average Transport Velocity in Open-plate and Parallel-plate Configuration

Average transport velocities in parallel-plate and open-plate configuration have been plotted versus electrowetting number in Figure 5-12. The average velocity is calculated by measuring the time required to transport the entire droplet on the actuated electrode. Note that the electrowetting number is given by:

$$\eta = \cos\theta \ - \cos\theta_0 \tag{5-6}$$

It should be noted that the droplet volume in open plate configuration is 10 times larger than the parallel plate configuration. In both cases the size of the square electrode is 1.4 mm and the channel gap in parallel-plate configuration is 0.15mm. Although the droplet volume is larger in open-plate configuration, the transport time is shorter. This is due to the absence of the top plate, the viscous drag force on the droplet is considerably lower for the open-plate configuration.

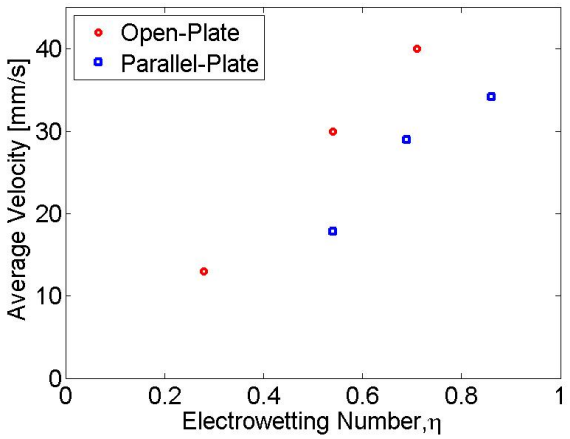

Figure 5-12 Average transport velocity in parallel and open plate configuration.

Closure

Dynamics of electrowetting induced droplet transport in parallel-plate and open-plate EWOD has been analysed numerically using the CLSVOF method for tracking the free surface in conjunction with the CSF model for the surface tension calculation. The various stages of droplet transport have been examined in detail. The effects of voltage amplitude, channel gap and electrode size on the transport process have also been investigated. It has been found that higher voltage, lower channel gap and larger electrode size make more pronounced deformation in parallel-plate droplet transport. Similar deformation tendency has also been seen in higher voltage droplet transport in open-plate configuration. Transport velocities in parallel-plate and open-plate configurations have been compared and open-plate EWOD devices have been found to exhibit faster transport due to lower viscous resistance.

Chapter 6

Conclusion

A numerical method for tracking capillary driven microfluidic interfacial flow has been developed. The transient governing equations for fluid flow have been solved by using finite difference scheme where the surface tension force has been determined using continuum surface force model. The static contact angle has been implemented using a wall adhesion scheme within the CSF framework. The dynamic contact angle has been calculated assuming a fixed deflection from the static contact angle. Successful implementation of the contact angle in numerical model has also been demonstrated.

The free surface has been tracked using a coupled level set and volume of fluid method. Both the level set and volume of fluid functions have been advected using a finite volume scheme. Interface construction and subsequent advection in 3D is a challenging complex procedure which is accomplished by adopting a geometric approach. VOF fluxes across the cell boundary have been calculated using Lagrangian interface propagation scheme and the re-distancing of the level set function has been carried out geometrically. The developed numerical models, both in 2D and 3D, have been validated using benchmark advection tests.

Using the developed numerical method, several micro-fluidic applications such as pendant drop formation from a vertical capillary tube, electrowetting induced droplet detachment and droplet transport in parallel-plate and open-plate EWOD devices have been analyzed. The numerical results have been validated with the available experimental data and by conducting satisfactory grid refinement studies. In each case, the physics of capillary driven flow has been analyzed thoroughly demonstrating the inter-related

dependence among droplet topology, capillary pressure and velocity field. The relevant parametric studies have also been conducted to obtain further insights into the physics.

One of the important extensions of the present work should be the coupling of energy equation to the fluid flow solver. As most of these micro-fluidic problems are related to efficient heat transfer and cooling applications, this extension can unfold a comprehensive picture of the entire process. Another important feature that needs to be developed is dynamic contact angle modeling. The fact that dynamic contact angles are influenced not only by the plate material but also by other factors such as temperature, ambient pressure, droplet properties, electrowetting voltage, surface irregularity and smoothness make prediction of dynamic contact angles very challenging. Yet accurate prediction of dynamic contact angle is necessary for precise matching of numerical results to the experiment. In addition, the present numerical code is written in serial architecture and parallelization is required to improve computational efficiency.

Appendix

Grid Convergence Study

Grid Convergence Study for 3D Pendant Drop Formation

Formation of a pendant droplet from a vertical capillary tube has been simulated with two different grid sizes for the grid refinement study. Water has been supplied through the nozzle of 0.8mm inner radius at 0.08m/s inlet velocity. As shown in Figure A-1, the size and shape of the pendant droplet matches very well at 60ms for different grid sizes and based on this result 0.05mm has been chosen as preferred grid size.

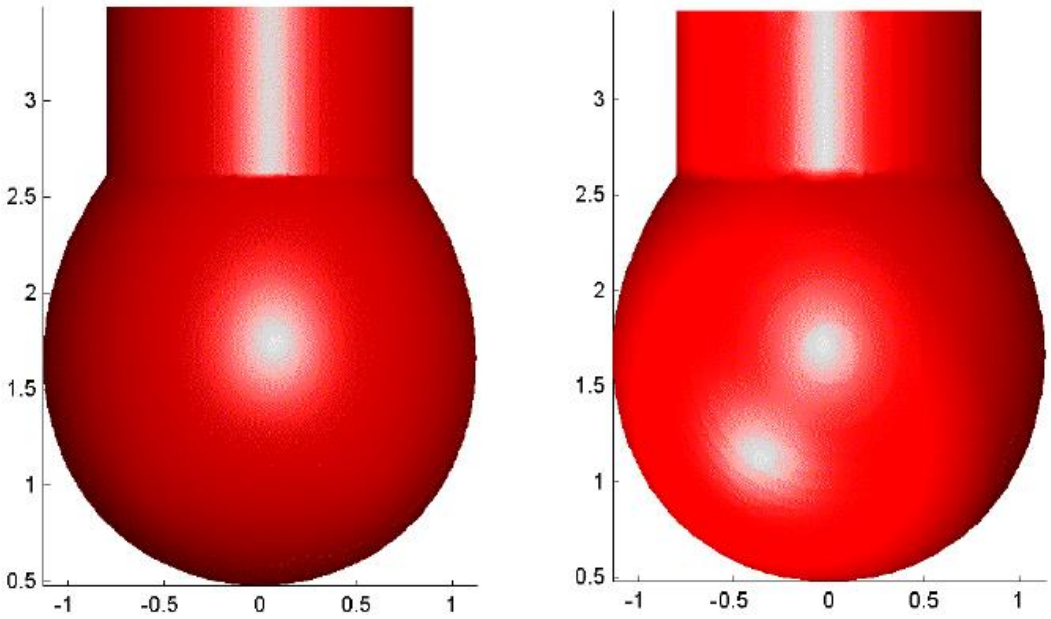

Figure A-1 Pendant droplet , LEFT: 0.025mm, RIGHT: 0.05mm uniform grid size.

Grid Convergence Study for 2D Axisymmetric Pendant Drop Formation

Both time and grid convergence studies are performed to validate the results of pendant and satellite droplet formation in 2D axisymmetric model. The CLSVOF code used here requires three time step constraints for stability. They are the viscous, courant, and capillary conditions and the numerical algorithm adjusts the time step automatically according to these constraints. However, the adjusted time step is only sufficient for stability and it does not guarantee the accuracy of the calculation especially a flow simulation with strong capillary effect. The maximum time step that can be used in the calculation can be defined by the user. Table A-1 shows the result of time convergence study for $0.025mm \times 0.025mm$ grid size. It is found that the time convergence of the present numerical scheme is attained at maximum time step of 1.47μs. For this study a water like fluid has been simulated at 0.08m/s inlet velocity.

Table A-1 Time convergence study at 0.025mmX0.025mm grid size

Nozzle size			dtmax[a] (μs)	t*[b] (ms)
Length (mm)	R_i (mm)	R_o (mm)		
1.9	0.8	1.05	5.88	278
1.9	0.8	1.05	2.94	280
1.9	0.8	1.05	1.47	285
1.9	0.8	1.05	0.74	286

[a] *dtmax* is the maximum time step allowed in the calculation

[b] t^* is the instant of primary bifurcation.

A grid refinement study has been conducted using four different uniform grid sizes at maximum time step of 1.47μs. Table A-2 and Figure A-2 show the results of grid

refinement study. Note that nozzle size is slightly different for different grid sizes which was necessary in order to avoid cutting any numerical fluid cell by the obstacle cells in nozzle. The maximum adjustment in nozzle dimension is less than 1.26 %, and thus the effect of changing the nozzle size can be considered minimum.

Table A-2 Grid convergence study at 1.47μs maximum time step

Nozzle size			$\Delta x \times \Delta y$	t^{*a} (ms)
Length (mm)	R_i (mm)	R_o (mm)	($mm \times mm$)	
1.9	0.8	1.05	0.05X0.05	311.20
1.92	0.8	1.04	0.04X0.04	299.68
1.92	0.81	1.05	0.03X0.03	284.88
1.9	0.8	1.05	0.025X0.025	285.12

[a] t^* is the instant of primary bifurcation.

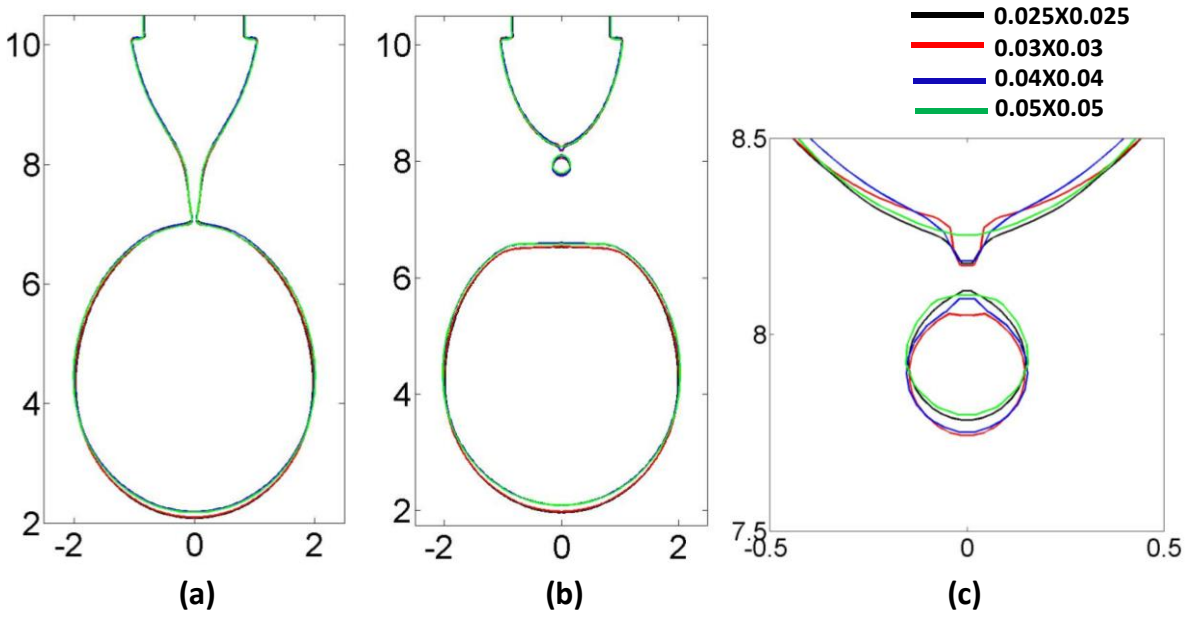

Figure A-2 Grid refinement study; a) primary bifurcation, b) secondary bifurcation and c) magnified view of the satellite droplet,

From the data presented in Table A-2, the primary bifurcation time converges at $0.025mm \times 0.025mm$ grid size. Convergence of liquid cone, filament, primary and satellite droplet at various grid sizes is shown in Figure A-2a and A-2b. The satellite droplets at different grid sizes have been elaborated in Figure A-2c. Note that the positions of satellite droplet are slightly different for different grid sizes, which is expected considering the fact that the satellite droplet is moving at a great speed toward the nozzle immediately after its formation, and it is difficult to capture the same position of satellite droplet at different grid sizes. Nevertheless, the shape and size of the satellite droplet should be similar for different grid sizes and from Figure A-2c, the size and shape of the satellite droplets are almost identical. Considering all the results of the grid refinement study, the present work takes 0.025mmX0.025mm as the preferred grid size.

Grid Convergence Study for Electrowetting Induced Droplet Detachment

Detachment of a 5µL droplet from a hydrophobic surface has been performed with four different mesh sizes for grid convergence. Various stages of droplet detachment obtained from these studies have been shown in Figure A-3. As can be seen, the topology of the droplet matches closely for different grid sizes except for the 0.2mm square mesh, which indicates that grid convergence has been achieved. Consequently, 0.05mm uniform grid size is chosen where the initial droplet radius consists of 26 cells. As for droplet volume other than 5µL, the grid size is chosen such that there are at least 26 cells along the initial droplet radius.

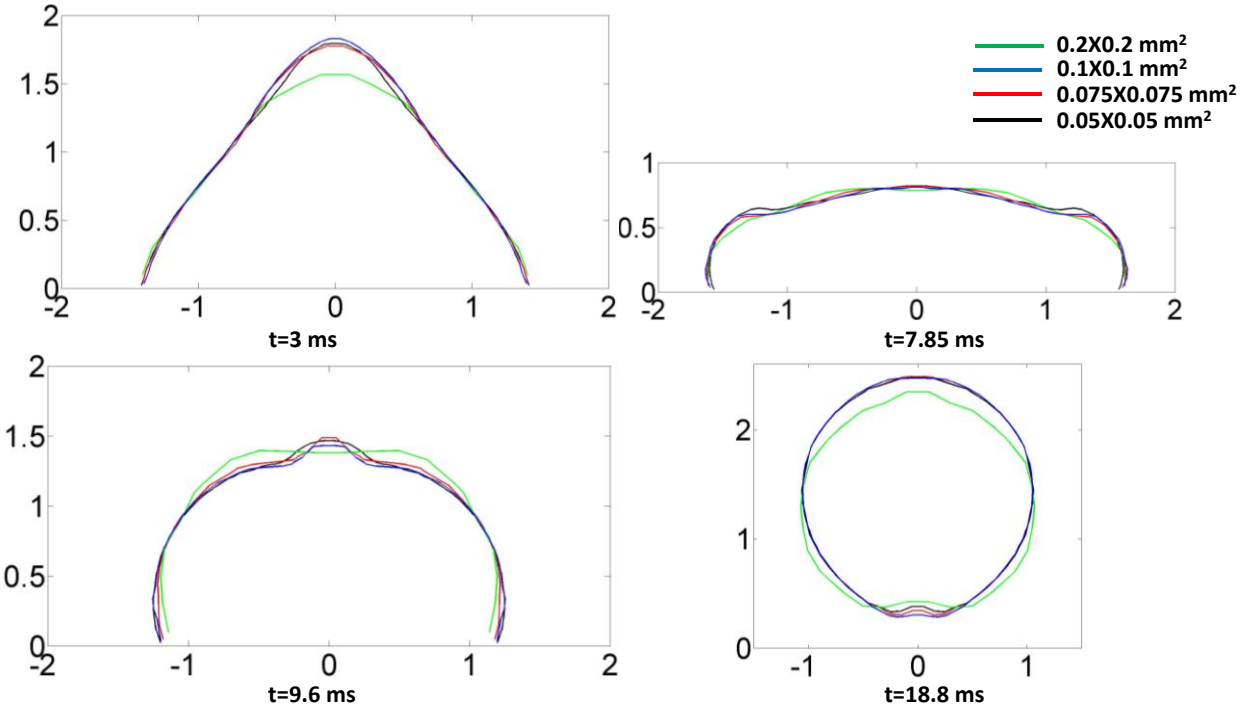

Figure A-3 Droplet detachment with various grid sizes.

Grid Convergence Study for Droplet Transport in Parallel-plate and Open-plate EWOD

Computations of droplet transport in open-plate and parallel-plate configurations have been performed with two different grid sizes in each case for the grid refinement study. In case of parallel-plate configuration (Figure A-4(a)), top views of the droplet at t=24ms have been plotted for 117˚/77˚ change in contact angle and 1.4mm square electrodes with 0.15mm channel gap. In case of open-plate configuration (Figure A-4(b)), the droplet cross-sections at t=84ms have been plotted for 110˚/93˚ change in contact angle where the actuated electrode unit is located between x=1.8mm and 3.2mm. The results obtained in both of the cases show good grid convergence. Based on these results, 0.025mm and 0.05mm uniform grid spacings have been used for parallel-plate and open-

plate configurations, respectively. Similar grid refinement studies have been conducted for different electrode size and channel gap.

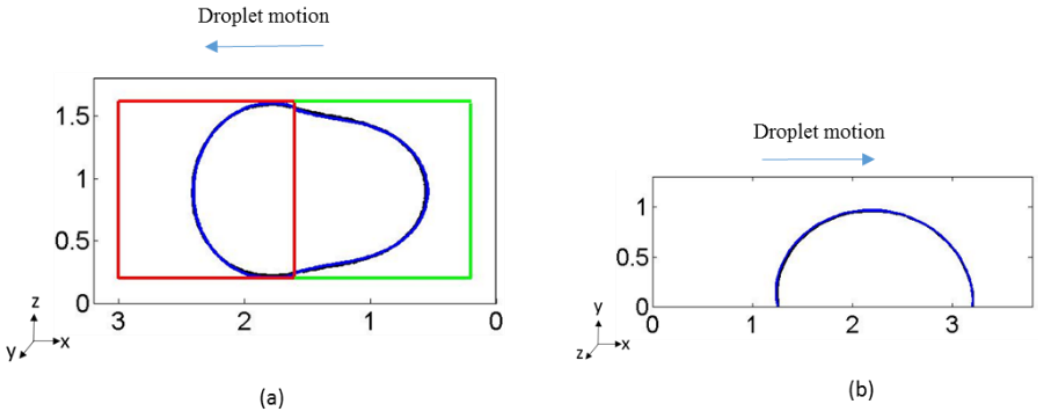

Figure A-4 Grid refinement study of electrowetting induced droplet transport; (a) Parallel-plate configuration with grid sizes 0.025X0.025X0.025 and 0.015X0.015X0.015; (b) Open-plate configuration with grid sizes 0.1X0.1X0.1 and 0.05X0.05X0.05.

References

1. Rudman, M., A volume-tracking method for incompressible multifluid flows with large density variations, *Int. J. Numer. Methods Fluids,* (1998), vol. 28, pp. 357-378.
2. Sussman, M., Smereka, P. and Osher S., A level set approach for computing solutions to incompressible two-phase flow, *J. Comput. Phys.* (1994), vol. 114, pp. 146-154
3. Badalassi, V. E., Ceniceros, H. D. and Banerjee, S., Computation of multiphase systems with phase field models, *J. Comp. Phys.,* (2003), vol. 190, pp. 371-397.
4. Pilliod, J. E. Jr., Puckett, E. G., Second order accurate volume-of-fluid algorithms for tracking material interfaces, *J. Comp. Phys.,* (2004), vol. 199, pp. 465-502.
5. Sussman, M., Fatemi, E., Smereka, P. and Osher, S., An improved level set method for incompressible two-phase flows, *Computers Fluids,* (1998), vol. 27, pp 663-680.
6. Unverdi, S. O. and Tryggvason, G., A front-tracking method for viscous incompressible multi-fluid flows, *J. Comp. Phys.,* (1992), vol. 100, pp 25-37.
7. Tryggvason, G., Scardovelli, R. and Zaleski, S., Direct numerical simulation of gas-liquid multiphase flows, Cambridge University Press, New York, 2011.
8. Gueyffier, D., Li J., Nadim, A., Scardovelli, R. and Zaleski, S., Volume-of-fluid interface tracking with smoothed surface stress methods for three-dimensional flows, *J. Comp. Phys.,* (1999), vol. 152, pp. 423-456.
9. Wang, Z., Yang, J., Koo, B. and Stern, F., A coupled level set and volume-of-fluid method for sharp interface simulation of plunging breaking waves, *Int. J. Multiphase Flow*, (2009), vol. 35, pp 227-246.

10. Kershaw, D. S., The incomplete Cholesky-conjugate gradient method for the iterative solution of linear equations, *J. Comput. Phys.* (1978), vol. 26, pp. 43-65.
11. Hirt, C. W. and Nichols, B. D., Volume of fluid (VOF) method for the dynamics of free boundaries, *J. Comput. Phys*. (1981), vol. 39, pp. 201-225.
12. Sussman, M., Smereka, P. and Osher S., A level set approach for computing solutions to incompressible two-phase flow, *J. Comput. Phys.* (1994), vol. 114, pp. 146-154.
13. Scardovelli, R. and Zaleski, S., Direct numerical simulation of free-surface and interfacial flow, *Annual Rev. Fluid Mech*, (1999), vol. 31, pp. 567-603.
14. Meier, M., Yadigaroglu, G., and Smith, B. L., A novel technique for including surface tension in PLIC-VOF methods, *Eur. J. Mech.-B/Fluids,* (2002), vol. 21(1), pp. 61–73.
15. Renardy, Y., and Renardy, M., PROST: A parabolic reconstruction of surface tension for the volume-of-fluid method, *J. Comput. Phys.,* (2002), vol. 183(2), pp. 400–421.
16. Tong, A. Y., and Wang, Z., A numerical method for capillarity-dominant free surface flows, *J. Comput. Phys*., (2007), vol. 221(2), pp. 506–523.
17. Sussman, M., and Puckett, E. G., A coupled level set and volume-of-fluid method for computing 3D and axisymmetric incompressible two-phase flows, *J. Comput. Phys*., (2000), vol. 162(2), pp. 301–337.
18. Son, G., and Hur, N., A coupled level set and volume-of-fluid method for the buoyancy-driven motion of fluid particles," *Numer. Heat Transfer, Part B,* (2002), 42(6), pp. 523–542.

19. Sussman, M., A second order coupled level set and volume-of-fluid method for computing growth and collapse of vapor bubbles, *J. Comput. Phys.,* (2003), vol. 187(1), pp. 110–136.
20. Yang, X., James, A. J., Lowengrub, J., Zheng, X., and Cristini, V., An adaptive coupled level-set/volume-of-fluid interface capturing method for unstructured triangular grids, *J. Comput. Phys.,* (2006), vol. 217(2), pp. 364–394.
21. Noh, W.F., Woodward P. R., SLIC (Simple Line Interface Calculation), in: A.I. van der Vooren, P.J. Zandbergen (Eds.), *Lecture Notes in Physics*, (1976), vol. 59, pp. 330–340.
22. Puckett, E. G. and Saltzman, J.S., A 3-d adaptive mesh refinement algorithm for multimaterial gas dynamics*, Physica D,* (1992), vol. 60, pp. 84–104.
23. Parker, B.J. and Youngs, D.L., Two and three dimensional Eulerian simulation of fluid flow with material interfaces, *Technical Report 01/92*, *UK Atomic Weapons Establishment*, Aldermaston, Berkshire, February 1992.
24. Puckett, E.G., A volume-of-fluid interface tracking algorithm with applications to computing shock wave refraction, in: H. Dwyer (Ed.), *Proceedings of the Fourth International Symposium on Computational Fluid Dynamics*, Davis, CA, (1991), pp. 933–938.
25. Brackbill, J. U., Kothe, D. B. and Zemach, C., A continuum method for modeling surface tension, *J. Comput. Phys.***,** (1992), vol. 100, pp. 335-354.
26. Kothe, D. B., Mjolsness, R. C. and Torrey, M. D., RIPPLE: A Computer Program for Incompressible Flows With Free Surfaces, Los Alamos National Laboratory, Technical Report No. LA-12007-MS (1991).
27. Senthilkumar, S., Delaure, Y. M. C., Murray, D. B. and Donnelly, B. The effect of the VOF-CSF static contact angle boundary condition on the dynamics of sliding

and bouncing ellipsoidal bubbles, *Int. J. Heat and Fluid Flow,* (2011), vol. 32, pp. 964-972.

28. Peregrine, D. H., Shoker, G. and Symon A., The bifurcation of liquid bridges, *J. Fluid Mech.,* (1989), vol. 212, pp. 25-39.
29. Schulkes, R. M. S. M., The evolution and bifurcation of a pendant drop*, J. Fluid Mech,* (1994), vol. 278, pp. 83-100.
30. Zhang, D. F. and Stone, H. A., Drop formation in viscous flows at a vertical capillary tube, *Phys. Fluids,* (1997), vol. **9**, pp. 2234-2242.
31. Zhang, X. and Basaran, O. A., An experimental study of dynamics of drop formation, *Phys. Fluids,* (1995), vol. **7**, pp. 1184-1203.
32. Zhang, X. Dynamics of growth and breakup of viscous pendant drops into air, *J. Colloid Interface Sci.* (1999), 212, pp. 107-122.
33. Ambravaneswaran, B., Wilkes, E. D. and Basaran, O. A., Drop formation from a capillary tube: Comparison of one-dimensional and two dimensional analyses and occurrence of satellite drops, *Phys. Fluids.,* (2002), vol. 14, pp. 2606-2621.
34. D'Innocenzo, A., Paladini, F. and Renna, L., Experimental study of dripping dynamics, *Phys. Rev. E,* (2002), vol. 65, p. 056208.
35. D'Innocenzo, A. and Renna, L., Dripping Faucet, *Int. J. Theor. Phys.,* (1996), vol. 35, pp. 941-973.
36. Shi, X. D., Brenner, M. P. and Nagel., S. R., A cascade of structure in a drop falling from a faucet, *Science*, (1999), vol. 265, pp. 219-222.
37. Brenner, M. P., Eggers, J., Joseph, K., Nagel, S. R. and Shi, X.D., Breakdown of scaling in droplet fission at high Reynolds number, *Phys. Fluids*, (1997), vol. 9, pp. 1573-1590.

38. Subramani, H. J., Yeoh, H. K., Suryo, R. S., Xu, Q., Ambravaneswaran, B. and Basaran, O. A. ,Simplicity and complexity in dripping faucet, *Phys. Fluids*, (2006), vol. 18, p. 032106.
39. Eggers, J., Nonlinear dynamics and breakup of free-surface flows, *Rev. Modern Phys*., (1997), vol. 69, pp. 865-929.
40. Ambravaneswaran, B., Phillips, S. D. and Basaran, O. A., Theoretical analysis of a dripping faucet, *Phys. Rev. Lett.,* (2000), vol. 85, pp. 5332-5335.
41. Notz, P. K., Chen, A. U., and Basaran, O. A., Satellite drops: Unexpected dynamics and change of scaling during pinch off, *Phys. Fluids,* (2001), vol. 13, p. 134906.
42. Tong, A.Y. and Wang, Z., Relaxation dynamics of a free elongated liquid ligament, *Phys. Fluids.,* (2007), vol. 19, p. 092101.
43. Enright, R., Miljkovic, N., Alvarado, J. L., Kim, K. and Rose, J. W., Dropwise condensation on micro-and nanostructured surfaces, *Nanoscale Microscale Thermophys. Eng.,* (2014), vol. 18, pp. 223-250.
44. Mugele, F., Baret, J.-C. and Steinhauser, D., Microfluidic mixing through electrowetting-induced droplet oscillations, *Appl. Phys. Lett.,* (2006), vol. 88 (20), p. 204106.
45. Lee, S. J., Lee, S., Kang, K. H., Droplet jumping by electrowetting and its application to the three-dimensional digital microfluidics, *Appl. Phys. Lett.,* 2012, 100 (8), 081604.
46. Cavalli, A., Preston, D. J., Tio, E., Martin, D. W., Miljkovic, N., Wang, E. N., Blanchette, F. and Bush, J. W. M., Electrically induced drop detachment and ejection, *Phys. Fluids.,* (2016), vol. 28(2), p. 022101.

47. Lee, S. J., Hong, J., Kang, K.H., Kang, I. S. and Lee, S. J. Electrowetting-induced droplet detachment from hydrophobic surfaces, *Langmuir,* (2014), vol. 30, pp. 1805-1811.
48. Mugele, F., Baret, J., Electrowetting: from basics to applications. *J. Phys,: Condens. Matter* (2005), vol. 17 (28), pp. R705-R774.
49. Cho, S. K., Moon, H. and Kim, C.-J., Creating, transporting, cutting and merging liquid droplets by electrowetting-based actuation for digital microfluidic circuits, *J. Microelectromech. Syst.* (2003), vol. 12 (1), pp. 70-80.
50. Gupta, R., Sheth, D. M., Boone, T. K., Sevilla, A. B. and Frechette, J., Impact of pinning of the triple contact line on electrowetting in parallel plate microchannels, *Langmuir,* (2011)*,* vol. 27 (24), pp. 14923-14929.
51. Nelson, W. C. and Kim, C. -J., Droplet actuation by electrowetting-on-dielectric (EWOD): a review, *J. Adh. Sci. Tech.,* (2012), vol. 26, pp. 1747-1771.
52. Pollack, M. G., Shenderov, A. D. and Fair, R. B., Electrowetting-based actuation of droplets for integrated microfluidics*, Lab Chip.,* (2002), vol. 2(2), pp. 96-101.
53. Mach, P., Krupenkin, T., Yang, S. and Rogers, J. A., Dynamic tuning of optical waveguides with electrowetting pumps and recirculating fluid channels, *Appl. Phys Lett.*, (2002), vol. 81, pp. 202-204.
54. Mohseni, K. and Baird, E. S., Digitized heat transfer using electrowetting on dielectric, *Nanoscale Microscale Thermophys. Eng.,* (2007), vol. 11, pp. 99–108.
55. Cheng, J. T. and Chen, C.L. Adaptive chip cooling using electrowetting on coplanar control electrodes, *Nanoscale Microscale Thermophys. Eng.,* (2010), vol. 14, pp. 63–74.

56. Enright, R., Miljkovic, N., Alvarado, J. L., Kim, K. and Rose, J. W., Dropwise condensation on micro-and nanostructured surfaces, *Nanoscale Microscale Thermophys. Eng.,* (2014), vol. 18, pp. 223-250.
57. Berge, B. and Peseux, J., Variable focal lens controlled by an external voltage: an application of electrowetting, *Eur. Phys. J.*, (2000), vol. E 3, pp. 159-163.
58. Palan, V. and Shepard, W. S., Jr. Enhanced water removal in a fuel cell stack by droplet atomization using structural and acoustic excitation, *J. Power Sources*, (2006), vol. 159 (2), pp. 1061−1070.
59. Hayes, R. A. and Feenstra, B. J., Video-speed electronic paper based on electrowetting, *Nature,* (2003), vol. (425), pp. 383-385.
60. Jang, L.-S., Lin, G.-H., Lin, Y. -L., Hsu, C.-Y., Kan, W.-H. and Chen C.-H., Simulation and experimentation of a microfluidic device based on electrowetting on dielectrode, *Biomed Microdevices,* (2007), vol. 9, pp. 777-786.
61. Walker, S. W. and Shapiro, B., Modeling the fluid dynamics of electrowetting on dielectric (EWOD), *J. Microelectromech. Syst.*, (2006), vol. 15(4), pp. 986-1000.
62. Walker, S. W., Shapiro, B. and Nochetto, R. H., Electrowetting with contact line pinning: Computational modeling and comparisons with experiments, *Phys. Fluids,* (2009), vol. 21(10), p. 102103.
63. Dolatabadi, A., Mohseni, K. and Arzpeyma, A., Behavior of a moving droplet under electrowetting actuation: Numerical simulation, *Can. J. Chem. Eng.,* (2006), vol. 84, pp.17-21.
64. Arzpeyma, A., Bhaseen, S., Dolatabadi, A. and Adams, P. W., A coupled electro-hydrodynamic numerical modeling of droplet actuation by electrowetting, *Colloids Surf. A,* (2008), vol. 323, pp. 28-35.

65. Guan, Y. and Tong, A. Y., A numerical study of droplet splitting and merging in a parallel-plate electrowetting-on-dielectrode device, *J. Heat Transfer,* (2015), vol. 137, p. 091016.

66. Guan, Y. and Tong, A. Y., A numerical study of microfluidic droplet transport in a parallel-plate electrowetting-on-dielectrode (EWOD) device*, Microfluid Nanofluid*, (2015), vol. 19, pp. 1477-1495.

67. Nelson, W. C., Sen, P. and Kim C. –J., Dynamic contact angles and hysteresis under electrowetting-on-dielectric, *Langmuir*, (2011), vol. 27, pp. 10319-10326.

68. Yi, U.-C. and Kim, C.-J., Characterization of electrowetting actuation on addressable single-side coplanar electrodes, *J. Micromech. Microeng.*, (2006), vol. 16, pp. 2053-2059.

69. Yaddessalage, J. B., Study of the capabilities of electrowetting on dielectric digital microfluidics (EWOD DMF) towards the high efficient thin-film evaporative cooling platform, *PhD Dissertation*, (2013),The University of Texas at Arlington.

Biographical Information

Md Ashraful Islam was born in Jamalpur, Bangladesh. He received his BSc. in Mechanical Engineering degree in 2009 from Bangladesh University of Engineering and Technology. After graduation, he worked as a Shift Engineer in Summit Narayanganj Power Limited (Bangladesh). He entered the University of Texas at Arlington for his PhD study in Mechanical Engineering in September, 2011. He received his PhD in December, 2016.